Vectorial Multichannel-Spin-Polarimetry and the Analysis of Spin-Transport in Metal-Organic Interfaces

Dissertation

for the degree of
"Doktor der Naturwissenschaften"

Faculty 08:
Physics, Mathematics and Computer Science
Johannes Gutenberg-Universität
in Mainz

Submitted November 11, 2016 by
Erik Dai Schaefer
born September 18th, 1987
in Bad Soden am Taunus

Abstract

Photoemission spectroscopy has become the key technique for the investigation of electronic properties of promising materials such as Heusler compounds, Weyl systems, materials exhibiting a strong Rashba effect, topological insulators or hybrid metal-organic interfaces. During the last decade photoemission spectroscopy without spin resolution enjoyed a considerable increase in performance due to parallel image detection while the spin polarization analysis of a given electron beam remained time consuming. Since potential candidates for spintronic applications such as metal-organic interfaces tend to degrade within a short period, a massive reduction of spin-resolved data acquisition time is crucial. A newly developed high-performance imaging spin filter system based on a large Ir(001) scattering crystal tackles this issue by enhancing the measurement efficiency. An increase of the effective figure of merit by a factor of over 10^3 in contrast to standard single-channel detectors is presented together with a detailed characterization of the experimental setup. Furthermore, the spectrometer resolution, spin filter preparation and lifetime are reviewed. An energy and angular resolution of 27 meV and 0.23° has been determined for an energy and angular acceptance of 1.5 eV and ±10°. The spin filter efficiency is analyzed by mapping a broad range of scattering energy and azimuthal angle. A Sherman function of up to 0.44 has been measured under ideal conditions. If the scattering plane coincides with a mirror plane of the crystal, the spin filter is only sensitive to the component of the spin vector perpendicular to the scattering plane. A scattering plane that does not coincide with a crystal mirror plane yields a high sensitivity to spin vector components that are parallel to the scattering plane. A spin rotator element enables the independent determination of the two in-plane components of the spin vector. By combining three or six scattering conditions a vectorial spin analysis becomes possible for both, magnetic and non-magnetic samples.

Spin-resolved spectra of Fe/W(110) and H_2TPP films of different thickness on Fe/W(110) are measured with the efficient multichannel spin-resolving photoemission spectrometer and with the ESPRESSO spectrometer at the Hiroshima Synchrotron Radiation Center. The experimental results allow for a determination of the spin diffusion length within the molecular film.

Zusammenfassung

Die Photoemissionsspektroskopie ist zur Schlüsseltechnik für die Untersuchung elektronischer Eigenschaften von vielversprechenden Materialien wie Heusler Verbindungen, Weyl Systeme, Materialien mit Rashba-Effekt, topologische Isolatoren oder metall-organische Grenzflächen geworden. In den letzten Jahren hat sich die Leistungsfähigkeit der Photoemissionsspektroskopie durch die Einführung der parallelen Bildgebung erheblich gesteigert. Die Analyse der Spinpolarisation blieb jedoch zeitaufwendig. Da für Spintronikanwendungen potenziell geeignete Materialien wie zum Beispiel metall-organische Grenzflächen dazu neigen, innerhalb von kurzer Zeit qualitativ zu degradieren, ist eine deutliche Reduzierung der Messdauer spinaufgelöster Daten notwendig.
Ein neu entwickelter und leistungsfähiger abbildender Spinfilter, der auf einem großen Ir(001) Streukristall basiert, bewältigt dieses Problem durch die Erhöhung der Messeffizienz. Eine Erhöhung der effektiven Gütefunktion um einen Faktor von über 10^3 im Gegensatz zu üblichen einkanaligen Detektoren wird zusammen mit einer detaillierten Charakterisierung des experimentellen Aufbaus präsentiert. Insbesondere wird die Spektrometerauflösung im Energie- und Impulsraum bestimmt. Die Energie- und Winkelauflösung beträgt 27 meV bzw. 0.23° für eine Energie- und Winkelakzeptanz 1.5 eV bzw. ±10°. Die Spinfiltereffizienz wird über große Energie- und Winkelbereiche kartiert und analysiert. Dabei wird unter idealen Bedingungen eine Sherman Funktion von bis zu 0.44 gemessen. Fällt die Streuebene mit einer Spiegelebene des Kristalls zusammen, ist der Spinfilter ausschließlich sensitiv auf die Komponente des Spinvektors senkrecht zur Streuebene. Streuebenen, die nicht mit einer Spiegelebene zusammenfallen, ergeben eine hohe Sensitivität für Komponenten des Spinvektors parallel zur Streuebene. Ein Element zur Drehung von Spins ermöglicht die unabhängige Bestimmung der zwei in-plane Komponenten des Spinvektors. Durch die Kombination von drei oder sechs Streubedingungen wird die vektorielle Spinanalyse für magnetische und unmagnetische Proben möglich.
Spinaufgelöste Spektren von Fe/W(110) und H_2TPP Schichten unterschiedlicher Dicke auf Fe/W(110) werden mit dem effizienten und parallelisierten spin-auflösenden Photoemissionsspektrometer sowie mit dem ESPRESSO Spektrometer am Hiroshima Synchrotron Radiation Center gemessen. Die experimentellen Resultate ermöglichen die Bestimmung der Spindiffusionslänge innerhalb des molekularen Films.

Contents

1 Introduction

The ever ongoing miniaturization of electronic devices leads to the development of new concepts. A new type of quantum-mechanical information processing is based on the orientation of electron spins. To this date, common electronic devices use the electron charge as information carrier. Components that rely on the spin are covered by the term spintronics. In addition to the possible reduction in size, a higher energy efficiency, faster cycle times and non-volatile memory could be realized by using spintronics [5, p. 562] [16, p. 329]. Intensive research is therefore carried out in the context of spintronics.

Hybrid metal-organic interface materials [42] are potential candidates for future spintronic components. The possibility to control desired properties by selective modulation of physical and chemical parameters allows for a high flexibility and variability. Additionally, new materials such as Heusler compounds [27], Weyl systems [105], materials exhibiting a strong Rashba effect [9] and topological insulators [32, 52] with unique spin-related properties [17, 40, 64] have emerged recently. The efficient spin-resolving analysis is therefore of great importance for the physical understanding. It paves the way for potential industrial applications and future research.

So far, many interfaces and promising materials with spin-related properties are largely unexplored mainly due to the low efficiency and the associated long measurement durations of most spin-resolving methods. For example, this leads to radiation damages of organic film layers or unavoidable surface contamination perturbing the results after a short time.

The spin- and angle-resolving photoemission spectroscopy turns out to be an ideal measurement method for the electronic characterization of such materials. A new type of measurement technique is needed to obtain the desired efficiency. Recently, a spin-resolved multichannel technique has been introduced [51, 94]. Unlike conventional one-channel systems (e.g. as described in references [43, 46]), the measuring efficiency of the novel multichannel concept has been enhanced by up to 3 orders of magnitude [51, 89]. Multichannel spin detection thus opens a pathway to study sensitive materials requiring fast measurements with high measurement efficiency. In the following years, different multichannel concepts have been further developed. They use an Au/Ir spin filter crystal in combination with SPLEED [95], a multichannel Mott concept [87], a spin filter based on exchange interaction and VLEED [39] and a time-of-flight momentum microscopy system with SPLEED at a tungsten crystal [54].

In this thesis the performance of a newly developed multichannel spin- and angle-resolving spectrometer is presented. This thesis covers the development, characterization and use of a multichannel spin-resolving spectrometer for the spin-transport analysis of metal-organic interfaces. A brief description about the relevant theory covering the experimental electronic structure, the electron spin, spintronics and photoemission spectroscopy is given

in chapter 2. In chapter 3, the experimental setup, operating processes and settings are described in detail. Chapter 4 presents the results. It covers three important parts: (i) the characterization of the constructed multichannel spin- and angle-resolving spectrometer, (ii) the analysis of Fe/W(110) systems and the H_2TPP-iron interface system with the multichannel spectrometer and (iii) the detailed analysis of the H_2TPP-iron interface at the Hiroshima Synchrotron Radiation Center. Chapter 5 gives a short summary and outlook.

As the main experimental result, spin-resolved photoemission spectra of Fe(110) as well as synthetic organic H_2TPP layers on ferromagnetic substrates are presented. They have been measured with the multichannel spin-, energy- and angle-resolving photoemission spectrometer. The detailed analysis of the imaging spin filter characteristics has led to the previously unexpected possibility of the vectorial spin polarization analysis.

2 Theory and Basic Concepts

2.1 Photoelectric Effect

During experiments on sparking phenomena in 1887, Heinrich Hertz discovered that ultraviolet light on electrodes influences the maximum possible flashover gap width [34]. It was the first indication of the photoelectric effect. The theoretical explanation of the non-classical effect, in which the quantum nature of light was included, followed by Albert Einstein in 1905 [21]. It describes the process of low-energy interaction between photons and matter, where electrons are extracted from a solid by the absorption of photons. This process is also known as photoemission.
The following sections follow the representation as given in reference [37, p. 1-5]. In order to generate a photoemitted electron from a sample, the electron must receive a minimum amount of photon energy to overcome the vacuum level energy E_{vac}. The required amount of photon energy is given by the sum of the materials' work function Φ_{mat} and the absolute value of the binding energy E_B. The work function is the difference between the vacuum level and the Fermi level. It is usually in the order of few eV and sensitively depends on the sample surface. In contrast to that, possible binding energies range up to the keV region dependent on the quantum state of the electron. If the transferred photon energy $\hbar\omega$ is at least higher than the sum of work function and binding energy, the electron can potentially leave the sample in different directions with the excess energy as kinetic energy E_{kin} (see figure 2.7) according to:

$$E_{kin} = \hbar\omega - \Phi_{mat} - |E_B|. \tag{2.1}$$

However, when trying to detect the photoemitted electrons with a spectrometer, the device-dependent work function Φ_{spec} has to be taken into account. When the sample and the spectrometer are electrically connected the Fermi energies are at the same reference level (see figure 2.1 (a)). Nevertheless, without a spectrometer calibration an incorrect energy value $E_{kin}^{'}$ would be measured due to the different work functions

$$E_{kin} + \Phi_{mat} = E_{kin}^{'} + \Phi_{spec}. \tag{2.2}$$

For successful photoemission upon excitation, the electrons must also possess a sufficiently large momentum component $k_\perp$ perpendicular to the sample surface, so that they can overcome the surface potential barrier and be emitted under an angle θ smaller than 90 degrees. The potential barrier is generated by the lack of translational symmetry in the perpendicular direction to the surface (see figure 2.1 (b)). Phenomenologically, the electron

is trapped inside a potential of depth $E_{vac} - V_0$, where $V_0 > 0$ is the inner potential of the crystal. This causes $k_\perp$ not to be conserved during transmission and does not allow for a precise determination of $k_\perp$ without additional information. However, the free electron final states approximation enables the formulation of an expression for $k_\perp$ (2.3). It uses the assumption that the final state of the electron can be described with a dispersion relation of free electrons shifted by V_0:

$$k_\perp = \sqrt{\frac{2m}{\hbar^2}(E_{kin} cos^2\theta + V_0)}, \tag{2.3}$$

$$E_{kin} = \frac{\hbar^2 \vec{k}^2}{2m} - V_0. \tag{2.4}$$

If an electron approaches the surface under a flat angle so that $k_\perp$ becomes small and falls below a certain limit, the electron will be totally reflected into the solid instead of transmitted through the surface. For an escape of an electron into the vacuum the following inequation must be satisfied [37, p. 353]:

$$E_{vac} - V_0 \leq \frac{\hbar^2 k_\perp^2}{2m}. \tag{2.5}$$

In contrast to that, $k_\parallel$ is conserved during the transmission (see figure 2.1 (b)) and simply accessible by knowing the emission angle θ and the kinetic energy E_{kin} of the electron:

$$k_\parallel = \sqrt{\frac{2m}{\hbar^2} E_{kin}} \cdot sin\Theta. \tag{2.6}$$

The measurable photoelectron spectrum is naturally limited by the available photon excitation energy predetermining the possible emission angles and kinetic energies. For a given photon excitation energy the measurable three-dimensional energy-momentum parameter space (E_{kin}, $k_{x\parallel}$, $k_{y\parallel}$) forms a paraboloid, which is also referred as photoemission horizon (see figure 2.1 c)).
Photoemission is of indispensable importance for many experimental techniques. Through electron spectroscopy, i.e., spin polarization and intensity measurements at different kinetic energies and emission angles, the electronic properties of samples can be determined. This measurement method is called angular-resolved photoemission spectroscopy (ARPES) and has become one of the most important techniques for the determination of band structures in solid-state physics.

2.2 Electronic Structure and Symmetry

2.2.1 Band Structure and Spectral Function

Considering a system of non-interacting electrons in a solid, the electronic states can no longer be characterized by discrete energies like practicable in individual atoms. In crys-

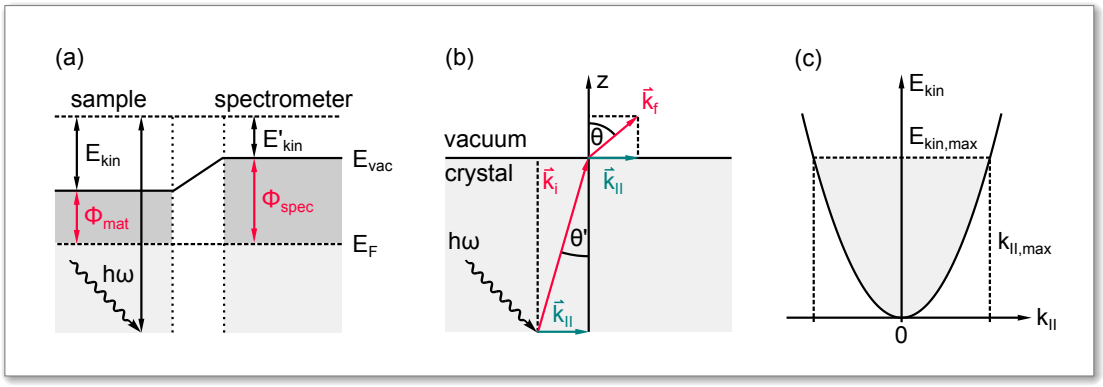

Figure 2.1: (a) Diagram of sample and spectrometer energy levels where the Fermi energy E_F is in balance. The inner potential V_0 is given by $\frac{\hbar^2\vec{k}^2}{2m} - E_{kin}$. (b) Electron momentum inside ($\vec{k}_i$) and outside ($\vec{k}_f$) the sample with conservation of $k_{\|}$. (c) Two-dimensional parameter space (gray) enclosed by the photoemission horizon for a given maximum kinetic energy.

talline materials with a periodic regular atomic or even molecular lattice, the states are described by the electronic band structure, which has its origin in the superposition of atomic orbitals. Here, possible states are characterized by the binding energy and by the momentum. The dispersion $E(\vec{k})$ results in band-like structures. In metals, bands resulting from different atomic orbitals usually overlap. In some cases, energy intervals exist without allowed states, named band gaps. The existing relation between energy E and momentum $\vec{p}$ (or wave vector $\vec{k} = \frac{\vec{p}}{\hbar}$) is also known as the electron dispersion relation $E(\vec{k})$, while the amount of states per energy interval dE is described by the density of states $D(E)$. In ferromagnets, the band structure differs in general for spin up and spin down electrons and can be separately analyzed. Spin-resolved band structures are particularly important in the research field of spintronics.

In contrast to the band structure, the spectral function describes the electronic properties of systems including many-body effects such as electron-phonon coupling, electron-magnon coupling and electron-electron interaction. The spectral function represents the probability of removing or adding an electron at energy E and momentum $\vec{k}$. The many-body effects lead to an energetic broadening of states compared to the band structure. This broadening has its origin mainly in electron correlation effects limiting the lifetime of the photohole (broadening with Lorentzian shape) and, additionally, the thermal Doppler effect or rather the atom or molecule movement according to the Maxwell-Boltzmann distribution (broadening with Gaussian shape).

A measured photoemission intensity spectrum contains information on this spectral function. The spectrum can be derived by using Fermi's Golden Rule for an N-electron system and applying the sudden approximation, which incorporates the aspect that a photoelectron decouples from the remaining system immediately after its photoexcitation and before

the system relaxation sets in. The additional consideration of linear dichroism effects from the lights' angle of incidence, electron transition probabilities and final states for example leads to deviations from the spectral function, which must be considered in the evaluation. In real materials, the electronic properties are not necessarily uniform over the crystal. Symmetry breaking at the crystal surface results in surface states that are nonexistent in the bulk, for example. The intermixing of surface and bulk states can lead to additional surface resonance states. Influencing factors like surface contamination from residual gas in the experimental chamber can additionally change the observed structures and contribute to a background.

2.2.2 Band Structure Calculations

The density-functional theory (DFT) is a computational modelling method that is frequently used to calculate band structures. It is considered as first-principles theory and has proven to provide proper structural characteristics of bands and electronic properties in many cases. The DFT band plot calculations are therefore often compared with results from photoemission experiments.
The theory involves approximations to render the problem of an insoluble N-body Schrödinger equation. It is based on the electron density, which is sufficient to map the ground state energy of a fictive non-interacting many-electron system according to the Hohenburg-Kohn theorem [36]. By using the Born-Oppenheimer approximation, an effective potential and one-electron wave functions as approximation, the N-body Schrödinger equation transforms into the Kohn-Sham equations containing the electron density. The electron density can then be determined in an iterative process by variation. In a final step, the undefined part of the effective potential, the exchange-correlation potential which describes the correspondent effects, has to be determined in order to calculate the ground state energy. A possible definition for the exchange-correlation potential is given by the local density approximation (LDA), which assumes a uniform electron density.
Despite the approximations, DFT in combination with LDA often provides reasonable results. There are many other methods and approximations which can potentially provide more accurate results. Nevertheless, the description of strongly correlated N-electron systems is a challenging and not always solvable task.

2.2.3 Fermi Level

The states are generally occupied with electrons up to the Fermi level E_F, which is often chosen to be the zero point of energy in diagrams. Binding energies E_B of electrons are accordingly negative. In the case of an idealized Fermi gas model, which is a system of many non-interaction electrons, the Fermi level creates a sharp cutoff in the measured intensity at zero Kelvin. This edge is broadened for $T > 0$ K. The probability of occupation

at the Fermi level $f(E)$ can be described by the Fermi-Dirac distribution:

$$f(E) = \frac{1}{\exp\left(\frac{E-\mu}{k_B T}\right) + 1}. \tag{2.7}$$

The formula contains the Boltzmann constant k_B and the chemical potential μ, which is equal to E_F at $T = 0$ K. Despite the simplification, measured Fermi edges follow roughly the Fermi-Dirac distribution. According to an approximation by the extrapolation of the gradient at E_F the probability of occupation drops from 1 to 0 within an interval of $4k_BT$. It follows that the Fermi edge has a width of about 0.1 eV at room temperature.

2.2.4 Energy Resolution

A sufficiently sharp edge in the intensity profile $I(E_{kin})$ of a photoemission experiment can be used to determine the energy resolution of the setup. Useful features are given with the Fermi edge at low temperatures or the low energy cutoff in the spectrum. The width of the Fermi edge depends on the temperature while the width of the low energy cutoff depends on the distribution of the work function on the surface. The edges can be fitted by means of least squares using a slightly modified cumulative distribution function (2.8) containing the complementary error function erfc (2.9):

$$I(E_{kin}) = \frac{a_0}{2}\mathrm{erfc}\left(\frac{a_1 - E_{kin}}{a_2}\right) + a_3, \tag{2.8}$$

$$\mathrm{erfc}(x) = \frac{2}{\sqrt{\pi}}\int_x^\infty \exp(-t^2)dt. \tag{2.9}$$

Here, a_0 is the magnitude, a_1 defines the position of the step, a_2 reflects the width of the edge and a_3 represents a constant offset. The full width half maximum (FWHM) value of the Gaussian inside the erfc integral represents the energy resolution and is given by:

$$\Delta E = (2\sqrt{\ln 2})a_2. \tag{2.10}$$

2.2.5 Brillouin Zone

Electronic structures are usually evaluated along specific high-symmetry directions of the first Brillouin zone. The first Brillouin zone is the polyhedron primitive cell in reciprocal space (or $\vec{k}$-space) of a single crystal. Due to the periodicity in crystalline solids, the first Brillouin zone suffices to describe the electronic structure. The projection of the three-dimensional Brillouin zone into two dimensions is called surface Brillouin zone. The $\vec{k}$-space containing the surface Brillouin zone can be imaged by low-energy electron diffraction (see figure 2.2 and chapter 2.2.6). An example of the surface Brillouin zone for a body-centered cubic (bcc) system like Fe(110) is shown in figure 2.2. The principal axes k_x and k_y of the surface Brillouin zone may also be named after the combination of symmetry points that span a line in the particular direction (e.g. ($\overline{\Gamma\mathrm{H}}$) or ($\overline{\Gamma\mathrm{N}}$)). Regarding

Fe(110), measuring the electronic structure along ($\overline{\Gamma H}$) or ($\overline{\Gamma N}$) is comparable to some extent with performing angle-resolved photoemission spectroscopy where the angle-sensitive axis lies in the [1$\bar{1}$0] or [001] real-space direction. However, the actually imaged part of the three-dimensional Brillouin zone is located on a spherical surface crossing the [110] axis somewhere between the symmetry points Γ and N because of the non-vanishing momentum component in the [110] direction which in turn depends on the photon excitation energy. Thus, a photoemission measurement can not be directly compared to a standard spectral function or band structure calculation showing only the electronic structure between high symmetry points.

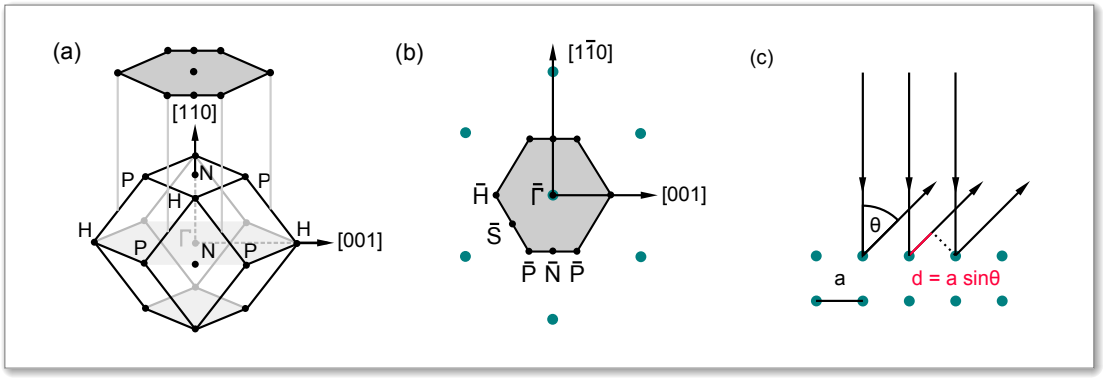

Figure 2.2: (a) First 3D Brillouin zone and (b) surface Brillouin zone of a body-centered cubic lattice in the (110) plane. Black dots represent symmetry points and green dots represent atomic sites in the $\vec{k}$-space (taken and modified from [38, p. 614]). (c) Low-energy electron diffraction at a crystal with lattice constant a. Constructive electron beam interference arises for a path difference d equal to an integer multiple of the electrons' wavelength λ.

2.2.6 Low-Energy Electron Diffraction

The low-energy electron diffraction (LEED) is a measuring method yielding information about the near-surface condition of samples. In this method, a fine electron beam with defined kinetic energy is usually vertically directed onto a sample. The diffracted electrons have an angular intensity dependence originating from interferences due to the wave nature of electrons that are diffracted at different atomic sites and layers (see figure 2.2 (c)). Material-dependent diffraction patterns on a spherical fluorescence screen will emerge, preconditioned that there is adequate atomic order in the probed area. High intensities can be observed under angles that obey Bragg's law:

$$n\lambda = 2\,a\sin(\theta). \tag{2.11}$$

In this equation, the lattice constant of the crystal is called a, the complementary angle of the angle of incidence is θ, λ is the de Broglie wavelength of the electrons and n is a positive integer value.
The observed patterns represent the reciprocal lattice of the sample. The visibility of the features can be influenced by tuning the kinetic energy E_{kin} of the electron beam an thus by changing the wavelength λ according to the de Broglie hypothesis:

$$\lambda = \frac{h}{p} = \frac{h}{\sqrt{2mE_{kin}}}. \tag{2.12}$$

Impurities, lattice irregularities or surface contaminants will show up as perturbations, blurring effects or additional overlapping patterns as described in reference [68]. LEED has become a fundamental method to monitor the near-surface quality of samples.

2.3 Electron Spin

2.3.1 Quantum-Mechanical Description

Almost ninety years ago Uhlenbeck and Goudsmit proposed the spin as an additional intrinsic property of the electron [96]. Observed fine structures in optical spectral lines of gases could be excellently predicted by introducing the additional spin quantum number. The spin $\vec{s}$ itself is a vector with a quantum mechanical property. In quantum mechanics, a complete set of commuting observables describes all quantities that can be physically measured both accurately and simultaneously. Regarding the spin, this set is given by $\vec{s}^2$ and one component, which is usually chosen to be s_z. A measurement of s_z, i.e., a spin-component measurement along the self-defined z-axis direction will always result in $\pm\frac{\hbar}{2}$. Regardless of the initial spin orientation in space, a measurement affects the system and restricts the possible result to $\pm\frac{\hbar}{2}$. This virtually quantized nature of the spin has no classical analog. Due to this fact, a simultaneous measurement of all three spin components becomes impossible. The classical or graphical interpretation of the spin as a vector pointing into an arbitrary direction has its limit here. Nevertheless, the spin is sometimes graphically compared with a rotating vector whose projection onto the z-axis equals $\pm\frac{\hbar}{2}$. In this case, the expectation values of the other components are indefinite due to the ongoing rotation of $\vec{s}$ (see figure 2.3 (a)).
The spin is often compared with a classical angular momentum due to partially similar symmetry properties. In the following paragraphs based on a textbook [43], the spin is described by the three-dimensional spin operator $\hat{\vec{s}} = \{s_x, s_y, s_z\}$. The components satisfy

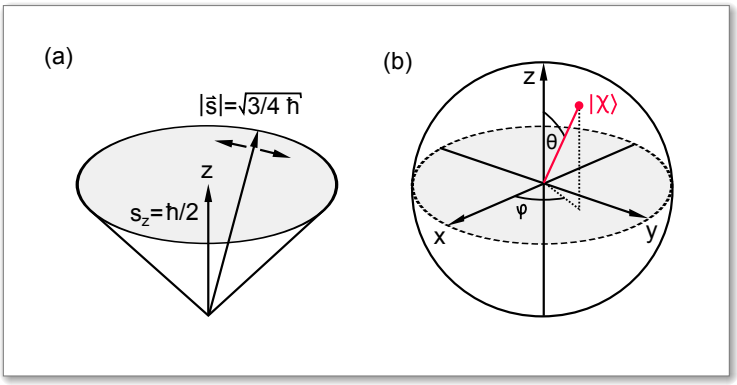

Figure 2.3: (a) Demonstrative projection of the spin $\vec{s}$ onto the z-axis. The spin vector $\vec{s}$ is precessing around the z-axis on a cone-shaped surface and has a length of $\sqrt{3/4}\hbar$. The projection s_z equals $\frac{\hbar}{2}$. The components s_x and s_y are always indefinite due to the precession. They have expectation values of zero. (b) Bloch sphere illustrating the Hilbert space of possible quantum states χ describing the electron spin. All points on the sphere surface correspond to pure spin states. Mixed spin states are represented by points inside the sphere.

the commutation relations as known from the angular momentum:

$$\begin{aligned}
[s_x, s_y] &= s_x s_y - s_y s_x = i\hbar s_z, \\
[s_y, s_z] &= s_y s_z - s_z s_y = i\hbar s_x, \\
[s_z, s_x] &= s_z s_x - s_x s_z = i\hbar s_y.
\end{aligned} \tag{2.13}$$

These commutation relations can be merged into a simple equation (2.15) by defining the Pauli matrices σ_x, σ_y and σ_z:

$$\sigma_x = \begin{pmatrix} 0 & 1 \\ 1 & 0 \end{pmatrix}, \quad \sigma_y = \begin{pmatrix} 0 & -i \\ i & 0 \end{pmatrix}, \quad \sigma_z = \begin{pmatrix} 1 & 0 \\ 0 & -1 \end{pmatrix}, \tag{2.14}$$

$$\vec{s} = \frac{\hbar}{2}\vec{\sigma}. \tag{2.15}$$

For a pure spin state all electrons obtain the same spin function χ with coefficients $a_{1,2}$, where $\binom{1}{0}$ and $\binom{0}{1}$ are the eigenfunction of σ_z:

$$\chi = \begin{pmatrix} a_1 \\ a_2 \end{pmatrix} = a_1 \begin{pmatrix} 1 \\ 0 \end{pmatrix} + a_2 \begin{pmatrix} 0 \\ 1 \end{pmatrix} \quad \text{with} \quad <\chi|\chi> = |a_1|^2 + |a_2|^2 = 1. \tag{2.16}$$

The measurement defines the z-direction so that the observable becomes exclusively σ_z. An interpretation is possible by remembering that experimentally measuring the spin-component s_z is equivalent to mathematically calculating the eigenvalues of s_z. By using the newly defined two-component wave function (2.16) it follows that $\binom{1}{0}$ and $\binom{0}{1}$ are

eigenfunctions to s_z with eigenvalues of $\pm\frac{\hbar}{2}$ (or ± 1 for σ_z) (2.17). They are measured with a probability of $|a_i|^2$. The values $\pm\frac{\hbar}{2}$ are often referred as spin-up or spin-down state of the electron:

$$s_z = \frac{\hbar}{2}\sigma_z \begin{pmatrix}1\\0\end{pmatrix} = \frac{\hbar}{2}\cdot\begin{pmatrix}1\\0\end{pmatrix}, \quad s_z = \frac{\hbar}{2}\sigma_z \begin{pmatrix}0\\1\end{pmatrix} = -\frac{\hbar}{2}\cdot\begin{pmatrix}0\\1\end{pmatrix}. \tag{2.17}$$

The possibility to represent all other spin orientations by this two-component wave function becomes apparent when solving a special eigenvalue equation. In this equation, λ is the eigenvalue and $\vec{e}$ is the unit vector in polar coordinates containing the angles ϕ and ϑ:

$$(\hat{\vec{\sigma}}\cdot\vec{e})\chi = \lambda\chi \qquad \Leftrightarrow \tag{2.18}$$

$$(\sigma_x e_x + \sigma_y e_y + \sigma_z e_z)\begin{pmatrix}a_1\\a_2\end{pmatrix} = \lambda\begin{pmatrix}a_1\\a_2\end{pmatrix} \qquad \Leftrightarrow \tag{2.19}$$

$$\begin{pmatrix}a_1\cos\vartheta + a_2\sin\vartheta e^{-i\varphi}\\ a_1\sin\vartheta e^{-i\varphi} + a_2\cos\vartheta\end{pmatrix} = \lambda\begin{pmatrix}a_1\\a_2\end{pmatrix} \qquad \Leftrightarrow \tag{2.20}$$

$$\begin{pmatrix}a_1(\cos\vartheta-\lambda) + a_2\sin(\vartheta)e^{-i\varphi}\\ a_1\sin\vartheta e^{-i\varphi} + a_2(-\cos(\vartheta-\lambda)\end{pmatrix} = \begin{pmatrix}0\\0\end{pmatrix}. \tag{2.21}$$

The nontrivial solution of equation (2.21) is given by $-\cos^2\vartheta + \lambda^2 - \sin^2\vartheta = 0$ or $\lambda = \pm 1$ which results in one general expression for the eigenfunction of the operator $\hat{\vec{\sigma}}$ covering all possible solutions (phase factors and constants neglected):

$$\chi = \begin{pmatrix}a_1\\a_2\end{pmatrix} = \begin{pmatrix}\cos\frac{\vartheta}{2}\\ \sin\frac{\vartheta}{2}e^{i\varphi}\end{pmatrix}. \tag{2.22}$$

The two eigenfunctions $\left(\begin{smallmatrix}1\\0\end{smallmatrix}\right)$ and $\left(\begin{smallmatrix}0\\1\end{smallmatrix}\right)$ of σ_z (2.17) are a special case of this result where $\vartheta \in \{0, \pi\}$ and $\varphi = 0$ (see figure 2.3 (b)). Spins pointing into the x-axis are given by a coherent and equal superposition of spin-up and spin-down state with $\vartheta = \frac{\pi}{2}$ and $\varphi = 0$ ($a_{1,2} = \frac{1}{\sqrt{2}}$). The y-axis direction is given by $\vartheta = \frac{\pi}{2}$ and $\varphi = \frac{\pi}{2}$ ($a_1 = \frac{1}{\sqrt{2}}$, $a_2 = i\frac{1}{\sqrt{2}}$).

2.3.2 Polarization

A system of many electrons can be characterized by a polarization $\vec{P} = (P_e, P_y, P_z)^T$ (2.23), which describes the average spin direction:

$$\hat{\vec{P}} = <\hat{\vec{\sigma}}> = <\chi|\hat{\vec{\sigma}}|\chi> = (a_1^*, a_2^*)\hat{\vec{\sigma}}\begin{pmatrix}a_1\\a_2\end{pmatrix}. \tag{2.23}$$

Considering the normalization, the value of $|\vec{P}|$ or its components are between 0 and 1. A polarization of 1 represents a pure spin state where all spins are pointing into the same direction, i.e. 100% spin-polarization. A polarization of 0 represents a system with an incoherent superposition of the same amount of spin-up ($N^{\uparrow}$) and spin-down states ($N^{\downarrow}$).

The polarization along the z-direction is given by:

$$P_z = \frac{|a_1|^2 - |a_2|^2}{|a_1|^2 + |a_2|^2} = \frac{N^{\uparrow} - N^{\downarrow}}{N^{\uparrow} + N^{\downarrow}}. \tag{2.24}$$

This is in contrast to a coherent and equal superposition of spin-up and spin-down states, which would lead to a completely polarized beam with the polarization lying in the perpendicular plane.

The polarization of an electron ensemble (e.g. a consistently polarized electron beam) along all directions can be determined as long as the measurements are performed separately within different subsystems. However, a subsequent measurement of several polarization components of the same electrons would lead to invalid results. The first polarization measurement prepares the spins, leading to a result in the second measurement that is not identical to the original state. It may be important to consider relativistic electron energies E. They reduce P_z in the laboratory system by the factor $\frac{mc^2}{mc^2+E}$ [45, p. 6]. Here, m is the electron mass and c is the speed of light. For low-energy electrons with 10 eV, the reduction will be only 0.002% and thus negligible.

2.3.3 Ferromagnetism and Exchange Interaction

The spin of the electron is coupled to a magnetic dipole moment $\vec{\mu_s}$ (2.25). A parallel arrangement of the magnetic moments and spins, respectively, is the reason for the net magnetization in ferromagnets. The proportionality factor g_s relates the spin $\vec{s}$ to the magnetic moment $\vec{\mu_s}$ and is called Landé- or g-factor. Here, $\gamma = \frac{g_s \mu_B}{\hbar}$ is the gyromagnetic ratio, $\mu_B = -\frac{e\hbar}{2m_e}$ is the Bohr magneton and m_e the electron mass. In contrast to the electron orbit magnetic moment where the proportionality factor is 1, for g_s it is approximately 2. The magnetic dipole moment of an electron is given by:

$$\vec{\mu_s} = \gamma \vec{s}. \tag{2.25}$$

Ferromagnetic materials exhibit a magnetization due to a spontaneous collective parallel alignment of their magnetic moments. This is noticeable by an unbalanced distribution of spin-up and spin-down states or a polarization at the Fermi level in the density of states. Looking at the band structure, iron shows a spin split $3d$ band for example. Ferromagnetism is a quantum-mechanical effect caused by the exchange interaction. It is based on the Pauli exclusion principle and the indistinguishability of identical particles like electrons. The consequences are unpaired electron spins and partially filled shells of the atoms.

Ferromagnetism can be explained by looking at a simplified two-electron wave function $\Psi(\vec{r_i}, s_{zi})$ that can be rewritten as a product of its spatial wave function $\Phi(\vec{r_i})$ and spin wave function $\chi(s_{zi})$ (2.26). According to the spin-statistics theorem, the total wave function of indistinguishable fermions must be antisymmetric under particle permutation. This is possible with a symmetric spatial wave function and an antisymmetric spin wave

function or vice versa. The spatial wave function must be entangled in order to be either symmetric or antisymmetric:

$$\Psi((\vec{r_1}, s_{z1}), (\vec{r_2}, s_{z2})) = \Phi(\vec{r_1}, \vec{r_2})\chi(s_{z1}, s_{z1}), \tag{2.26}$$

$$\Phi(\vec{r_1}, \vec{r_2}) = \frac{1}{\sqrt{2}}(\varphi_A(\vec{r_1})\varphi_B(\vec{r_2}) \pm \varphi_A(\vec{r_2})\varphi_B(\vec{r_1})). \tag{2.27}$$

As a consequence, calculating the potential energy expectation value of Ψ will lead to an additional term called exchange energy. It has either a positive or a negative sign, depending on the symmetry of the Φ. A negative sign would correspond to an energetically favorable state. It requires Φ to be antisymmetric so that χ has to be symmetric. A symmetric χ corresponds to a parallel spin alignment. However, one electron must occupy a higher and energetically disadvantageous state, since two electrons with the same spin orientation cannot occupy the same state. In contrast to that, an antisymmetric Φ comes along with a greater average electron-electron distance and a lower Coulomb repulsion. Only if this aspect energetically overcompensates the electron configuration effect, ferromagnetism will arise spontaneously.

2.3.4 Electrons in Magnetic Fields

The magnetic moment of the spin will experience a torque when exposed to an external magnetic field H. The associated magnetization M of an ensemble will therefore start to precess around the field axis with a frequency of ω:

$$\omega = -\gamma B \approx \frac{e}{m}B. \tag{2.28}$$

The rotational motion can be described by the Landau-Lifschitz-Gilbert equation, which contains the damping factor λ:

$$\frac{dM}{dt} = -\gamma M \times H - \lambda M \times (M \times H). \tag{2.29}$$

In ferromagnetic solids, an external magnetic field can potentially force the self-aligned magnetic moments inside the magnetic domains to realign along the direction of the external field. A stable remanent magnetization reaching across several domains can remain even after switching off the external field. The realignment process comes along with a damped precession of the individual magnetic moments (see black line in figure 2.4 (a)). The damping is caused by the interaction of the spin with other electrons, spins or phonons (e.g. lattice vibrations or spin-waves). The precession frequency is dependent on the amplitude of the magnetic field while the material dependent damping determines the speed of the realignment.
In this context, free electrons as found in a beam usually have a negligible damping factor. The magnetic moments or rather the electron spins that are exposed to a magnetic

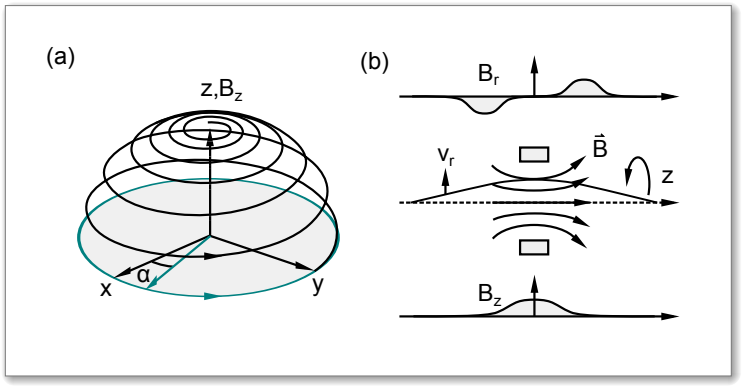

Figure 2.4: (a) Illustration of the spin precession around B_z. The tip of the spin vector follows the black line (with damping) or the green line (without damping). The dynamics of a polarization vector may look slightly different e.g. due to dephasing effects. (b) The field of a magnetic lens influences the electron trajectory. A beam rotation occurs due to the Lorentz force (direction indicated by the curved arrow). A focusing effect will additionally arise. The radial and longitudinal components of the magnetic field generated by a coil are schematically drawn on the top and bottom (taken and modified from [20, p. 36 ff.] and [29, p. 94]).

field will therefore simply rotate around the field axis without any realignment along the magnetic field (see green line in figure 2.4 (a)). The apparent rotation of the spins or the polarization is quantum-mechanically caused by a collective phase change of the quantum states. This is reflected in a measurable rotation of an initial polarization. Electron-optical elements can therefore be designed to manipulate the spin polarization freely [18]. The spin rotation angle α around the field axis is dependent on the value of the electron velocity $\vec{v}$ and the magnetic field $\vec{B}$ over which it interacts with the magnetic moment:

$$\alpha = \frac{e}{m_e v} \int B_z dz. \tag{2.30}$$

A simple solution of the integral is given by approximating the magnetic field as uniaxial along the z-axis and as a step function with width l and height B_0. Equation (2.30) will then result in $\alpha = \frac{leB_0}{m_e v}$. The polarization changes according to equation:

$$\vec{P}_{rot} = (P_e \cos\alpha \mp P_y \sin\alpha, P_y \cos\alpha \pm P_e \sin\alpha, P_z). \tag{2.31}$$

However, in real experiments electron optical elements are usually used to focus electron beams, which generates a small radial velocity v_r (see figure 2.4 (b)). The Lorentz force $\vec{F_L} = -e(\vec{v} \times \vec{B})$ can thus cause a spiral motion of the beam in addition to the spin rotation. This image rotation angle Φ is given by equation (2.33) [20, p. 43]. The rotation angle depends on the kinetic energy E_{kin} of the electrons. The integral over B_z is used since a real magnetic field amplitude generated from a coil is especially inhomogeneous

at the border region. The Lorentz force can therefore act in further directions so that the magnetic field has also a focusing effect (magnetic lens) with focal length f (for more details see [20, p. 34 ff.]):

$$\frac{1}{f} = \frac{e^2}{8m_e E_{kin}} \int B_z^2 dz, \tag{2.32}$$

$$\text{with } \Phi = \frac{e}{\sqrt{8m_e E_{kin}}} \int B_z dz = \frac{e}{2m_e v} \int B_z dz. \tag{2.33}$$

It is obvious that the image rotation Φ is exactly half the value of the spin rotation described by equation (2.30). A more precise description of the magnetic field along the z-axis for a short coil is given by a Lorentzian-shaped distribution (2.34). In this case, the integral of equation (2.32) can be analytically solved (2.35). In the solution, B_0 is the maximum field amplitude and $2a$ is the FWHM value of B_z [20, p. 41]:

$$B_z = \frac{1}{1 + \frac{z^2}{a^2}} B_0, \tag{2.34}$$

$$\int_{-\infty}^{\infty} B_z^2 dz = \frac{\pi}{2} a B_0^2. \tag{2.35}$$

2.3.5 The Fe/W(110) System

Tungsten and iron crystals form a bcc lattice structure. Tungsten substrates can be easily cleaned with a standard heating procedure. Cycles of low power flashes to 1500 K at around $6 \cdot 10^{-8}$ mbar partial pressure of oxygen and a final high power flash to 2200 K will remove not only iron but also carbon, oxygen and oxides of carbon. This will produce an atomically clean surface [107]. Thin single-domain iron films can be deposited on tungsten by molecular beam epitaxy. Usually, a high-purity iron rod is therefore sublimated by heating it through electron bombardement.

The lattice constant a of relaxed tungsten and iron is 316.52 pm and 286.65 pm, respectively. This corresponds to a layer distance of $\frac{\sqrt{2}}{2}a$ in the (110) plane. The lattice mismatch of 9.4% between tungsten and iron affects the growth of the first few iron monolayers. According to the coverage $\theta = \left(\frac{a_F e}{a_W}\right)^2 = 0.82$, a relaxed monolayer of iron would only cover 82% of tungsten. This has to be taken into account when calculating layer thicknesses from deposition rates.

There are mainly three modes of thin-film growth. The Volmer-Weber growth mode represents the formation of adatom clusters or islands. The Frank-van der Merwe mode represents a layer-by-layer growth, while the Stranski-Krastanov mode shows both layer-by-layer and island growth. The Stranski-Krastanov growth mode is typical for the Fe/W(110) system. Growth mode and surface quality can be influenced by additional annealing during or after the deposition. An annealing around 500-600 K is suitable to improve the Fe/W(110) surface quality. At this temperature no agglomeration occurs, but

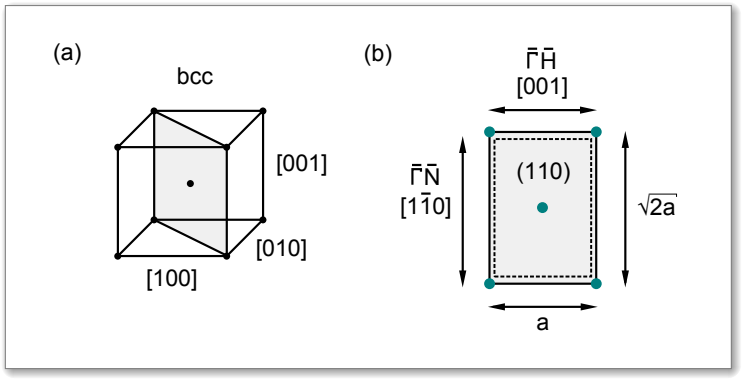

Figure 2.5: (a) Body-centered cubic lattice with marked (110) plane. Black dots represent atomic sites in real-space. (b) Lattice constant a mismatch between relaxed tungsten (solid line) and iron (dashed line). Green dots represent atomic sites of tungsten.

the atom diffusion is maximized and the nucleation is minimized.
At room temperature, the first monolayer of iron grows pseudomorphically on W(110) in a step-flow growth mode starting from the tungsten step edges. After completion of the first layer the second monolayer grows mostly pseudomorphically with irregularly spaced dislocation lines along [100]. The third layer growth is energetically unfavorable. With a thickness of 4 monolayers a two-dimensional dislocation network arises and starts to relax the lattice mismatch. The bcc lattice is then close to the bulk lattice constant form [28].
The easy magnetization axis of Fe/W(110) depends on the iron film thickness. It has an in-plane easy magnetization axis along [1$\bar{1}$0] for films thinner than a critical thickness of 30 to 50 monolayers. For narrow double layer stripes one observes an out-of-plane magnetization along [110] (see reference [23]). The Curie temperature of a pseudomorphic monolayer is around 230 K [24] and increases to values above room temperature beyond 1.4 monolayers [3]. The easy axis changes to the in-plane direction along [001] for iron films with thicknesses above 30 to 50 monolayers [53].
The coercive field of an Fe(110) film decreases with increasing thickness and approaches 1.2 mT above 15 monolayers [61]. At the same time the spin polarization of secondary electrons created by an electron gun increases with the film thickness. The spin polarization is highest for iron thicknesses above 15 monolayers [61] and secondary electrons at kinetic energies between 0 and 4 eV. It reaches around 45% for a primary beam energy of 0.8-2.0 eV [1,49]. In experiments, the spin polarization decreases with time because of the unavoidable residual gas adsorption influence. The intensity of secondary electrons has a maximum around 600 eV primary beam energy [49].
Generally, the iron films can be passivated by the adsorption of oxygen. Different superstructures are possible depending on the preparation procedure. To obtain a primitive (2×2) superstructure (Fe(110)p(2×2)O), the iron film has to be exposed to 1 to 3 L of oxygen and subsequently annealed at 550 K [26] [103].

2.3.6 Magneto-optic Kerr Effect

The magneto-optic Kerr effect (MOKE) describes the changes in polarization and intensity of light reflected at magnetized surfaces. The effect is based on the anisotropic permittivity triggered by the magnetization of the target. An illustrative explanation is given by considering the Lorentz force. The electron oscillation in the target caused by linear polarized light, for example, is affected by the magnetization. Depending on the alignment between magnetization and light polarization, an oscillation component perpendicular the polarization of the incident light can arise and change the polarization vector orientation of the reflected light. The resulting Kerr angle can be used to analyze the magnetization of a sample or to image magnetic domains.
There are three important experimental geometries where the analyzed magnetization vector is either perpendicular to the sample surface (polar MOKE), parallel to the surface but perpendicular to the plane of incidence (transversal MOKE) or parallel to the surface and the plane of incidence (longitudinal MOKE). These geometries are usually combined with s- or p-polarized light.
For the longitudinal MOKE setup, s-polarized light with a polarization perpendicular to the plane of incidence and parallel to the target plane is usually used. A rotation of the polarization vector can be observed after the reflection. A photodiode with an analyzer perpendicular to the s-polarization should therefore measure a small intensity if the target causes a Kerr-rotation. To precisely analyze this signal, the lock-in technique is needed. The light is therefore transmitted through an AC-powered Faraday rotation modulator before the reflection. This causes the measured intensity signal to oscillate with the AC frequency. The lock-in amplifier processes this signal and supplies the modulator with an additional constant voltage that gradually compensates the Kerr-rotation caused by the target. If the Kerr-rotation is fully compensated, the signal will oscillate with a doubled AC frequency because the intensity becomes minimum when the analyzer is exactly perpendicular to the incoming polarization. The constant voltage part that is needed to observe the doubled frequency represents the measuring signal and is proportional to the Kerr-angle.

2.4 Spintronics

2.4.1 Spin Transport

Preventing the fast spin relaxation and maintaining or transporting the spin information over time and distance is a demanding task. There are four principal mechanisms for spin-relaxation in the bulk. Their contribution to the total relaxation is dependent on the materials. The Bir-Aronov-Pikus mechanism [10] describes the exchange interaction and scattering at electron holes. Spin flip events due to electron scattering at phonons and crystal defects are described by the Elliott-Yafet mechanism [22,106]. The Dyakonov-Perel mechanism [19] described the spin precession in effective magnetic fields due to band

splitting. Finally, the hyperfine interaction contributes to a spin dephasing through the effective magnetic field of the nuclear spins that interact with the electron spins. In metal-organic interface materials, spin-polarized currents can be injected from the substrate into the surface layer to improve the spin transport properties. In the organic molecule, hopping among defect states or the highest and lowest occupied molecule orbital (HOMO/LUMO) enable the spin transport. In this context, an important measure is the spin diffusion length which defines the distance over which an injected spin population decays by $\frac{1}{e}$ due to spin relaxation. For transition metals, the inverse spin diffusion length is proportional to the number of unoccupied d-orbitals [79]. Typical spin injectors are ferromagnetic metals with a high spin polarization at the Fermi edge. The dominant spin relaxation mechanisms is still not conclusively identified [4].

2.4.2 Metal-Organic Interfaces

Ferromagnetic-organic interfaces are potential spintronic materials. A large spin diffusion length is essential for spintronics. The interaction of ferromagnetic substrates with organic molecules can lead to larger spin diffusion lengths because the light elements with low atomic number exhibit weak spin-orbit coupling and reduce the strength of the spin relaxation. Their production can be relatively cost-efficient and simple by using thermal evaporation.

The precondition for the substrate of the interface is a non-equilibrium of spin-up and spin-down states at the Fermi energy as found in iron. It induces the possibility to inject spin-polarized currents from the ferromagnet (e.g. iron) into coatings of organic materials, semiconductors or metals. This effect is called spin-injection. The injection efficiency depends on the interface and can be tuned through chemical modification of the molecules for example. In comparison to metallic conductors, the spin injection and transport properties of these hybrid interface materials in terms of spin coherence over time and distance can be improved.

The electronic structure of both, substrate and organic molecule, generally changes dramatically by bonding interactions. While physisorption leads to normalization and broadening of the electronic structure of isolated molecules, the additional planar chemisorption of organic molecules on metals can cause charge transfers and hybridizations. A hybridized $\pi - d$ interface can emerge with iron as substrate for example. Overall, the measurable density of states is changed [60] and superimposed by additional molecular and interface states (see figure 2.6).

In organic molecules, the HOMO and the LUMO level play a major role for the electronic structure of the interface. A reliable prediction of emerging energy levels as possible for non-organic interface systems on the basis of the Schottky-Mott limit rule [42] of vacuum level alignment is not suitable. Deviations from the model come from charge exchange, Fermi level pinning and metal-surface modifications according to reference [42].

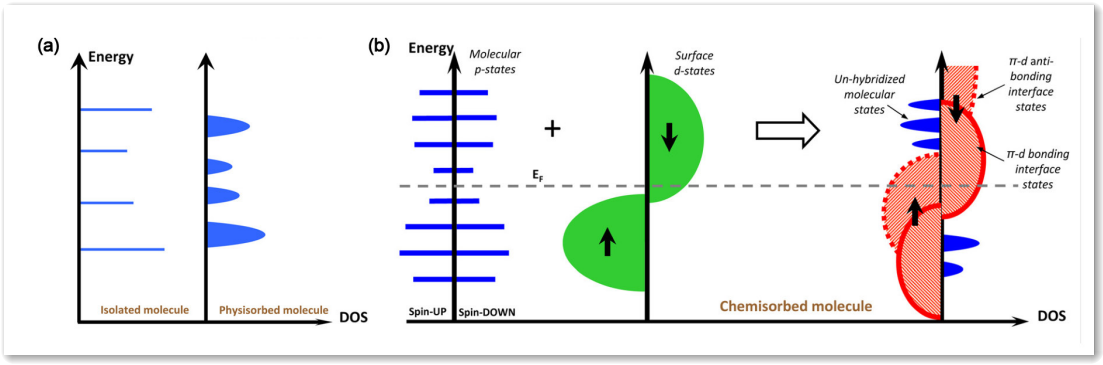

Figure 2.6: (a) Broadening of molecule states due to physisorption. (b) Schematics of the formation of (un-)hybridized π-d interface states due to chemisorption. The image is taken from [72].

2.5 Photoemission Spectroscopy

2.5.1 General Description

Photoemission spectroscopy is a unique measurement technique which leads to fundamental insights on the electronic properties of analyzed samples. In combination with a low-energy excitation sources such as VUV lamps the technique is often called ultraviolet photoemission spectroscopy (UPS or PES). Charging of the sample should be prevented during the excitation process. In this established technique, the electron energies E and emission angles θ in one azimuthal plane can be measured simultaneously if needed. Measured $E - \theta$ diagrams can be converted into $E - k_{||}$ diagrams and reveal a part of the materials spectral function within the first Brillouin zone.
Disregarding transition probabilities and further side effects, the electronic bands (or density of states if measured angular-integrated) can be reflected by plotting the number of emitted electrons against their measured kinetic energy. This principle corresponds to equation (2.1) and is shown in figure 2.7. Cross sections of the surface Brillouin zone can be analyzed by measuring two-dimensional energy- and angle-resolved intensity maps. The associated measurement is then called angle-resolved photoemission spectroscopy (ARPES). Spin-resolved spectra can be obtained by employing a spin filter. It is called spin- and angle-resolved photoemission spectroscopy (SARPES). Other techniques like the time-of-flight momentum microscope can measure energies and two momentum components simultaneously [80].
A pronounced feature in each photoemission spectrum is the occurrence of secondary electrons. Secondary electrons possess low energies by trend due to inelastic scattering processes inside the sample. They are observable as a broad and intense feature above the low energy cut-off in each spectrum. Despite the fact that the measured spectra of the electronic structures are covered with a background, the secondary electrons can be helpful in certain cases. Due to the high intensity of this part of the spectrum it can be

used for adjustment purposes of the experimental setup. The high spin polarization of secondary electrons produced by a combination of an electron gun and a magnetized iron target, for example, can also serve as a polarized electron source [49].

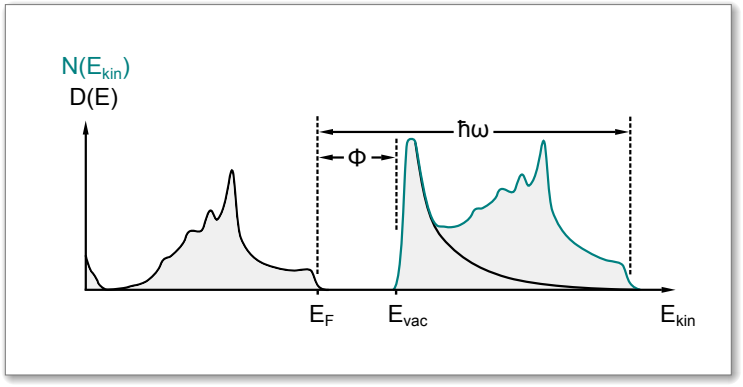

Figure 2.7: The density of states is outlined on the left. Electrons are excited with $\hbar\omega$ to overcome the work function Φ. In angular-integrated mode, the measured kinetic energy spectrum on the right resembles the density of states. The contribution from the intrinsic spectrum and the inelastic background by secondary electrons merge into the measured curve (green)

It is necessary to point out several important aspects of PES (cf. [37, p. 14-16]). Photoemission spectra always show a mixture of surface and bulk properties according to the inelastic mean free path (see 2.5.3). Furthermore, the probed sample is not in the ground state because the continuous excitation generates positive holes. Another aspect is the assumed momentum conservation for $k_{\|}$ which is not exact. Also selection rules for optical transitions have to be taken into account when trying to understand photoemission spectra. Finally, the effect of the imperfect sample surface on electromagnetic field of the photons is unclear.

2.5.2 Electron Excitation Source

The excitation process in photoemission can be performed with different photon sources. Usually, most of the excited electrons remain in the solid because of inelastic interactions and scattering processes. Technically, the requirements for an electron excitation source are a suitable photon energy, monochromaticity and a high intensity (avoid space-charge) on a small spot size and a low angular divergence. The unified measure of quality is called brilliance. Frequently used light sources alongside lasers, radiation from synchrotrons and x-ray tubes are rare-gas discharge lamps that emit vacuum ultraviolet (VUV) light. VUV light has an energy $\hbar\omega$ of >10.5 eV (the cutoff energy of LiF) and requires vacuum because it will be blocked by air or conventional glass. VUV gas-discharge lamps with Hydrogen ($\hbar\omega = 10.2$ eV), Argon ($\hbar\omega = 11.62$ eV or 11.83 eV) or Helium ($\hbar\omega = 21.22$ eV or 40.81 eV) are very popular. Undesired spectral lines can be blocked by ionic crystal filters [88].

2.5.3 Inelastic Mean Free Path

The escape depth of electrons excited by VUV-lamps is in the order of nanometers, even though the penetrated volume of the light can be greater. In the energy range that can be obtained with VUV-lamps the electron-electron interaction is mainly responsible for the escape depth characteristics. The inelastic mean free path (IMFP) is the energy dependent distance at which the intensity of an electron beam decays to $\frac{1}{e}$ or 37 percent of its initial value. Universal mean free path curves describe these characteristics (see figure 2.8). One should note, that the universal curve is rather approximative. Experimentally determined values may vary by more than a factor of two from the universal curve in particular on the low energy side. The IMFP is also spin-dependent. Most of the excited electrons originate from the first few monolayers of the sample when using H, Ar, or He gas-discharge lamps. Therefore, VUV lamps provide the possibility to perform relatively surface-sensitive measurements.

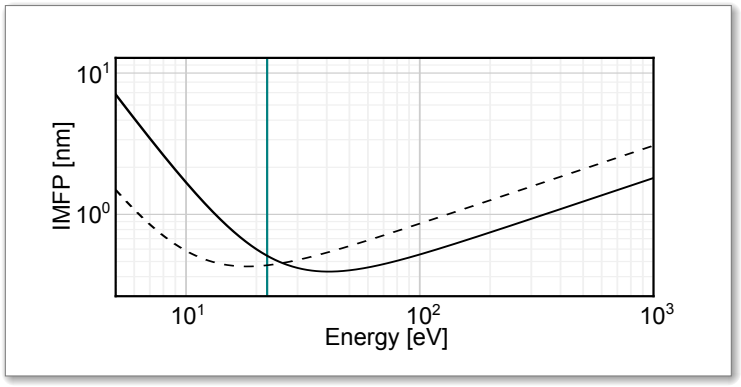

Figure 2.8: Energy dependent universal curve of electron mean free path for elements (solid line) and organic compounds (dashed line) [82]. The minimum IMFP with values of less than 0.5 nm are located at excitation energies of approximately 18 eV and 41 eV according to this curve. The vertical green line marks the first energy of the frequently used Helium emission line.

In ARPES experiments, the intensity of electrons escaping under large angles should decrease by a cosine law because of longer electron escape paths. For most spectrometers, this effect is very small due to a limited angular acceptance of typically $\pm 15°$ at maximum.

2.5.4 Models of Photoemission

A simple phenomenological formulation of the photoemission process is covered by the three-step model (see left figure 2.9). It is divided into the photoexcitation of electrons, the electron transport to the surface and the escape through the surface into the vacuum (cf. [37, p. 50-51, 349-357]). Since VUV photons have a negligible momentum, this model assumes direct or vertical momentum transitions in the reduced zone scheme with

backfolded bands from outside the first Brillouin zone. Here, the initial parallel momentum is equal to the final momentum ($k_{\parallel i} = k_{\parallel f}$). However, according to the reduced zone scheme many direct transitions would be impossible due to the lack of final states. In order to fulfill energy and momentum conservation a reciprocal lattice vector $\vec{G}$ must be involved in the photoexcitation step. The lattice vector provides the required crystal momentum change enabling direct transitions ($\vec{k_f} = \vec{k_i} + \vec{G}$). Treating electrons in the sample as free particles, the energy conservation defines the angle between $k_{\parallel i}$ and $\vec{G}$. The possible combinations of $k_{\parallel i}$ and $\vec{G}$ lead to cone-like structures in a diagram and are therefore called Mahan cones (cf. [15, p. 163-164]). Another problem of the three-step model is the violation of the uncertainty principle. A correct description of the photoemission process is given by the one-step model (see [37, p. 349-350] for more details) describing the process with a partially damped Bloch wave (see right figure 2.9).

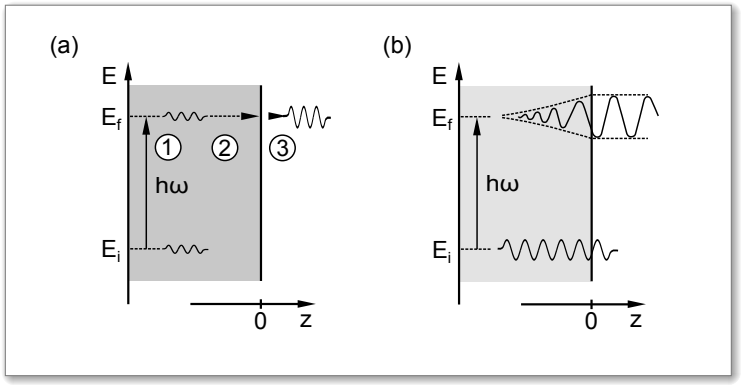

Figure 2.9: (a) Three-step model with photoexcitation from initial state energy E_i to final state energy E_f (1), transport to surface (2) and escape (3). (b) One-step model with the excitation of the Bloch wave in the crystal to a damped final state (taken and modified from [37, p. 350]).

2.5.5 Experimental Setup

The experimental setup for photoemission depends on the number of measured properties. In the case of energy- and angle-resolved photoemission, a frequently used technique is based on a hemispherical analyzer. In this type of analyzer, the excited electrons are captured and transferred from the sample to a narrow entrance slit of an energy analyzer by an electron optical system. The hemispherical analyzer is in principle composed of two interleaved hemispheres. A voltage is applied so that an attractive force pointing to the inner hemisphere is created. When passing the entrance slit, the electron bunch is dispersed in one direction by means of energy because of their different trajectory radii when passing the interspace of the hemispheres. The corresponding dispersion direction is labelled as energy-dispersive axis.
The emission angles of the excited electrons are also transferred to the hemispherical an-

alyzer. However, the thin entrance slit allows only angles along one direction to enter the hemispherical analyzer. This direction is perpendicular to the energy-dispersive axis. As a result, a two-dimensional image resolved in angle and energy arrives finally at the exit plane (see red parts of figure 2.16).
The maximum energy resolution ΔE_{an} is dependent on the entrance slit width d, the mean radius of the hemispheres R_0, the average angular width α of the electron distribution and the energy acceptance of the analyzer given by the pass energy E_p and defined by the applied voltages [58, 84]:

$$\Delta E_{an} = E_p \left(\frac{d}{2R_0} + \alpha^2 \right). \tag{2.36}$$

In the case of very small excitation spot sizes on the sample the spot footprint may determine the value d so that the resolution can be further improved. The average angular width α can be calculated by using the total linear magnification M of the electron optical lens, the acceptance angle α_{acc} of the spectrometer and the ratio between E_{kin} and E_p [58]:

$$\alpha = \arcsin \left(\frac{\sin(\alpha_{acc})}{M} \sqrt{\frac{E_{kin}}{E_p}} \right). \tag{2.37}$$

For hemispherical analyzers, the intensity of the resulting $E - \theta$ pattern in in the exit field is proportional to $\frac{E_p^2}{E_{kin}}$ and d. The intensity and thus the measurement speed can be increased at the expense of resolution.
Typical acceptance angles for hemispherical analyzers are $\pm 15°$ at maximum. A high angular resolutions of $0.1°$ is obtained for smaller acceptance angles. The energy acceptance is usually defined by 10% of the pass energy E_p. Depending on the spectrometer settings, an energy resolution of <3 meV can be obtained.

2.6 Spin-Resolved Photoemission Spectroscopy

2.6.1 Principle of Spin Filtering

Spin-dependent scattering processes are used in spin-resolved photoemission spectroscopy to determine a polarization component P of an electron beam. Looking at the scattering interactions between free electrons and surfaces, the spin-orbit interaction and the exchange interaction are the predominant effects. A crystalline ferromagnetic target is needed for strong exchange interaction. Strong spin-orbit interaction is achieved with targets made of high-Z materials. Even though both effects are always present at the same time, there are conditions in which one of them dominates the interaction.
To unambiguously determine one polarization component of an electron beam it is required to use the correct geometry of the experiment or to employ a scattering setup which is only sensitive to one axis. Otherwise, the influence of the other components can mask the result for the wanted component. Depending on the employed scattering method, sensitivity limitations may originate from intrinsic scattering properties or can arise from

special geometries (explanation given in subsections 2.6.2 and 2.6.3). Spin-polarized low-energy electron diffraction (SPLEED) at crystalline targets is exclusively sensitive to the component normal to the scattering plane when a mirror plane of the crystal coincides with the scattering plane. For polycrystalline targets (e.g. Mott scattering), no favourable interferences for large reflectivities are available. Here, the spin-dependent scattering is always sensitive to the component normal to the scattering plane. This is independent from the target orientation since every scattering plane coincides with a mirror plane. The sensitivity of exchange scattering is intrinsically given by the direction parallel to the scattering target magnetization. Figure 2.10 illustrates a typical setup with a sensitivity normal to the drawing plane.

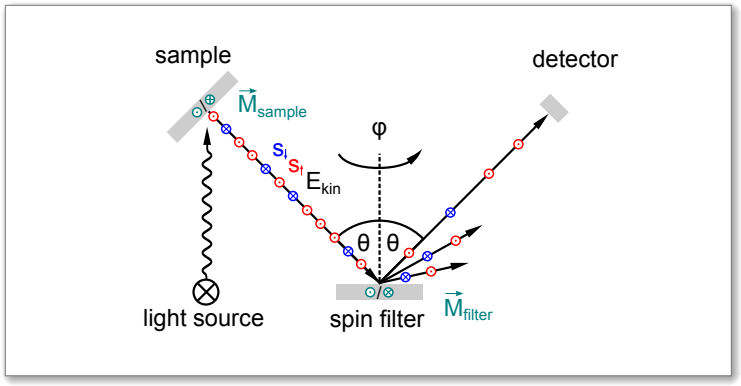

Figure 2.10: A polarized electron beam is photoemitted from a sample. If the sample is magnetized ($\vec{M}$ in green) the electron spins are aligned with respect to each other (red and blue vectors normal to the drawing plane). The beam is elastically scattered under the angle θ. The azimuth ϕ and the not shown polar angle or inclination ϑ (usually 0°) of the target can be adjusted. Non-specular electrons illustrate further diffraction spots. Depending on the method, either target or sample can be non-magnetic. For Mott scattering at an amorphous target, the angle of incidence is usually 0° and two mirror-symmetrically mounted detectors are used (sample and target may then be non-magnetic). For SPLEED, the initial beam polarization can be inversed or experimental parameters have to be adjusted for a polarization analysis. For the spin polarization analysis with exchange interaction, the scattering target magnetization is reversed.

In a spin-resolving experiment, the intensity of the scattered electron beam is measured. Depending on spin-dependent scattering effect, this is done at (i) different scattering conditions, (ii) geometries or (iii) magnetization directions. This will give rise to an intensity asymmetry A. Each scattering condition is related to a different spin-dependent cross section. In Mott scattering and sometimes also in SPLEED [46], two mirror-symmetrically mounted detectors are used. Here, the electron beam approaches the target normal to the surface and the non-specularly backscattered beam intensities are measured at the

detectors. For scattering experiments with mainly exchange interaction, only one detector for measuring the specular beam is usually employed. Here, the magnetization of the spin filter is reversed to determine the spin polarization. For spin-orbit interaction combined with SPLEED, the experimental parameters can be adjusted to change the scattering condition and subsequently measure a second intensity to obtain the asymmetry. Depending on the method, adjustable parameters are given by the scattering energy E_{scatt}, the polar or azimuthal target angle ϑ or φ, the scattering angle θ, the detector position, the scattering target magnetization or the reversal of the initial beam polarization. The reversal methods have the great advantage, that they redundantize reflectivity $R = \frac{I}{I_0}$ corrections, which are mostly needed upon variation of the other parameters (exceptions are possible mirror symmetries in SPLEED or in Mott scattering). Additionally, the inherent relatively high asymmetry results in better signal-to-noise ratios. The polarization reversal of the incident beam is possible by using a spin-rotator lens, by a reversal of the ferromagnetic sample magnetization or by switching the photon helicity of the excitation source (if applicable for the sample). The reversal method is therefore most frequently used.
In a simple example, the measured intensities of $N_\uparrow$ spin-up and $N_\downarrow$ spin-down electrons after scattering are given by $I_i = R_i(N^\uparrow(1 \pm S_i) + N^\downarrow(1 \mp S_i))$. Here, R_i is the reflectivity with a value between 0 and 1 (for low-energy scattering at crystals defined by LEED spots) and S_i is called Sherman function and quantifies the analyzing power of the setup with a value between 0 and 1. The calculation of the asymmetry A between these intensities is directly proportional to the initial beam polarization P. Creating an asymmetry by exploiting an initial beam polarization inversion so that $S_2 = S_1$, the reflectivity remains constant ($R_1 = R_2$) and the expression of the asymmetry simplifies to the following equation:

$$\begin{aligned} A &= \frac{R(N^\uparrow(1+S) + N^\downarrow(1-S)) - R(N^\uparrow(1-S) + N^\downarrow(1+S))}{R(N^\uparrow(1+S) + N^\downarrow(1-S)) + R(N^\uparrow(1-S) + N^\downarrow(1+S))}, \\ &= S\frac{N^\uparrow - N^\downarrow}{N^\uparrow + N^\downarrow} = SP. \end{aligned} \tag{2.38}$$

Thus, the polarization can be directly calculated if the Sherman function is known from a calibration. The Sherman function can be determined by a double scattering experiment [43, p. 71-74] or by calibrating the setup with a known initial beam polarization. It should be noted that the measured reflectivity is generally decoupled from the Sherman function. While S essentially depends on the properties of the single atoms, the reflectivity depends on the coherent summation of the scattered amplitudes [45, p. 20]. Multiple-scattering effects contribute to both values.

2.6.2 Exchange Scattering

The exchange interaction involves a scattering process between valence electrons of the target and free electrons. An unpolarized beam will become polarized in the direction of

the target magnetization [45, p. 28]. The effect is a consequence of the Pauli principle. In another simplistic case, polarized electrons are scattered under a scattering angle $\theta > 0$ at a polarized ferromagnetic target whose valence electron spins are initially either parallel or anti-parallel to the spins of the incident beam (see figure 2.10). An unequal scattering amplitude will be the result for the different relative spin orientations. The cross sections can be derived from scattering theory using antisymmetric wave functions according to the Pauli principle [43]. The resulting scattering channels lead to expressions for the total cross sections which are finally different [25]. Mathematically, the so-called exchange amplitude is responsible for this difference. It describes the capture of the incident electron by the atom and the ejection of the oppositely polarized atomic electron. In contrast to the spin-orbit interaction where the left-right asymmetry as shown in figure 2.11 entails $-A_{SO}(\theta) = A_{SO}(-\theta)$ [45, p. 11], the asymmetry in exchange interaction changes according to $A_{ex}(-\theta) = A_{ex}(\theta)$ for complementary scattering angles [45, p. 16]. There is also no azimuthal dependence of the cross section and polarization components of non-relativistic electrons lying in the scattering plane do not contribute to the asymmetry [45, p. 16].

2.6.3 Spin-Orbit Scattering

The spin-orbit interaction is particularly pronounced in the scattering of electrons at heavy, non-magnetic materials [45]. The importance of a scattering target with high Z becomes clear by looking at the Dirac equation with a non-relativistic approximation describing electron movements [43]:

$$(\mathcal{H} + \mathcal{H}_B + \mathcal{H}_\nabla + \mathcal{H}_{SL})\Psi = E\Psi, \tag{2.39}$$

$$\mathcal{H}_{SL} = -\frac{e\hbar}{4m^2c^2}\hat{\sigma} \cdot (\hat{E} \times \hat{p}), \tag{2.40}$$

$$= \frac{Ze^2}{2m^2c^2}\frac{1}{r^3}(\hat{s} \cdot \hat{l}). \tag{2.41}$$

The equation consists of a term $\mathcal{H}$ describing the interaction with external fields which is also found in the Schrödinger equation, $\mathcal{H}_B$ for the interaction between a magnetic dipole and an external magnetic field, a term $\mathcal{H}_\nabla$ with a relativistic correction to the energy and $\mathcal{H}_{SL}$ for the influence of the spin-orbit coupling. E stands for the energy and Ψ consists of two two-component spinors representing the spin state of the particle.
The $\mathcal{H}_{SL}$ term from (2.39) is also called spin-orbit energy and can be transformed from equation (2.40) to (2.41) in several steps. First, replacing the Pauli operator $\hat{\sigma}$ with $\frac{2}{\hbar}\hat{s}$ will include the dependency of the spin operator $\hat{s}$. By using $\hat{E} = -\frac{1}{e}\frac{dV}{dr}\frac{\hat{r}}{r}$ for a motion in a central Coulomb potential $V(r) = -\frac{Ze^2}{r}$ the dependence on the atomic number Z is included. Here, the symbol e stands for the electron charge, whereas r or $\hat{r}$ stands for the radial distance to the electron or the position operator. Replacing the emerging cross

product between $\hat{r}$ and the momentum operator $\hat{p}$ with the angular momentum operator $\hat{l}$ leads to the final form (2.41) [43].

The elastic low-energy scattering process at crystalline solids, where the total scattering potential consist of the effective Coulomb potential and an additional contribution originating from the spin-orbit interaction, is called spin-polarized low-energy electron diffraction (SPLEED). The elastic high-energy scattering at polycrystalline or amorphous targets is called Mott scattering.

In the kinematic approximation these processes are described as single-scattering events, which is comparable to the single atom scattering. During the flight of an electron in the electrostatic field of a charged scattering center, i.e, an atomic nucleus, the magnetic moment $\vec{\mu_s}$ of the electron interacts with its orbital angular momentum $\vec{l}$ caused by the deflection. The velocity $\vec{v}$ of the electron and the electric field $\vec{E}$ of the nucleus generate a magnetic field $\vec{B} = \vec{E} \times \frac{\vec{v}}{c}$ in the rest frame of the electron which then acts upon the magnetic moment of the electron. The spin-orbit interaction corresponds to an additional scattering potential which, depending on the interplay of the spin and the orbital angular momentum, can be either of repulsive or attractive nature (see figure 2.11). The resulting difference in the direction of the scattered electrons is often referred to left-right asymmetry and causes the cross sections for opposite spin orientations to be unequal [43, p. 50]. What has been illustrated with electrons passing the scattering center on both sides in figure 2.11 can be transferred to the back-scattering from a surface.

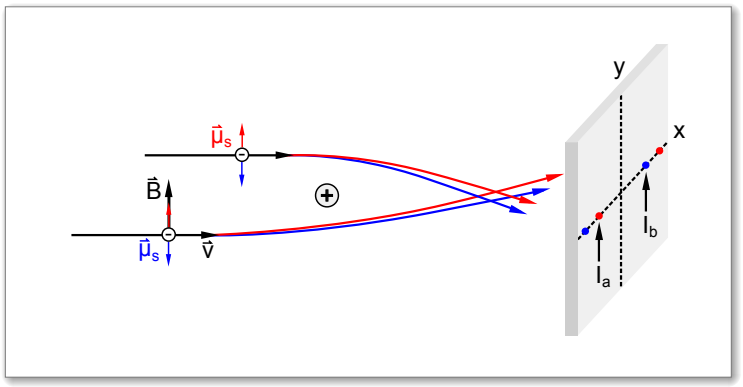

Figure 2.11: Deflection of electrons by a positively charged scattering center. The electron trajectories differ for opposite spin orientations (red and blue). The spin-orbit interaction causes a left-right intensity asymmetry (I_a, I_b). This effect can be used to polarize or analyze the electron beams.

As a consequence of the unequal spin-dependent cross sections $\sigma_\uparrow$ and $\sigma_\downarrow$, an unpolarized electron beam will become polarized with magnitude $\vec{P'} = S(\theta)\hat{\mathbf{n}}$ perpendicular to the scattering plane (only for $\theta \neq 0°$). Here, $\hat{\mathbf{n}}$ is the unit vector normal to the scattering plane. The asymmetry of the corresponding cross sections is directly proportional to the

number of scattered electrons and thus the polarization, which is given by [43, p. 42, 52]:

$$\vec{P}' = S(\theta)\hat{\mathbf{n}} = \frac{N_\uparrow - N_\downarrow}{N_\uparrow + N_\downarrow}\hat{\mathbf{n}} = \frac{\sigma_\uparrow - \sigma_\downarrow}{\sigma_\uparrow + \sigma_\downarrow}\hat{\mathbf{n}}. \tag{2.42}$$

$N_\uparrow$, $N_\downarrow$ are the number of measured spin-up and spin-down electrons and $\sigma_\uparrow$, $\sigma_\downarrow$ the corresponding cross sections. In this consideration, the process is independent of any polarization component parallel to the scattering plane. In analogy to an unpolarized beam, a beam that is polarized normal to the scattering plane will change its polarization after scattering under an angle $\theta > 0°$. Only a polarized beam with $P_n = 1$ retains its polarization. However, the direction and magnitude of $\vec{P}$ is generally changed when scattering an arbitrarily polarized beam [43, p. 38, 44]. The beam has then a polarization $\vec{P}'$ after scattering, which is given by [43, p. 43]:

$$\begin{aligned} \vec{P}' &= \frac{(P_n + S(\theta))\hat{\mathbf{n}} + T(\theta)\vec{P}_\parallel + U(\theta)(\hat{\mathbf{n}} \times \vec{P}_\parallel)}{1 + P_n S(\theta)} \\ &= \frac{(\vec{P} \cdot \hat{\mathbf{n}} + S(\theta))\hat{\mathbf{n}} + T(\theta)\hat{\mathbf{n}} \times (\vec{P} \times \hat{\mathbf{n}}) + U(\theta)(\hat{\mathbf{n}} \times \vec{P})}{1 + \vec{P} \cdot \hat{\mathbf{n}} S(\theta)}. \end{aligned} \tag{2.43}$$

The orientation of the polarization components in space can be seen in figure 2.12. The normal component P_n is changed by the Sherman function $S(\theta)$, the parallel component $P_\parallel$ is reduced by $T(\theta) \in [0, 1]$, the vector $\vec{P}$ is rotated, $P_\perp$ arises with $U(\theta)$ and all components are divided by the denominator [43, p. 43-44]. Again, an exception is a totally polarized beam, whose absolute polarization does not change ($|\vec{P}| = |\vec{P}'|$). What may change, though, is the direction. Only a polarized beam with $P_\perp = P_\parallel = 0$ and $P_n \neq 0$ retains its direction but changes its magnitude if $P_n > 0$ according to [43, p. 44-45]:

$$\vec{P}' = \frac{(P_n + S(\theta)) \cdot \hat{\mathbf{n}}}{(1 + P_n S(\theta))}. \tag{2.44}$$

In conclusion, the left-right asymmetry of a beam polarized normal to the scattering plane is given by [43, p. 56-57]):

$$A = \frac{N_l - N_r}{N_l + N_r} = \frac{(1 + PS(\theta)) - (1 - PS(\theta))}{(1 + PS(\theta)) + (1 - PS(\theta))} = PS(\theta). \tag{2.45}$$

This underlines the equality of polarizing and analyzing power since a beam with polarization $P_n = 1$ leads to $A = S(\theta)$ and an unpolarized beam leads to $P = S(\theta)$, thus $P = A$.

2.6.4 Rotational Diagrams and Mapping

Generally, the earlier introduced kinematic approximation is insufficient to describe all effects and multi-scattering processes have to be considered to fully describe spin-dependent scattering processes in SPLEED. This means multiple scattering at different atomic sites

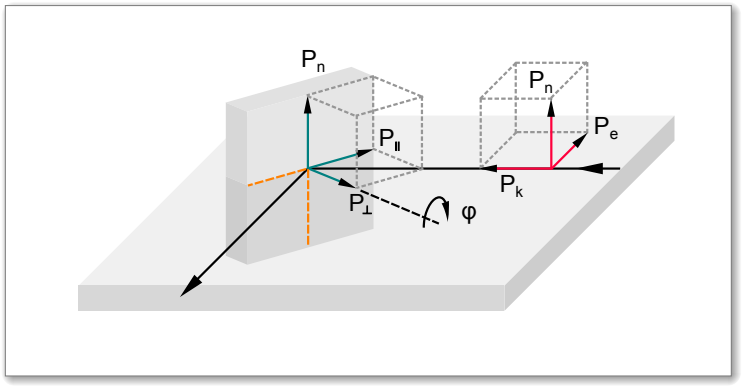

Figure 2.12: An electron beam is scattered at a target with 2 mirror planes (dashed orange line; 4-fold symmetry as found in Ir(001)). The target can be rotated by φ about its surface normal. The beam polarization can be decomposed into the components P_e, P_k and P_n (red) with respect to the scattering plane or into $P_\perp$, $P_\parallel$ and P_n (green) with respect to the target surface. For illustration purpose, the vector lengths are chosen arbitrarily and independent of each other. They should not reflect outcomes of a real experiment.

and crystal layers. The simplistic figure 2.11 is therefore no longer valid. Unfortunately, the complexity of SPLEED prohibits a more detailed and demonstrative graphical explanation. In general, the spin-dependent interactions in SPLEED will become more complex and highly dependent on the azimuthal angle [45, p. 20, 69-70]. The azimuthal dependence of polarizing or analyzing power, can be plotted in rotational diagrams.
In the context of multi-scattering processes, time reversal and spatial symmetries as fundamental physical laws have to be considered, as they induce interesting phenomena. In an experiment, the time-reversal symmetry equals the exchange of electron source and detector or an azimuthal crystal rotation of 180°. The intensity curve in a rotation diagram of a crystal with n-fold symmetry should thus have a periodicity of $2n$ (for odd n) or n (for even n). However, due to spin dependent processes the degeneracy is partly lifted and the periodicity is always n [45, p. 24-25].
Regarding spatial symmetries, the parity ($(x, y, z)^T \rightarrow (-x, -y, -z)^T$) should be conserved in electromagnetism. A mirror experiment ($(x, y, z)^T \rightarrow (x, y, -z)^T$) must therefore have the same final and initial states as the real experiment (unless the target is chiral). Longitudinal polarization components lying in the scattering plane or showing into the direction of the incident or scattered beam ($P_{\vec{k}}$ or $P_{\vec{k'}}$) transform like axial vectors [45, p. 3]. They would violate parity and can therefore not exist [43, p. 53]. Only components perpendicular to the scattering plane may exist. However, if the target or the interaction itself violates parity, polarization components in the scattering plane may arise when scattering an unpolarized beam under the influence of spin-orbit interaction [45, p. 25, 70] [43, p. 58-62]. This happens exactly when the scattering plane does not coincidence with the

mirror plane of the target. Scattering a polarized beam will influence all polarization components as already seen in equation (2.43).
Parity is again conserved when the scattering plane is simultaneously a mirror plane of the crystal. Then, the polarization components parallel to the scattering plane must vanish to fulfill the invariance under mirror operation [45, p. 25-26.] A rotation diagram of a 3-fold symmetric crystal is shown in figure 2.13 where the components parallel to the scattering plane vanish exactly when the mirror plane coincides with the scattering plane. For P_k and P_e, the rotation diagrams behave asymmetrically around these points, while the normal component P_n is mirror symmetric. Further rotation diagrams were published by [46], [6, 8, 75, 90, 99, 100] and [45, p. 81] for example.

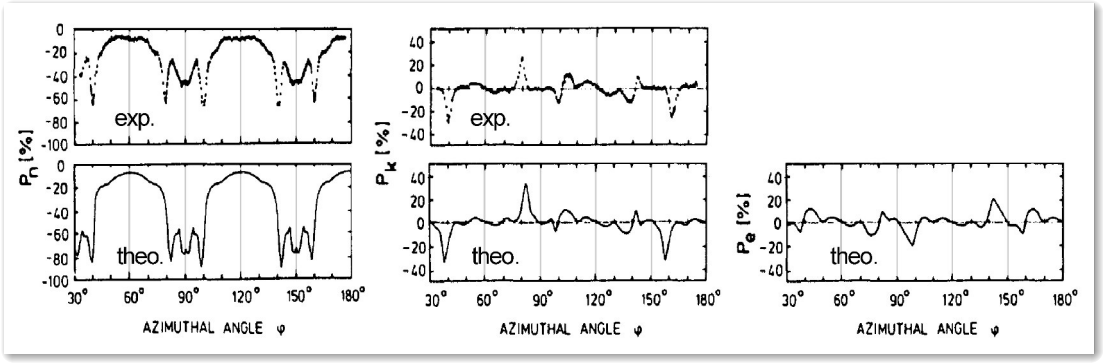

Figure 2.13: Rotation diagrams showing the polarization components of the specularly scattered unpolarized beam at a 3-fold symmetric Pt(111) target ($\theta = 43.5°$, $E_{kin} = 60$ eV) (top row) and the corresponding calculations for $\theta = 44.0°$ (bottom row). The orientation of P_n, P_e, and P_k can be seen in figure 2.12. P_n (Mott-component) shows a symmetric behaviour around 60° and 120°, while P_e (second in-plane component), and P_k (longitudinal component) are antisymmetric with respect to these angles. As expected from parity conservation, the polarization vanishes in the mirror planes. A 6-fold symmetry is not observed due to the lifting of degeneracy (taken and modified from [7]).

Besides rotation diagrams, maps (and line scans) showing the influence of E_{kin} and θ on the reflectivity, asymmetry (or Sherman function) and figure of merit (see subsection 2.6.5) can be measured or calculated to locate suitable scattering conditions for polarization measurements. Theoretical maps are generally calculated by using various methods in the framework of density functional theory. Experimental examples can be found in references [11, 91] (Fe(001) and Fe(001)-(1x1)O), [48] (Au on Ir(001)), [56] (Ir(001) see figure 2.14) and [55] (W(001)). The oxygen passivated iron and the pseudomorphic monolayer Au on Ir(001) have the advantage of a high lifetime of several months [89, 98]. While other crystals need to be regularly cleaned, these targets remain clean and do hardly suffer from residual gas contamination. A brief overview of this topic is found in [25].

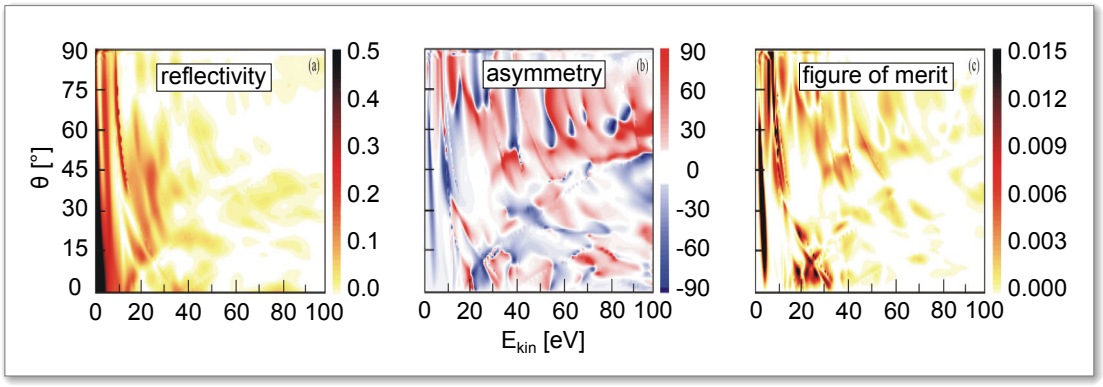

Figure 2.14: Theoretical reflectivity, asymmetry and figure of merit maps for unreconstructed Ir(001) calculated by the relativistic layer-KKR method (taken and modified from [56]). Features with bulk and surface character are visible as rapidly or slowly increasing curves. Suitable scattering conditions are given around $\theta = 45°$ and $E_{kin} = 10$ eV or 39 eV, for example.

2.6.5 Figure of Merit

The figure of merit (FoM; see equation (2.46)) is a unitless performance measure for electron spin detectors. It was originally developed for single channel spin detectors and is composed of the Sherman function S and the reflectivity $\frac{I}{I_0}$:

$$FoM = S^2 \frac{I}{I_0}. \tag{2.46}$$

The FoM can be used as an indicator for the potential measurement speed because a higher reflectivity or Sherman function improves the signal to noise ratio. A perfect single-channel spin polarization measurement device would yield a FoM value of 1. Unfortunately, the efficiency of common spin detectors based on exchange scattering (in combination with VLEED) or spin-orbit coupling (e.g. Mott-detector or SPLEED) is very low. Typical values range from 10^{-4} to 10^{-2}.

For UV-sensitive organic materials or rapidly contaminated materials that require clean surface conditions, a fast spin-polarized photoemission spectroscopy is indispensable. The parallelization of the spin measurement solves this issue by enhancing the effective figure of merit by the number N of simultaneously measured beams. In terms of photoemission spectroscopy, this means analyzing a complete energy- and angle-resolved image (two-dimensional set of electron beams) with a spin filter. This enhances the figure of merit by the number of resolved pixels. The overall data acquisition time can be drastically reduced. Such multichannel-spin-polarimeters were recently developed (e.g. $N = 10^3$ [51], $N = 5 \cdot 10^3$ [95], $N = 6.8 \cdot 10^3$ [39]). They can overcome the single-channel FoM limit of 1. Several achieved figure of merit values are shown in figure 2.15.

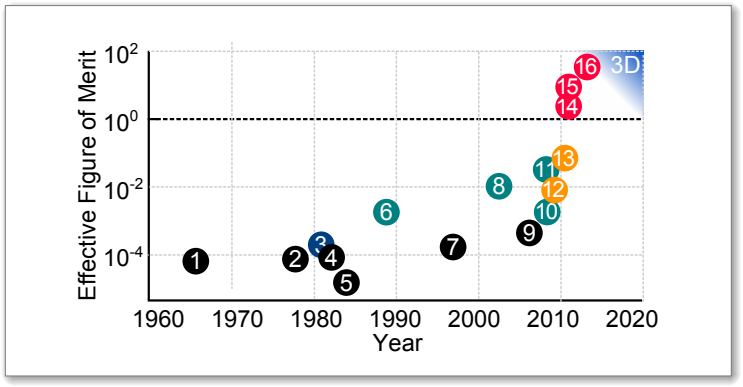

Figure 2.15: Published figure of merit values. Mott scattering (black), SPLEED (blue), exchange scattering (green), 1D time of flight (yellow) and imaging spin filters (red) were used (taken and modified from [89]). The dashed line denotes the limit of an ideal single channel spin detector. Recent multichannel developments overcome this limit. The currently attainable two-dimensional imaging spin filter values are marked in red. The 3D detection (e.g. time of flight momentum microscope) can even lead to higher values. 1-16 correspond to [14, 31, 33, 35, 41, 47, 50, 51, 67, 70, 71, 92, 94, 95, 97, 104].

2.6.6 Experimental Setup

Starting from the experimental setup described in section 2.5.5, the spectrometer can be extended to obtain multichannel spin-filtered data. One possibility is to use the imaging spin filter technique based on SPLEED. The energy- and angle-resolved image at the exit plane of the hemispherical analyzer is therefore transferred to the scattering target and subsequently measured (see figure 2.16). Established targets with high atomic number and strong spin-orbit coupling are tungsten(001) ($Z = 74$), iridium(001) ($Z = 77$) or iridium(001) with a pseudomorphic monolayer of gold ($Z = 79$). The filtering characteristics and thus their best scattering conditions are highly unequal. The measured asymmetry between images of opposite sample magnetization reveals the initial spin polarization according to figure 2.10 and 2.16. The scattering angle is usually predetermined and fixed. The fact that the filtering sensitivity is highly dependent on the scattering energy E_{kin} and the scattering angle θ is a challenge for the multichannel setup. The scattering energy as well as the scattering angle is not uniform at the exit plane of the hemispherical analyzer. The adjustable energy window ranges usually up to several eV and the angular distribution at every resolved data point is up to a few degrees. The Sherman function will therefore vary within the measured image. Changing the operation mode of the lens, i.e., the maximum acceptance angle of the electron optics will influence the angular distribution slightly. Nevertheless, a certain energy and angle distribution will inevitably arrive at the spin filter crystal (see figure 2.17). Thus, scattering with overall constant energies and merely parallel electron trajectories becomes impossible. As a consequence, either the

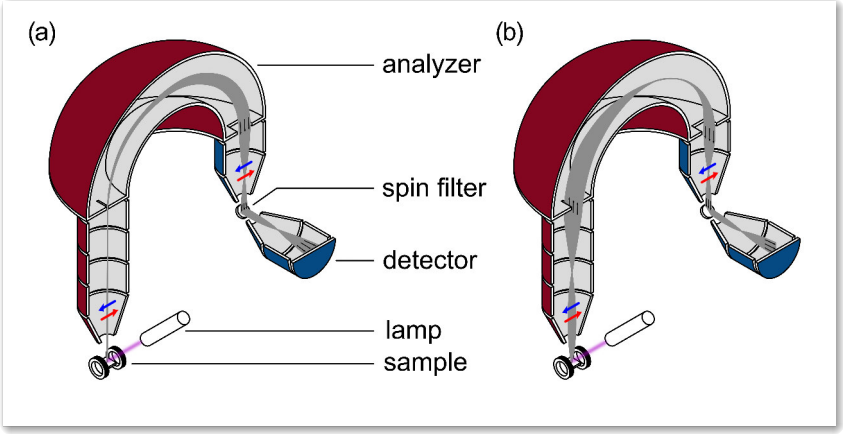

Figure 2.16: Cross sections of a multichannel spin-, angle- and energy-resolved photoemission experiment. Electron optical lenses, the hemispherical energy analyzer (red) and spin filter optics (blue) with the scattering crystal and $\theta = 45°$ are depicted. (a) Relevant trajectories are shown for the energy dispersive axis and (b) for the angle-dispersive axis. The sample magnetized by two coils and the polarized electrons are excited by a VUV lamp. Electron optics transfer the electrons to the hemispherical analyzer. The electron spin is depicted by red and blue arrows. The image at the exit plane is refocused onto the imaging spin filter crystal and finally to the delay line detector (DLD). The spin filter crystal causes an intensity asymmetry upon reversed sample magnetization because of the spin-orbit interaction.

scattered energy range and angular distribution must be small or the figure of merit of the spin filter crystal must be relatively stable and high over a certain range of E_{kin} and θ. There are basically two operating modes of the spin filter electron optics (see figure 2.17). The image of the exit plane can be refocused (and demagnified) onto the target where the electrons create a real image (a). The scattered image is then refocused (and remagnified) onto the detector. Another possibility is given by focussing a reciprocal image on the spin filter crystal. Then the lateral image formation is encoded in the scattering angle. Finally the ream image is refocused onto the detector (see figure 2.17 (b)). The first mode usually results in a better image quality especially when the surface of the scattering target is imperfect (e.g. due to contamination). This can be compared to a projection of an image onto a hazy mirror. Although the reflection might be of poor quality, the projected image is still visible when looking on the mirror itself. A disadvantage of this mode is the potential visibility of the scattering target structures (mosaicity, defects). Large scattering crystals tend to have multiple domains with slightly anomalous crystallographic orientation. This fact will be visible by little intensity and asymmetry differences in the image. The second mode produces images with lower resolution by trend but suppresses the visibility of scattering target domains. In both modes, the energy or angular distribution will

cause an averaging effect of the measured spin sensitivity in comparison with calculations. Parallel and monoenergetic trajectories are practically impossible.

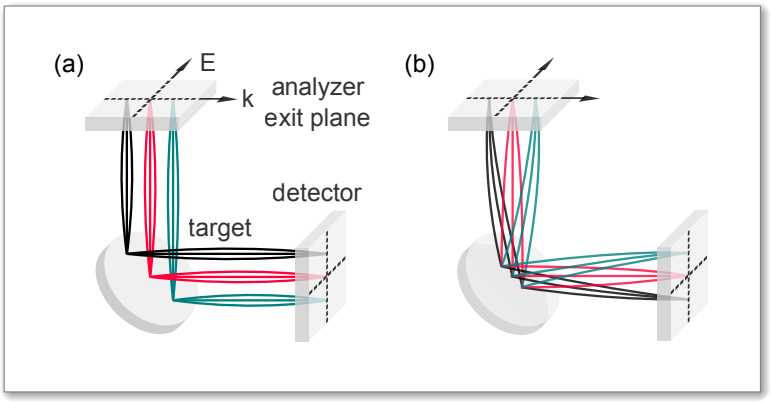

Figure 2.17: (a) Schematic drawing showing the refocusing of the analyzer's exit plane (E,k)-image onto the circular scattering target and the detector. For illustration, possible electron trajectory crossovers are omitted and the focal plane is placed on the inclined scattering target surface. (b) The analyzers exit plane image is scattered converted into a reciprocal image on the target and then refocused as real image onto the detector.

At a typical pressure of $1 \cdot 10^{-10}$ mbar, it takes approximately 4 hours to accumulate 1 Langmuir of an adsorbate on a crystal surface with a sticking coefficient of 1. Depending on this coefficient, the scattering crystal must be regularly cleaned from surface contamination to achieve high asymmetry values. Passivated and gold covered surfaces have a longer lifetime.
Inelastic scattering processes can hamper the spin-resolved photoemission spectroscopy, so that inelastic electrons should be suppressed. Phonons do slightly influence the energy of scattered electrons through phonon or magnon scattering processes. For hot crystals, the asymmetry through spin-flip processes is hardly reduced but changes of the momentum are observed which clearly reduce the intensity of the specular beam (see [25], [45, p. 19]). Therefore, the crystal should cool down to prevent offsets in the asymmetry determination. Further intensity and asymmetry variations by spin-wave excitations (below $\approx$ 10 eV), Stoner excitations (>25 eV), electron-hole excitations (<50 eV) or plasmons (>50 eV) may occur during scattering of polarized electrons at parallel magnetized targets [102] [25].

3 Experiment

3.1 Experimental Chamber

The experimental setup is shown in figure 3.1. It consists of a main chamber, a spin filter chamber and a preparation chamber. The multichannel spin-, energy- and angle-resolving photoemission spectrometer is based on a commercial SPECS PHOIBOS 150 hemispherical analyzer equipped with the multi-element, two-stage transfer lens [84]. It is embedded in a μ-metal main chamber where the W(110) sample is mounted on a xyz-manipulator. Either the $\overline{\Gamma\mathrm{N}}/[1\bar{1}0]$ or the $\overline{\Gamma\mathrm{H}}/[001]$ axis are aligned along the angular dispersive direction. A continuous flow cooling system is connected to the sample holder. Magnetic materials are avoided near the manipulator. The sample can be set to any bias voltage and rotated around the long axis of the manipulator to map the momentum space which is not covered by the angular acceptance of the spectrometer. An attached filament located underneath the sample is used for annealing and flashing through electron bombardement. For the sample preparation, a leak valve dedicated for oxygen is installed.

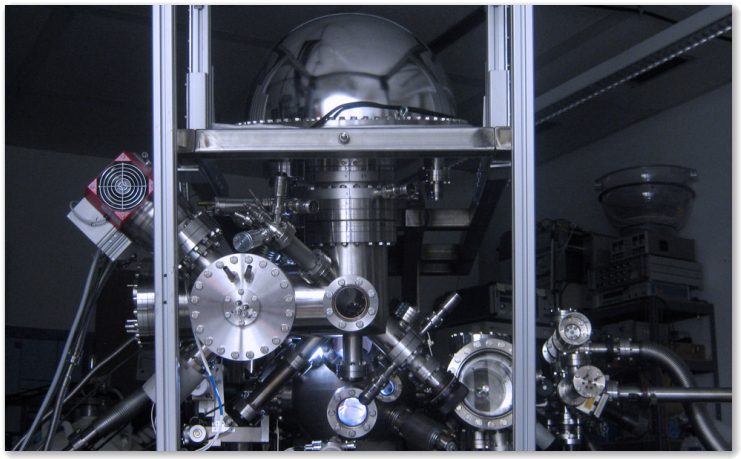

Figure 3.1: Photo of the final experimental setup. The hemispherical analyzer is visible at the top border. The L-shaped spin filter chamber is in the center and the main chamber is visible at the lower border. The preparation chamber is in the lower right corner.

An electron bombardement type water-cooled evaporator with a Fe rod of 99.995% purity enables the vapor deposition of iron onto the sample. A Knudsen cell with H_2TPP is available to create molecular films by sublimation. A water-cooled quartz crystal microbalance inside the preparation chamber is used to monitor or calibrate the evaporation. Furthermore, two coils in serial connection or one single coil can be slewed towards Fe/W(110)

samples to magnetize the films in the $[1\bar{1}0]$ or [001] direction by current pulses. The easy magnetization axis can be controlled by the film thickness. It is usually along $[1\bar{1}0]$ for thin films and changes to [001] thicknesses over 30 monolayers. Photoemitted electrons from these films will have spins aligned parallel to the magnetization axis. The magnetic properties of the Fe/W(110) sample can be analyzed by the longitudinal and transversal magneto-optic Kerr effect. A polarized 670 nm laser is therefore injected through the axial viewport of the analyzer and reflected at the Fe/W(110) sample. For the angular calibration and resolution determination, a slit array (d = 0.2 mm with 1 mm interval) can be moved in front of the transfer optics. The hemispherical analyzer has an additional built-in slit array at the exit plane generating equidistant lines in the energy dispersive direction (d = 0.3 mm with 8 mm interval). An electron gun (max. 5 kV) and a differentially pumped He-VUV discharge lamp (21.2 eV) serve as excitation sources. The VUV lamp has a glass capillary with a small inner diameter to guide the light towards the sample and create a small spot. A sample stage and a LEED system are located in the adjacent preparation chamber.

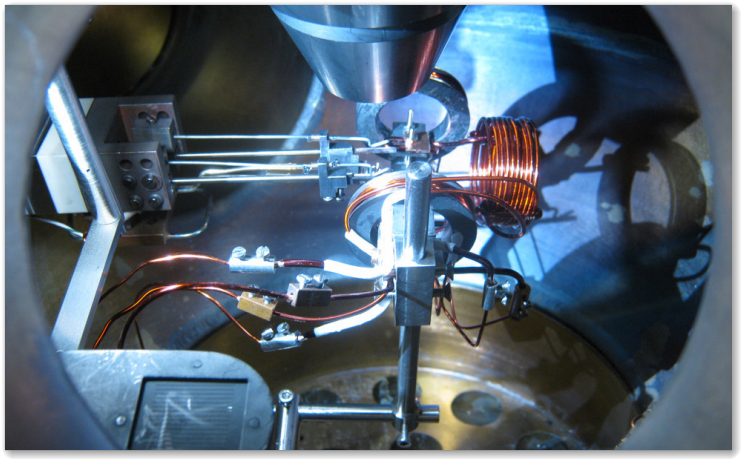

Figure 3.2: The xyz-manipulator holds the sample below the transfer lens of the photoemission spectrometer which is visible at the upper border. The movable slit array for calibration and distortion review is located in the parking position at the lower left corner.

The μ-metal L-shaped spin filter chamber with carbon coated electron optics is attached to the exit flange of the hemispherical analyzer. Moreover, a 5° inclination of the spin filter system is integrated to better match the simulated escape angles at the hemispherical analyzer exit plane. A non-μ-metal plate valve is installed in the lens system between the exit plane and the scattering crystal to separate both chambers during crystal preparations (see figure 3.5). The installed internal μ-metal shield near this valve is overlapping as far as possible but inevitably slightly permeable for magnetic fields. Inside the spin filter chamber a circular Ir(001) crystal (d = 15 mm) is destined for spin-dependent electron

scattering based on SPLEED. Here, a magnetization reversal of the Fe/W(110) sample leads to a beam polarization inversion which usually causes intensity asymmetries between the scattered images. The scattering angle θ is fixed to 45° and the iridium is mounted on a rotation feedthrough to vary the azimuthal angle Φ. A bias voltage can be applied to the Iridium and electron bombardement from installed filaments is used to prepare the crystal. For preparation purpose, a thermal oxygen doser is available. The scattered electrons are measured with a delay line detector (active area d = 40 mm) which guarantees extremely low dark count rates. A flat-field correction to eliminate mainly intensity variations due to aging effects of the microchannel plates was omitted because of the mint condition of the microchannel plates. Instead, a low-pass filter was useful to reduce periodical artifacts originating from intrinsic time-to-digital converter parasitics or microchannel plate structures.

3.2 Chamber Condition and Crystal Preparation

With inactive VUV lamp, the base pressure was usually around $3 \cdot 10^{-10}$ mbar in the main chamber and around $1 \cdot 10^{-10}$ mbar in the spin filter chamber. Our W(110) crystal was prepared by 5-10 low-power flashes to 1200 K with approximately 75 W for 10 s (60 s idle interval) in an oxygen atmosphere of $5 - 8 \cdot 10^{-8}$ mbar. After stopping the oxygen supply and returning to base pressure, a subsequent high-power flash to 2200 K was performed by applying between 150-180 W for 8-10 s. Temperatures were measured by an optical pyrometer and the tungsten surface quality was checked by LEED.
Based on a clean tungsten surface, multiple layers of iron were deposited onto the tungsten crystal. The sample surface was facing to the iron evaporator which was warmed-up before the shutter was opened. Around 15-25 monolayers of iron were usually deposited at room temperature to ensure a high spin polarization of low-energy secondary electrons [61] with values around 45% [49]. During the room temperature evaporation at rates around 25 monolayers per hour, a pressure of $5 - 10 \cdot 10^{-10}$ mbar was detected. A subsequent continuous annealing of the Fe/W(110) sample to 550-600 K with a filament and additional 3 W from electron bombardment for 10 minutes resulted usually in a smooth surface and a clear carbon- and oxygen-free LEED pattern.
The reliable magnetizability along the easy-axis was always confirmed with the magneto-optic Kerr effect. A continuous coil current of 60 A through the serial coil produced a magnetic field of over 13 mT in the center with the serial coils. The created field strength was always above the expected coercivity of less than 2 mT [61]. In most cases, the coils were supplied by a capacitor pulse creating a much stronger field, which was not determined.
The iridium crystal was prepared by 5-10 low-power flashes with 135 W for 10 s ($\geq$ 5 min idle interval) in an oxygen atmosphere of $1 \cdot 10^{-7}$ mbar. A thermocouple that is placed in a lateral mounting hole measured around 1200 K in accordance with an optical pyrometer.

After reaching base pressure and shortly before starting a measurement, a high-power flash was performed with an average power of 235 W applied for 10 s. Again, thermocouple and pyrometer reported consistent temperatures around 1600 K as needed [48,95,98]. The Iridium crystal was regularly cleaned according to its lifetime.
H_2TPP molecules (see figure 3.3) were deposited at room temperature onto the Fe/W(110) samples. In the crystalline phase, the layer-to-layer distance is 350 pm. While thin films of H_2TPP can grow ordered on metal substrates like Cu(110)-(2x1)O [83], there is no growth order on Fe(110). A precise monolayer coverage can therefore not be assigned to H_2TPP molecule films on Fe/W(110). Film thicknesses were nevertheless specified by the coverage of molecules equivalent to monolayers of the crystalline phase. A monolayer of H_2TPP induced a frequency change of 9.68 Hz for an AT-cut 10 MHz quartz crystal and 2.46 Hz for a 5 MHz AT-cut quartz crystal. The warm-up time for a stable evaporation rate was over one hour and could be shortened by dynamically adjusting the heating current. The deposition of H_2TPP on Fe/W(110) resulted in LEED images with higher a background intensity. Auger spectra usually showed a decrease of the iron peaks and an increased carbon and nitrogen peak.

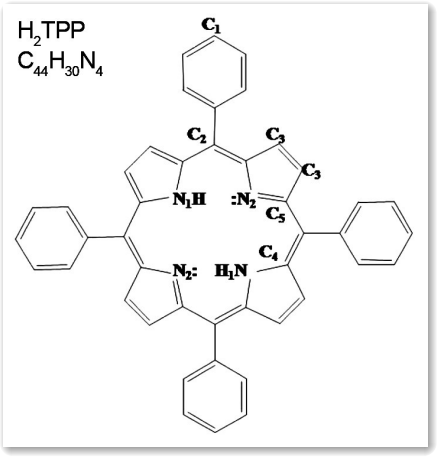

Figure 3.3: Planar representation of H_2TPP with numbered elements of different species (taken from [63]). A detailed structural description is found in [63].

3.3 Analyzer Settings

The PHOIBOS 150 analyzer from SPECS could run in different modes with α_{acc} equal to $\pm 3°$, $\pm 4°$, $\pm 7°$, $\pm 13°$ [84]. The mode with the acceptance angle of $\pm 13°$ is called wide angle mode by SPECS. Entrance slits d could be chosen from 0.2 mm, 0.50 mm, 1.0 mm, 3.0 mm and 7.0 mm. The spectrometer was always operated in the wide angle mode to transfer the maximum angle of $\pm 13°$ to the exit plane of the hemispherical analyzer.

Redundant trajectories that do not contribute to the detector image were blocked by a transfer lens iris diameter of 15-20 mm. Entrance slits were usually chosen between 0.2×20 to 3×20 mm^2 to obtain the highest possible energy resolution while retaining sufficient intensity. The pass energy E_p was usually set to 30 eV which transfers an energy window of several eV to the 20x70 mm^2 exit plane of the hemispherical analyzer. The exit plane was either open, equipped with a fine mesh or a slit array in energy dispersive direction (see figure 3.4). To compensate residual magnetic fields, the trim coil of the analyzer was properly adjusted. The kinetic energy E_{kin} was usually set to 10 eV or 39 eV. Since the scattering energy E_{scatt} equals E_{kin} for a grounded spin filter crystal, we covered the major spin filter scattering conditions. Minor variations of E_{scatt} were realized by applying spin filter crystal bias voltages of up to ±5 V. This had a slight magnification and shifting effect on the image. Varying E_{kin} without adjusting the spin filter optics was only possible within few eV and therefore rarely used.

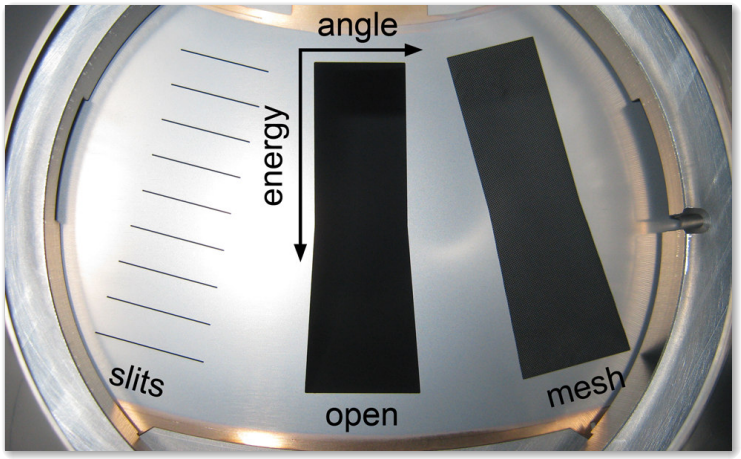

Figure 3.4: Photo of the exit plane of the hemispherical analyzer. The three possible 20 mm × 70 mm exit windows are visible.

3.4 Spin Filter Settings

The spin filter electron optics were revised regarding the setup from 2014 [57]. A rotation feedthrough allowed a variation of the azimuth. The iridium crystal plane was adjusted until a specular beam reflex did not show any excentricity or spot movement upon azimuthal rotation. Windows of the cone-shaped lenses have been enlarged to fully transmit the electron bunches. A graphite coating ensured sufficiently uniform work functions. The electron trajectories inside the improved spin filter optics had to be simulated based on models from previous versions using the software SIMION 8.1. The model had to be adapted and no information about previous voltage settings were reusable. The objective was to reproduce the real image of the exit plane at the iridium crystal and refocus it onto

the detector. Scattering a reciprocal image at the target is also possible but resulted in a lower image quality as explained in subsection 2.6.6. Ultimately, voltages of 15 lens elements were determined. The first lens element behind the exit plane of the hemispherical analyzer (lens 1 in figure 3.5) was set to the same voltage as the base plate of the analyzer ($E_p - E_{kin}$) to ensure a good coupling to the analyzer and enable simple simulations. The iridium crystal (number 13 in figure 3.5) and the adjacent lens elements were set to ground potential to ensure a homogeneous electric field distribution around the sample. Moreover, the scattering energy is then automatically defined by $E_{scatt} = E_{kin}$. Special attention was given to the fact that the iridium reflectivity or spin sensitivity depends on the scattering angle θ. This fact demands for preferably parallel beams with little angular distribution during scattering to avoid radial variations and intermixture of reflectivities and spin sensitivities. Additionally, the plate valve region (lens 7-10 in figure 3.5) with magnetic stray fields should be passed at high voltages. The final tuning of voltages and controllable deflectors of 4 lens elements (number 2, 4, 11, 15 in figure 3.5) was carried out experimentally. First, the voltages of the elements after the reflection at the iridium crystal were tuned until the border of the circular shaped iridium as well as visible Ir domains were sharp (see section 4.2 of chapter 4). Secondly, all the other elements between scattering crystal and hemispherical analyzer were tuned so that the slit arrays in front of the transfer lens and at the exit plane of the analyzer were sharp and barely distorted. These settings were approved by a high asymmetry of spin-polarized low-energy electrons from Fe/W(110). The results of the simulations and the experimentally applied voltages are shown in section 4.1 of chapter 4.

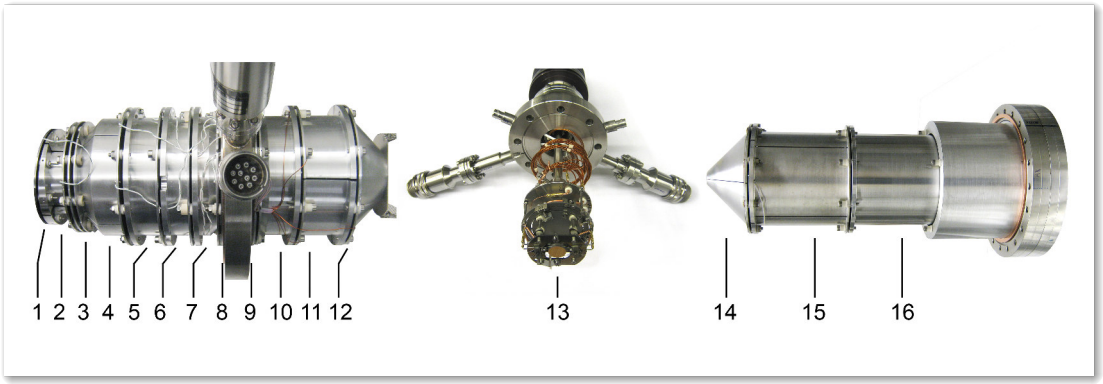

Figure 3.5: Photo of electron optics and the iridium scattering crystal mount. Lens elements 1-12 transfer the image from the exit plane to the Ir crystal. The valve is located between 8 and 9. The Ir crystal (13) is mounted on a rotation feedthrough. Lens elements 14-16 transfer the scattered image to the DLD.

3.5 Sample Position, Spin Orientation and Excitation Sources

The lateral sample position and optimum transfer lens distance of 40 mm were verified to an accuracy of 1 mm by ex-situ laser displacement measurements. This could not be done prior to evacuation since the transfer lens moved slightly towards the sample in vacuum conditions. The angle was optically determined by guiding a laser though the lens axis viewport and regulated with a precision of at least $\pm 0.25°$. By default, the sample surface was tilted 5° around the manipulator axis and thus inclined to the normal plane of the lens axis. Depending on the easy axis of the sample, photoemitted electrons from magnetized Fe/W(110) samples had therefore spins aligned normal to the scattering plane (out-of-plane) or parallel to the scattering plane (in-plane) at the iridium crystal. The lateral position of the sample was checked optically by looking through the axial viewport and by using the low magnification mode of the spectrometer. It allows a spatial imaging along one spectrometer axis. The sample can then be moved through the field of view. Characteristic points of the sample holder will become visible as intensity differences. A nicely focused electron gun was used to produce figure 3.6 by a stack of several images. The center of the sample can then be easily determined. However, the optimum position for the angular modes might differ slightly.

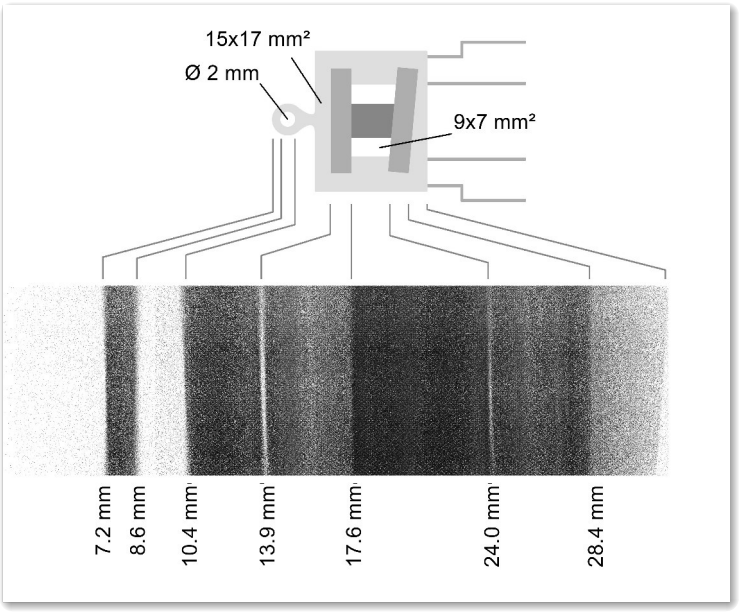

Figure 3.6: Combined detector images of a tungsten sample on an omicron molybdenum sample holder recorded in the low magnification dispersion mode. Dark areas represent high intensities.

The He-VUV lamp was driven at 0.5-0.7 kV and 0.15 A. The angle of incidence was 45°. During ignition, the pressure of the Helium with purity 6.0 reached the 10^{-6} mbar region in the main chamber. During operation it was in the 10^{-7} mbar region in the main cham-

ber and approximately on order of magnitude better in the spin filter chamber. The ion pump was switched off. Tests with a CaF sealed capillary and Argon gas (11.6 eV and 11.8 eV) were successful and no gas leaked into the main chamber. Unfortunately the intensity loss was too high because the window transmissivity is fairly low at 11.6 or 11.8 eV. The doublet was also relatively pronounced and undesired. In another test a LiF lens was attached leak-proof to the capillary. The lens distance to the sample matched the focal length to focus VUV light from hydrogen gas discharge onto the sample. The intensity was higher but a nicely focused spot could not be observed in the spatially resolved modes of the spectrometer.
The energy of the electron gun was set to 1.5 kV to yield a high secondary electron intensity and polarization in combination with the Fe/W(110) sample [49]. Deflector and focus settings were always adjusted regarding image quality, intensity and asymmetry. The correct deflector settings were extremely important to obtain high asymmetries. An off-enter spot position will entail unfavorable angular distributions at the exit plane and finally change the conditions at the scattering crystal.
Both excitation sources were always warmed-up until the intensities were sufficiently stable. The excitation spots were positioned by evaluating intensity and distortion in images. The spatially resolved mode of the spectrometer in combination with the transfer lens aperture additionally helped to align the spots [86]. The diameters were at least < 0.4 mm for the electron gun and a few millimeters for the VUV lamp. The VUV lamp spot was adjusted easiest using a laser beam guided trough the capillary onto the sample.
Generally, spin-polarized secondary electrons from 15-25 monolayers Fe/W(110) with energies around 0.5-3.0 eV were used to calibrate and characterize the setup. The measured spin polarization from Fe/W(110) samples decreased noticeable over a couple of weeks due to surface contamination but was still sufficient for further calibration measurements.

3.6 SARPES Evaluation Program

For many evaluation tasks, small programs have been written to process and visualize the data. To process the experimental data produced by the SPECS CCD Acquire software, a program was written in Python (see figure 3.7). It is able to read the saved bitmap images, ASCII files and settings, display them in a file browser and edit and visualize them in different ways. Besides the standard ARPES image, the SARPES image can be calculated out of two images. Line scans of ARPES and SARPES spectra can be plotted along any constant energy or angle position. Additionally, all measuring properties can be displayed. Some of the main editing possibilities cover diagram properties, field of view variations, energy- and angle-calibration, background correction and threshold setting, Gaussian blur, binning, low-pass correction, total variation denoising, k-space conversion, data and image rotation and shear. The result can be exported as vector, ASCII or image files. In the SARPES image, a customizable local asymmetry analysis is integrated.

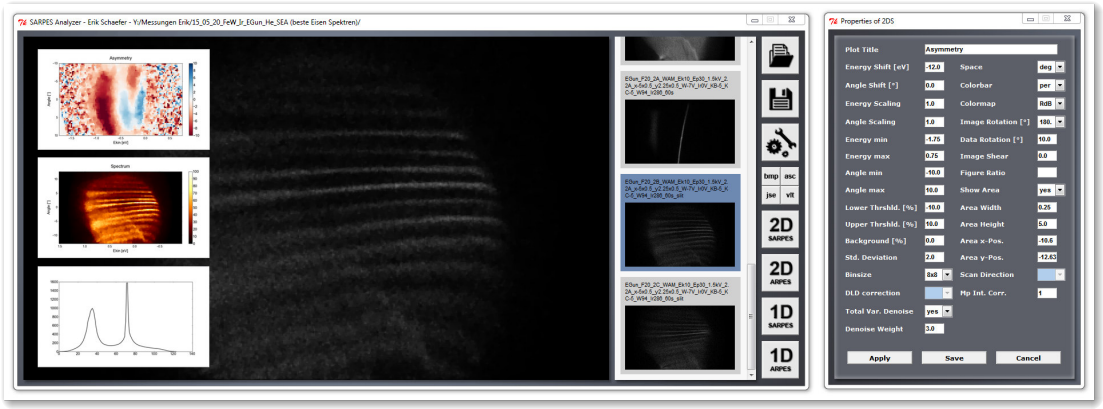

Figure 3.7: Screenshot of the written software for the comfortable data analysis. The small inlets show different display variants. The right window shows the editing options.

3.7 Efficient Spin Resolved Spectroscopy Observation Machine at Hiroshima

A photoemission spectrometer with a double VLEED spin detector was used at the Hiroshima Synchrotron Radiation Center. A detailed description of the experimental setup is found in references [65, 66]. Three different W(110) crystals have been used in total for the measurements. An iron evaporator of the same type as used in the multichannel SARPES experiment was provided and calibrated with a cooled quartz micro balance. The H_2TPP evaporator was dismounted from the multichannel SARPES experiment, brought to the HSRC and attached to the ESPRESSO machine. A new calibration was carried out. Again, a long warm-up of over one hour was needed to achieve relatively stable deposition rates. The rate was checked shortly before moving the sample into position and shortly after the deposition. It was usually in the range of 1-3 $\frac{ML}{h}$. The heating power of the crucible was 3.0-3.5 W. The pressure was constantly around $1 \cdot 10^{-9}$ mbar during evaporation. It is assumed that the temperature of the crucible was <300°. The base pressure inside the preparation chamber was around $4 \cdot 10^{-10}$ mbar. In the spectroscopy chamber, it was in the high 10^{-10} mbar range without He-gas. Crystal preparation procedures to nominal temperatures were done as described before. Only the heating power was different depending in the crystal. The surface quality of produced samples was analyzed by LEED and Auger spectroscopy.

4 Results

4.1 Trajectory Simulations and Detector Image

Electron trajectories were simulated for scattering energies of 10 eV and 39 eV in the real image scattering mode and for 10 eV in the reciprocal image scattering mode. Important imaging requirements as described in section 3.4 were respected while searching for suitable lens voltages. Exemplary secondary electron spectra of each setup were recorded to assess the image quality. The exit window of the analyzer was therefore usually meshed since recorded images with the open exit window (see figure 3.4) tended to suffer from stronger distortion originating from electrostatic fields penetrating into the hemispherical space (see 4.1). A more detailed analysis of the detector image is given in section 4.2 and 4.3.

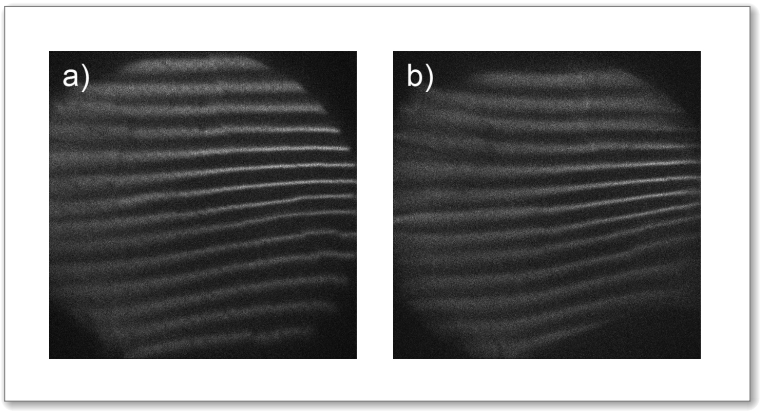

Figure 4.1: Angular slit array recorded after the scattering at the spin filter for calibration purpose. Image (a) was recorded with a meshed exit slit and (b) with an open exit slit.

The constructed model for simulating the electron path starts at the exit plane of the hemispherical analyzer and ends at the delay line detector. For technical reasons, the scattering angle of 45° and the crystal itself were omitted in the simulation. The first electrode was always set to a voltage of $E_p - E_{kin}$ and the iridium crystal as well as the neighboring electrodes were set to ground potential for reasons stated in section 3.4. Each exemplarily plotted electron bundle consists of three electron trajectories with initial angles of -1, 0 and +1 degree at their point of origin. Their initial kinetic energy behind the first electrode was set to E_p. A linear energy distribution around E_p as found in the experiment was omitted. The displacement from the optical axis of the two outer bundles was set to ±7 mm. Blue contours in the images show lines of equal energy to illustrate the

shape of the electric field. The angular distribution and kinetic energy of each trajectory was monitored 42 cm behind the first electrode to benchmark the scattering conditions. The experimental iridium crystal position might have been slightly different, not least because of the scattering angle that corresponds to an inclined scattering plane in the simulation. Despite this fact the obtained values at 42 cm are still very accurate since no major variations of the monitored values arise within a few centimeter in the nearly field-free region.

Figure 4.2 shows the best simulation found for the real image scattering mode with a scattering energy of 10 eV (see figure 2.14). The corresponding lens voltages can be found in table 4.1. The first focal plane is located 42 cm behind the first electrode and is naturally slightly curved. However, the experimental focal plane position will be different due to the angular and energy distribution at the exit window of the analyzer. There is no image magnification from the exit plane to the scattering crystal and the displacement of the outer bundles from the optical axis is still ± 7 mm. As consequence, only an elliptic part of the 20 mm × 70 mm exit plane can be scattered at the crystal. In the energy dispersive direction, this width is approximately 15 mm and equal to the diameter of the scattering crystal. With 10.6 mm in the angular dispersive direction the transferred width that can be scattered is reduced by a factor of cos(45°). For grounded electrodes around the crystal, a demagnification of the exit plane image onto the crystal was technically impossible without violating the imaging requirements of preferably parallel trajectories with small angular dispersion. However, a magnification of 2.05 from the crystal towards the detector was realizable to benefit from the large active circular delay line detector area of 40 mm in diameter. The ±7.0 mm in the energy dispersive direction at the exit plane translate to ±14.4 mm at the detector. According to the measurement point at 42 cm marked by red dots, the scattering energy is 10.1 eV and each trajectory bundle has electrons with angles of 1.7°, 0.0° and −1.7°, 1.4°, -0.4° and -2.1° or -1.4°, 0.4° and 2.1° with respect to the optical axis. The deviation from the targeted scattering angle is accordingly twice as high.

Several deflectors with adjustments of up to 15 V were needed to shift the image onto the crystal and the detector. The deflector settings were highly dependent on the sample position, source spot position, analyzer settings and lens modes. They had to be carefully determined as incorrect values caused a significant loss of image quality. Unfortunately, the elements around the plate valve could not be raised over 165 V although this would minimize the influence of magnetic stray fields in this region. A higher voltage always resulted in a shorter focal length, which could not be compensated. The energy and angular slits are therefore slightly rotated which is a result of longitudinal field components. The angle between angular and energy slits are surprisingly not rectangular even after compensating the different axis scales. This is probably a perspective effect of the image rotation in combination with the inclined scattering crystal surface and astigmatism of the hemispherical projection.

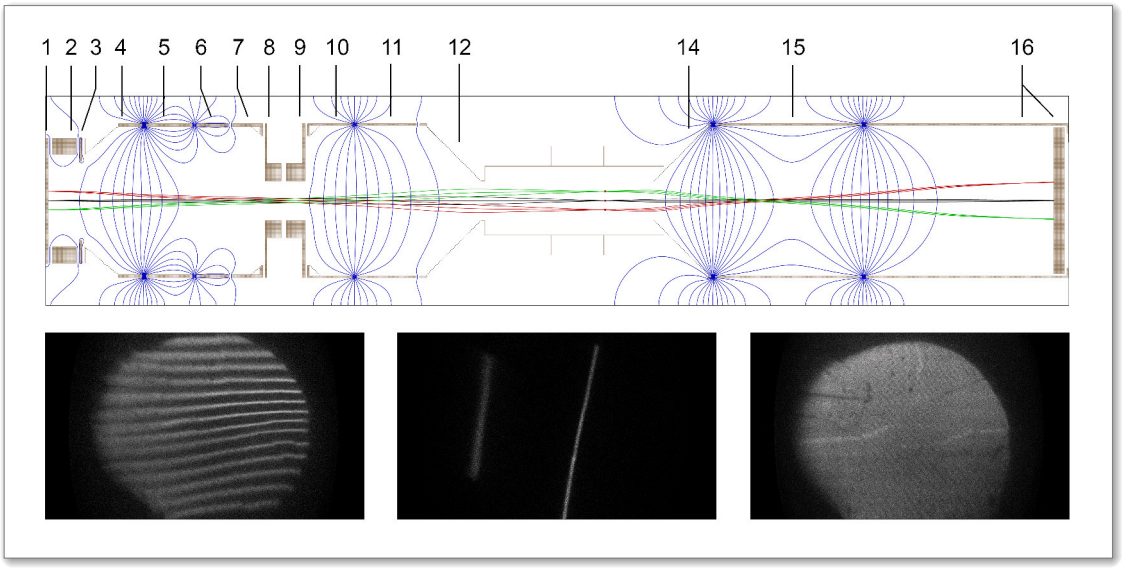

Figure 4.2: Top: Simulation according to the experimental setup of the real image scattering mode with $E_{kin} = E_{scatt} = 10$ eV and $E_p = 30$ eV. Bottom: Images of secondary electron spectra taken at $E_{kin} = E_{scatt} = 10$ eV and $E_p = 30$ eV. The E_{kin} axis is horizontal and the vertical axis represents the emission angle. The sample was set to -7 V bias to capture the low-energy secondary electrons. The angular slit array (left), the exit plane energy slits (center) or the standard exit plane mesh (right) were employed and the mirror plane of the iridium was either identical to the scattering plane or rotated by 45°.

The second scattering condition around 39 eV scattering energy (see figure 2.14) was also simulated in combination with the real image scattering mode (see figure 4.3). The voltages are shown in table 4.1. A demagnification of 0.81 from the exit plane to the focal plane around 41.5 cm is observed. This allows to transfer a window of 18.5 mm in the energy dispersive direction and 13.1 mm in the angular dispersive direction. The magnification from the crystal towards the detector is 1.76, which leads to an overall magnification of 1.42. The active detector area is therefore not ideally utilized. The scattering energy at the 42 cm measurement point is 39.2 eV. The angles of the center bundle are ±1.1° and ±0.0°. The outer bundles have angles of 2.7°, 1.5° and 0.4° or -0.4°, -1.5° and -2.7°. The trajectory bundles can be further tuned to become even more parallel.
The advantage of this scattering condition is the relatively low angular distribution during scattering. Furthermore, the high voltage of 800 V around the plate valve reduces the magnetic stray field influence significantly as recognizable by the reduced image rotation in comparison to figure 4.2. The demagnification to the scattering crystal is expressed by the larger acceptance in the energy direction. Surprisingly the angular acceptance has not increased and the resolution is lower. This might be related to the high sample bias of 35 V which changes the entrance angles into the transfer lens. Another interesting fact is

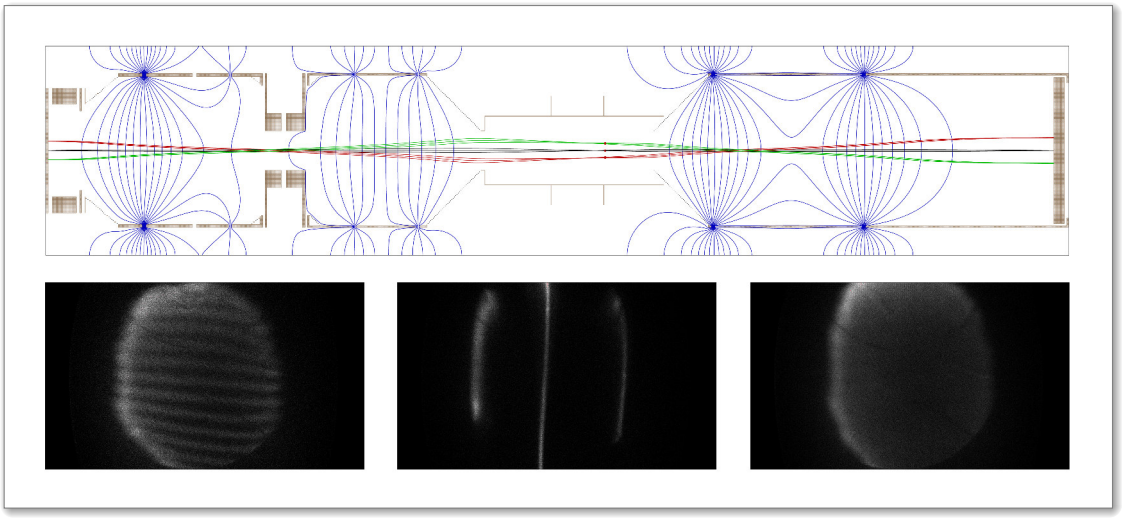

Figure 4.3: Top: Simulation according to the experimental setup of the real image scattering mode with E_{kin} = 10 eV, E_{scatt} = 39 eV and E_p = 30 eV. Bottom: Images of secondary electron spectra taken at $E_{kin} = E_{scatt} = 10$ eV and $E_p = 30$ eV showing a similar sequence of slit arrays as in figure 4.2. The sample was set to a bias voltage of -35 V. The mirror plane of the iridium was identical to the scattering plane.

the significant resolution drop for a mirror plane which is rotated by 45° with respect to the scattering plane. This might be attributed to the (5x1) superstructure of clean Ir(001), which produces additional diffraction spots lying nearby the (00) spot. The superstructure spots coincide with the scattering plane for the rotated crystal and thus contribute to the scattered intensity but do not conserve the parallel momentum. This behavior was not observed in the 10 eV scattering setup. A logical reason is missing here. Furthermore, this setup was only tested experimentally and no fine-tuning has been done to further improve the image quality.

In a final simulation, the reciprocal image scattering mode was investigated (see figure 4.4 and table 4.1). An iridium area of less than 5.2 mm is hit for the maximum initial angular distribution of ± 1°. This enables the utilization of smaller crystals if the distribution is small. Since the transferred image size is solely dependent on the angular distribution, the whole exit plane can be transferred to the detector in principle. An overall magnification of 1.38 from the exit plane to the detector is observed according to the simulation. The crossing point is at 40 cm for a scattering energy of 10.0 eV. The angular distribution of the center bundle is 0.0° and ±1.3° while the outer bundles have a distribution of 5.2°, 6.6° and 7.9° or -5.2°, -6.6° and -7.9°. This distribution is rather large. A construction change or further fine tuning can reduce these values.

The detector image in the reciprocal image scattering mode has a relatively large angular and energy acceptance but shows strong aberrations throughout the entire field of view.

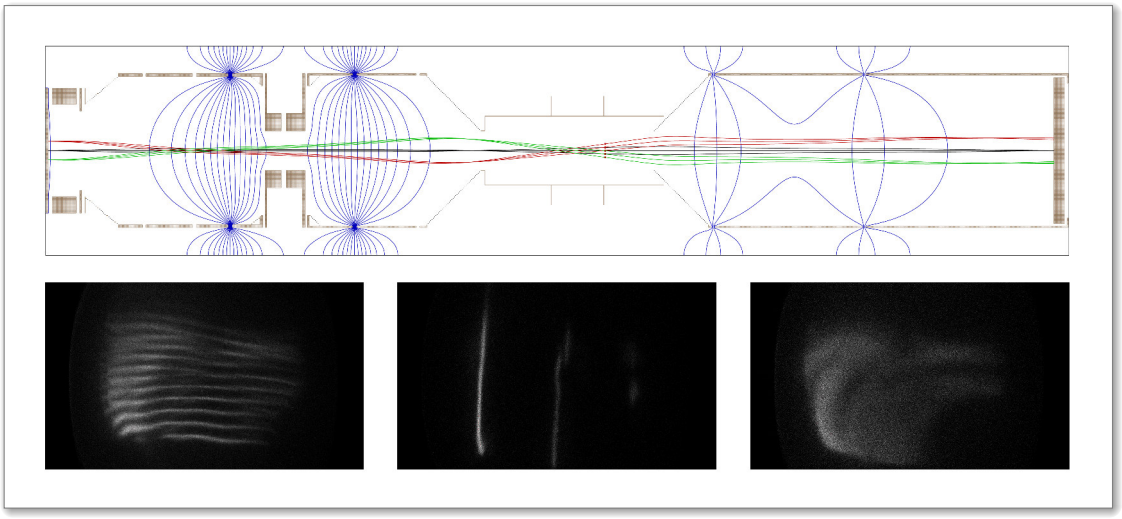

Figure 4.4: Top: Simulation according to the experimental setup of the reciprocal image scattering mode with $E_{kin} = E_{scatt} = 10$ eV and $E_p = 30$ eV. Bottom: Images of secondary electron spectra taken at $E_{kin} = E_{scatt} = 10$ eV and $E_p = 30$ eV showing a similar sequence of slit arrays as in figure 4.2. The sample was set to -7 V bias to capture the low-energy secondary electrons. The [100] direction of the iridium was rotated by 45° to the scattering plane.

The images of the slit arrays show abrupt displacements and kinks which are a result of crystallographic misorientations of the scattering crystal (see also section 4.2). The standard image also shows a non-uniform illumination which is problematic. However, further-fine tuning of voltages might reduce these problems partly.

	1	2	3	4	5	6-9	10	11	12	13	14	15	16
x: 10 eV	20	-6	30	10	250	120	165	15	0	-	0	225	10
x: 39 eV	20	-9	0	0	800	800	600	300	0	-	0	700	10
k: 10 eV	20	0	0	0	0	0	300	0	0	-	0	85	15

Table 4.1: Applied lens element voltages in simulations or experiments in the real image mode (x) or reciprocal image scattering mode (k) at different scattering energies. Number 13 represents the scattering crystal which is absent in the simulation.

After the simulations with trajectory bundles having an angular distribution of ±1°, it is important to take a closer look at the angular distribution at the exit plane of the spectrometer. Unfortunately the distribution of the angles as well as the angular spread is not constant and behaves differently. The distribution can be simulated, which was done by SPECS. For a kinetic energy of 10 eV, an excitation spot size of 0.5x0.5 mm^2 and an iris diameter of 60 mm, the elongation (angle in the energy dispersive direction) is approximately -5.5° in the center of the exit plane. This is the mentioned reason for the

5° inclination of the spin filter chamber. Towards higher and smaller energies (±20 mm away from the center), the elongation drops to -3°. The angular spread is ±0.5° for the 1x20 mm^2 entrance slit and increases to ±2.5° for the 7x20 mm^2 entrance slit. The variation of this behavior in the non-dispersive axis is negligible. The azimuth (angle in the angular dispersive direction) is naturally 0° in the center of the exit plane. For the 1x20 mm^2 entrance slit and towards higher angles (±10 mm away from the center), the azimuth equals up to 5.0° on one side (20 mm away from the image center of the energy dispersive direction) and up to -5.0° on the opposite side. The angular spread is below ±0.5°. For the 7x20 mm^2 entrance slit, the angular spread equals ±0.5°. In principle, the same behavior applies for a kinetic energy of 39 eV. Only the angular spread increases by up to 30% in the worst case.
Since the transferred field of the exit plane is only ±7.5 mm in the energy dispersive direction and ±5.3 mm in the angular direction, the elongation and azimuth values are significantly smaller. The 1x20 mm^2 entrance slit for example comes along with an elongation of -5.5° in the center and -4.5° to -5.5° at ±7.5 mm in the energy dispersive axis and has an angular spread of ±0.5°. The azimuth is 0° in the center. At ±5.3 mm in the angular dispersive direction it is approximately ±2.5° with an angular spread of ±0.5°. According to trajectory simulations with the spin filter model, a maximum deviation of $0.4^{+1.7}_{-1.8}$ degree can occur for the scattering angle (elongation) of the outer trajectories at the iridium spin filter crystal in the 10 eV real image scattering mode. In the center of the image, the elongation deviation equals $0.9^{+0.9}_{-0.9}$ degree. The azimuth can vary up to $3.8^{+1.7}_{-1.7}$ degree at the extreme border and $0.0^{+0.9}_{-0.9}$ degree in the center. These angular distributions are scattered at the crystal and cause a decrease of the measured asymmetry due to the averaging over a range of suboptimal scattering conditions. The deviations increase considerably with the size of the entrance slit. Although a decrease of the measured asymmetry towards the the field of view border is expected, it is not noticeable in the asymmetry images even with larger entrance slits of 7x20 mm^2 (see figure 4.17 and 4.18). The deviations are obviously acceptable and other factors such as kinetic energy variations or crystallographic misorientations play a bigger role at least for the asymmetry variations over the entire field of view.

4.2 Image Characteristics and Domain Microscopy

Recorded images show the circular shape of the irradiated iridium scattering crystal of 15 mm in diameter. The kinetic energy axis is horizontal and the emission angle is vertical. Small dots with anomalous intensity on the crystal may originate from dust particles or defects at the iridium surface. The elliptic crystal shape is a consequence of the stretched angular image axis. The scattering angle, which causes an elliptic image transfer, compensates this partly. An additional distortion originates from the internal delay line detector settings and the transfer lens. The lens distortion is generally smaller for higher kinetic

energies (see figure 4.5). Although a dewarping routine is available in the SPECS software, it is difficult to do the same with the spin filter system which adds additional aberrations.

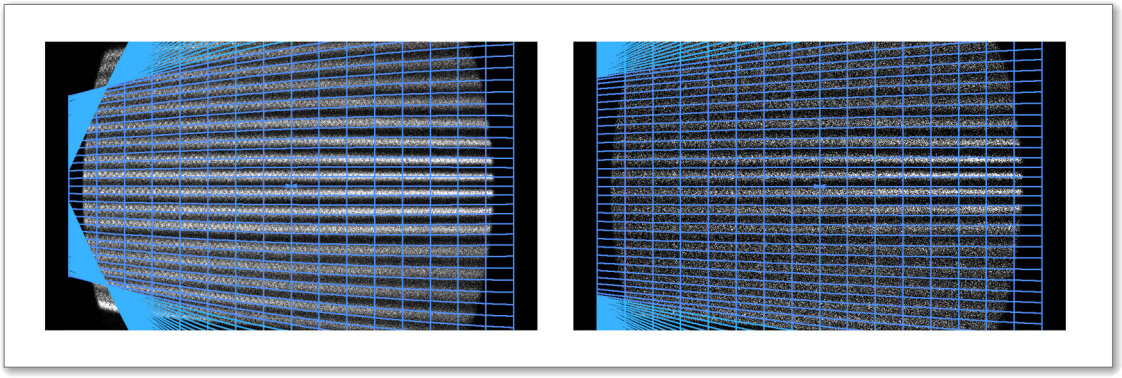

Figure 4.5: Image of the angular slit array recorded with the bare spectrometer without attached spin filter system. Left image is taken at E_{kin} = 10 eV and the right image is taken at E_{kin} = 38 eV. The pass energy was set to 30 eV. Superimposed blue lines as given by the CCD Acquire software from SPECS suggest the theoretical distortion produced by the transfer lens. Except of the extreme corners they do match the observed slit array patterns.

Depending on the deflector settings and magnetic stray fields, it might be additionally distorted or partly blurred. Regarding the real image scattering mode, the image sharpness is assumed to be best at the spot where the focus lies on the iridium crystal surface. Unfortunately, the scattering angle prohibits an area-wide focus along the angular axis while the energy distribution around E_p prohibits it in the energy dispersive axis.
Since small misorientated domains are unavoidable in the manufacturing process of large iridium crystals, the Sherman function and reflectivity will vary. The domains can be observed even with the naked eye by using a flashlight under certain reflection angles. The arising electron scattering contrasts between domains are highly dependent on the relative misorientation and change under variation of Φ or E_{kin}. Observed kinks in slit array images recorded with the reciprocal image scattering mode suggest small crystallographic inclinations of roughly 1°. Asymmetry differences between domains at different azimuthal crystal angles indicate additional azimuthal misorientations of approximately 2°. Normalizing the data by using a neutral master image can solve this issue. Another solution is the utilization scattering conditions where especially the contrast in the asymmetry almost disappears (see figure 4.6). Although misoriented domains are usually a disturbance, they have turned out to be useful. Their pronounced visibility was a reliable indicator for a successful crystal preparation leading to high asymmetries.

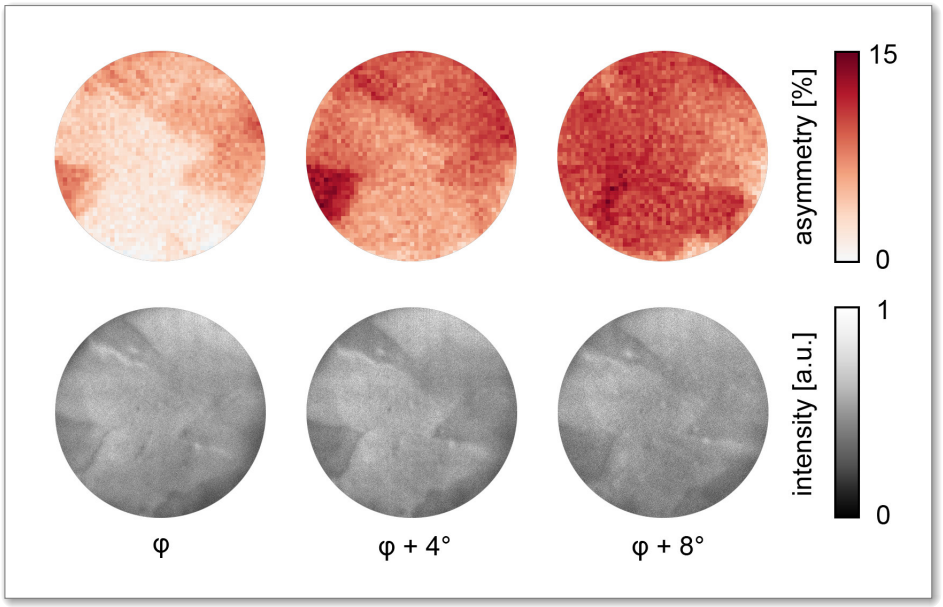

Figure 4.6: Image section of the relative intensity and asymmetry in percent for $E_{scatt} = 10$ eV and different azimuthal angles around $\varphi = 13°$. Reflectivity and Sherman function variations are clearly visible. The circle has a diameter of approximately 1 cm. A low-pass filter was applied to the intensity images to eliminate periodic patterns from electronics and multi-channel plates of the detector. The asymmetry image was binned with 8x8 pixels.

4.3 Resolution and Acceptance

Using the default wide angle mode with 30 eV pass energy and 10 eV scattering energy, an energy and angular acceptance of approximately 1.5 eV and ± 10° is possible. These values were determined by analyzing a slit array in front of the transfer lens and by analyzing the low-energy cutoff position at different sample bias voltages. While the angular acceptance is determined by the adjustable angular dispersion of the transfer lens, the energy acceptance can be changed by tuning E_p and linearly adjusting the first electron optical element of the spin-filter (see figure 3.5).
In addition to the spectrometer and spin filter lens settings, the maximum resolution of the setup is highly dependent on the sample position, excitation spot size and position, iridium surface condition, magnetic shielding and deflector settings. Our resolution limit was determined by using secondary electrons from the well-focused electron gun. The VUV lamp produced naturally inferior results due to the relatively big excitation spot.

Generally, the spectrometer energy resolution ΔE_{theo} without spin filter is given by [58,84]:

$$\Delta E_{theo} = E_p \left(\frac{d}{2R_0} + \alpha^2 \right), \tag{4.1}$$

$$\alpha = \arcsin \left(\frac{\sin(\alpha_{acc})}{M} \cdot \sqrt{\frac{E_k in - WF}{E_p}} \right). \tag{4.2}$$

In our case, 0.2 mm is the smallest entrance slit width d and $R_0 = 150$ mm the mean trajectory radius. In the wide angle mode, the α^2-term contains an acceptance angle in energy direction of $\alpha_{acc} = \pm 2.3 \cdot 10^{-3}$ rad, a magnification of $M = 0.7$ (according to SPECS support) and a sample dependent work function WF. Since the total contribution of the α^2-term is negligible, the maximum resolution is $\Delta E_{theo} = 20$ meV for our default pass energy of 30 eV.

Analyzing the low-energy cutoff edge of pristine tungsten was used to determine the experimental resolution. The edge was therefore fitted by means of least squares using a modified cumulative distribution function containing the complementary error function $erfc$:

$$I\left(E_{kin}\right) = \frac{a_0}{2} erfc \left(\frac{a_1 - E_{kin}}{a_2} \right) + a_2, \tag{4.3}$$

$$\Delta E_{exp} = 2\sqrt{ln2} a_2. \tag{4.4}$$

Here, a_0 is the magnitude, a_1 defines the position of the step, a_2 reflects the width of the edge and a_3 represents a constant offset. With the attached spin filter we have measured a peak energy resolution of $\Delta E_{exp} = (27 \pm 1)$ meV which decreases radially. Naturally, reducing the pass energy will improve the resolution.

In contrast to that, the angular resolution $\Delta\alpha_{theo}$ along the corresponding axis is dependent on the wide angle mode dispersion D = 0.75 mm/°, the magnification M = 0.7 and the spot size d_{spot}:

$$\Delta\alpha_{theo} = \frac{M d_{spot}}{D}. \tag{4.5}$$

With our slit array in front of the analyzer transfer lens, we could measure a peak resolution of $\Delta\alpha_{exp} = (0.23 \pm 0.01)°$ which would correspond to a spot size of 0.25 mm. Setting the analyzer to a higher dispersion will naturally improve this value. However, this was not further pursued.

The theoretical limit of resolved data points N for a circle of 1.5 eV and ±10° is given by:

$$N = \frac{\pi}{4} \frac{1.5eV}{\Delta E} \frac{20°}{\Delta\alpha}. \tag{4.6}$$

If ΔE_{exp} and $\Delta\alpha_{exp}$ would be constant all over the crystal, N would be $3.8 \cdot 10^3$. Considering the resolution decrease to the image border, an estimated value around $N = 10^3$ is

reasonable. Since ΔE_{theo} and the energy acceptance scale with the pass energy, a change of the pass energy should not influence N presupposed that the optical performance of the spin filter part remains constant. The same is valid for $\Delta\alpha_{theo}$ and the acceptance angle, which scales with the angular dispersion and spot size. Thus, increasing N is only possible by reducing the spot size, increasing the field of view or improving the resolution limit inherent to the spectrometer. In our setup, scattering a larger area of the exit plane at the iridium crystal was accompanied by an unacceptable angular distribution of the trajectories, suppressing the appearance of asymmetry. The reasonable scattering energy range leading to high asymmetries is in any case limited.

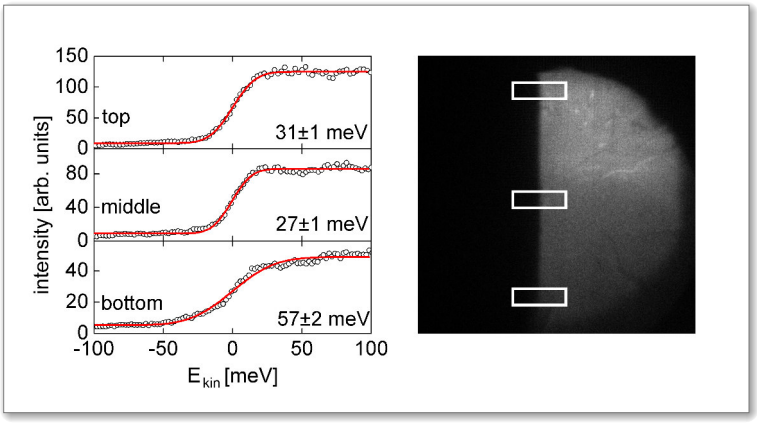

Figure 4.7: Energy resolution according to equation 4.4. For the energy resolution, a pass energy of 30 eV kinetic energy of 9 eV and an iridium bias of 1 V was used. This equals a scattering energy of 10 eV. The tungsten bias voltage was varied until the low-energy cutoff edge was in in the center of the image (here 7 V, value varied depending on settings).

At $E_{kin} = 39$ eV, a resolution of 134±23 meV and 0.44±0.04° was observed in the Gaussian scattering mode. For the reciprocal scattering mode at $E_{kin} = 10$ eV, a resolution of 67±15 meV and 0.33±0.02° was observed. Both values are relatively large compared to the previous values. This is partly caused by the omitted time-consuming fine-tuning of the spin filter lens voltages and deflectors and the high sample bias voltage for the 39 eV condition.

With the He VUV lamp, the resolution drops due to the larger spot size. An image of the Fermi edge for a cooled W(110) crystal measured in the wide angle mode at $E_p = 30$ eV, $E_{kin} = 10$ eV and $d = 0.5$ mm is shown in figure 4.9 (c). The continuous-flow cryostat was operated with liquid nitrogen but the flow rate as well as the crystal temperature were unknown. The line scan of the Fermi edge results in a resolution of 85±3 meV (see figure 4.9 (b)). This would correspond to a temperature of roughly 247 K assuming the relation $\Delta E = 4k_BT$. Assuming that the sample was significantly cooler, this value must

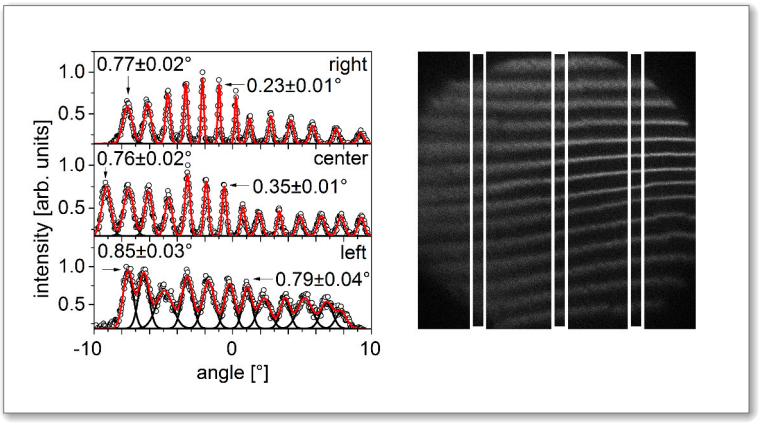

Figure 4.8: Angular resolution checked with the slit array in front of the transfer lens. A Gauss multi peak fit was applied to the profile. The pass energy was set to 30 eV. E_{kin} and the scattering energy were 10 eV.

be the consequence of a relatively large VUV lamp spot size. The same is observed for the angular resolution (see figure 4.9 (a) and (d)). A peak value of 0.51° has been observed in the center of the image. This would correspond to a spot size of 0.55 mm. However, the background is relatively high and the angular resolution becomes much worse to the corners.

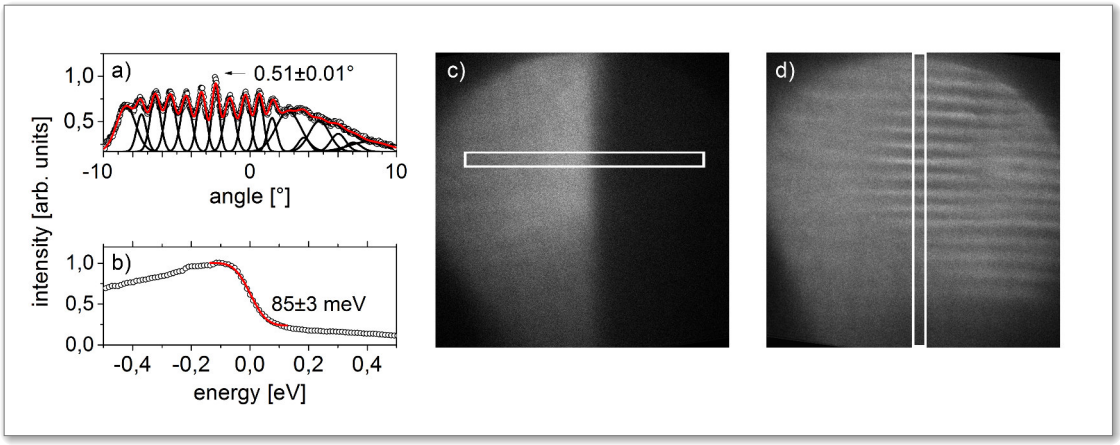

Figure 4.9: Energy resolution with the same settings as shown in 4.7 according to equation 4.4. The W(110) sample was cooled with a continuous-flow cryostat and liquid nitrogen.

4.4 Lifetime and Temperature

The spin filter efficiency is highest for a freshly prepared and clean crystal by means of annealing under oxygen atmosphere and a subsequent high-temperature flash. As expected, neither intensity nor asymmetry (through spin-flip processes) are visibly influenced by phonons from a residual temperature of up to 250°C as shown in the figure 4.10 (a)-(c). The low asymmetry in this measurement series originated from an omitted annealing under oxygen atmosphere. The observed constant intensity is important to avoid asymmetry offsets. In principle, phonons can change the momentum of scattered electrons which reduces the intensity of the specular beam (see [25], [45, p. 19]). In our case, the temperature must have been to low to see this effect. According to these results, measurements can therefore be started only minutes after the high temperature flash. The asymmetry starts to drop after the preparation mainly due to residual gas adsorption.

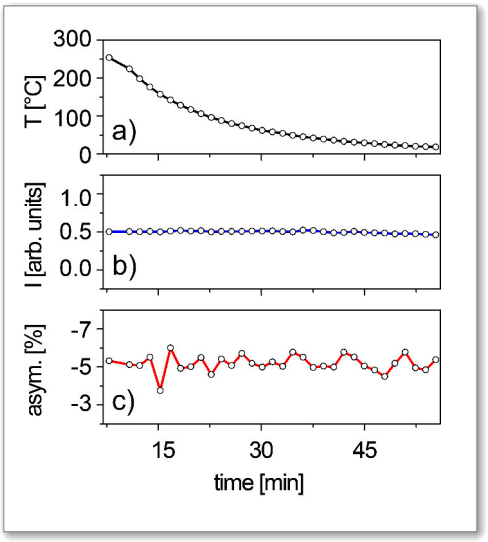

Figure 4.10: (a) Residual temperature at the iridium crystal measured with a thermocouple. The high-temperature flash was done at the zero-point. Intensity (b) and asymmetry (c) evolution after a high-temperature flash is plotted to evaluate the influence of the crystal temperature.

At a pressure of $1.0 - 1.5 \cdot 10^{-10}$ mbar, we recorded intensity and asymmetry values over several hours to determine the lifetime of the iridium spin filter . Although a non-linear asymmetry decrease is expected, we could approximately observe a linear behavior over the first three hours. An applied linear fit to the data revealed a decline rate of 1.26 $\frac{\%}{h}$ and a lifetime of $6\frac{1}{6}$ hours . Moreover, a high-temperature flash after $3\frac{3}{4}$ hours could recover the asymmetry from around 11 to 13% (see figure 4.11 (b)). A full recovery was only possible by repeating the annealing procedure and subsequently preforming a high-temperature flash before starting the measurement. In a separate series that showed an asymmetry of roughly 5% due the ommited annealing procedure, we found a decline rate

of 0.32 $\frac{\%}{h}$ and a lifetime of over $9\frac{1}{2}$ hours at a pressure of $1.0 \cdot 10^{-10}$ mbar by using a linear fit (see bottom figure 4.11 (a)). The asymmetry decline rate is approximately four times lower for contaminated iridium surfaces.

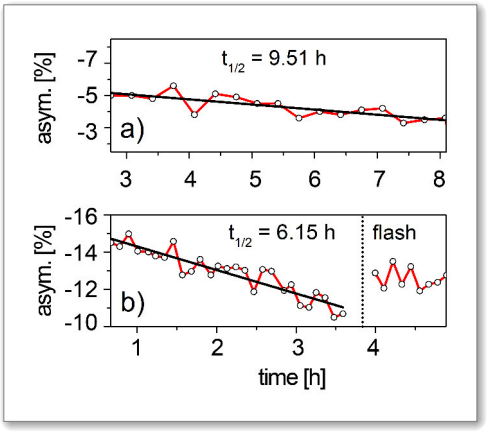

Figure 4.11: (a) Lifetime determination for an unannealed but flashed iridium. (b) Lifetime determination of an annealed and flashed iridium crystal and the recovery by single a high-temperature flash.

4.5 Energy and Azimuthal Dependence of the Spin Sensitivity for Ir(001)

A detailed characterization of the scattering energy dependence and azimuthal dependence on the intensity, asymmetry and FoM was performed and the results were displayed in two-dimensional maps. The azimuth was varied from -45° to 45° with respect to the Ir(001)-(5x1) mirror plane (e.g. [100]). This is sufficient due to the 4-fold symmetry of the Ir(001) surface. The [100] mirror plane is defined according to figure 4.12. The spectrometer was set to the wide angle mode and the iris diameter was smaller than 20 mm. The entrance slit was 3x20 mm^2 or 7x20 mm^2, while the exit slit was equipped with the fine mesh. The scattering energy of 5-15 eV was adjusted with iridium bias voltages (E_{kin}=10 eV). The same was done for scattering energies between 34-44 eV (E_{kin}=39 eV). The spin filter lens was operating in the Gaussian scattering modes. The incoming spin-polarized secondary electron polarization was aligned by the easy axis-magnetization of 15 ML Fe/W(110) samples. They were installed with the $(\overline{\Gamma N})$/[110] or the $(\overline{\Gamma H})$/[001] along the angular dispersive analyzer axis to obtain either a full in-plane (P_e) or full out-of-plane (P_n) spin polarization at the scattering crystal.
Each map was measured within 3-5 hours. Asymmetry lifetime corrections have not been applied to the raw data. Each scattering energy series was measured for all azimuthal angles before going over to the next scattering energy. An energy calibration was also not applied. The real energy axis can therefore be slightly shifted, since it is not completely

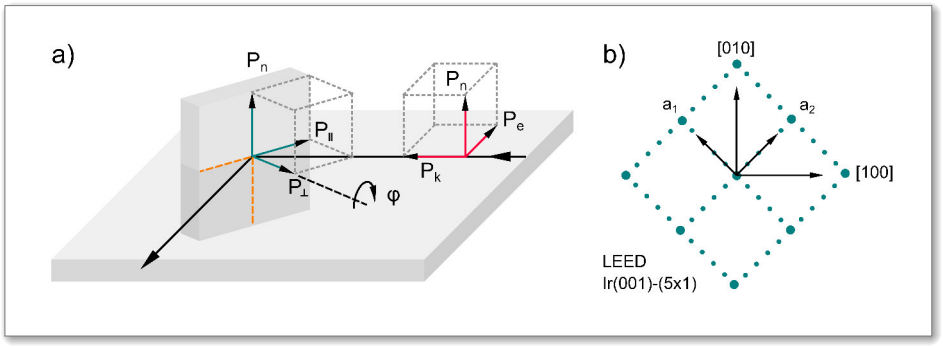

Figure 4.12: (a) Spin polarization components for the scattering at the spin filter crystal. See figure 2.12 for further details. (b) Scheme of a LEED image produced by the Ir(001)-(5x1) reconstruction. The corresponding axes are labeled.

clear which part of the exit plane and thus which scattering energy interval arrives at the iridium. Each pixel denotes one energy-azimuth setting. The values were calculated from a circle in the center of the detector image with a diameter of 300 px, corresponding to an energy, angle interval of 0.75 eV and 12.5°. This was needed to obtain enough statistics and keep the influence of iridium domains small. A smaller analysis circle diameter did not reveal any further details. The scattering angle variations and the angular spread is described in section 4.1. Asymmetries were calculated by dividing the difference of the accumulated counts of the oppositely magnetized samples through the sum of all counts within the circular area. Intensity and FoM are given as relative values. The recording time was 5 s for the 39 eV maps or 10 s for the 10 eV maps per sample magnetization polarity and scatterin condition. A single magnetization reversal procedure was sufficient since the obtained values were stable. Bias voltages from -5 V to 5 V in steps of 0.5 V and azimuthal angles between -45° and +45° in steps of 5° controlled by a stepper motor were applied to the iridium crystal to record the maps consisting of 21x19 data points in total. A programmed AutoIt master script controlled all devices and programs during the measurement (CCD Acquire software, LabVIEW voltage control, capacitor charge and magnetization pulse, azimuthal angle of the iridium) and automatically saved the results. The data was then evaluated and visualized using Python scripts. All results are shown in figure 4.13 and 4.15.

The 5-15 eV out-of-plane setup (fig. 4.13 (d)-(f)) shows a symmetric intensity and asymmetry behavior $A(P_n, \varphi) = A(P_n, -\varphi)$ around the 0° crystal mirror plane as expected from theory. The asymmetry measured here shows a maximum negative value around $\varphi = 0°$ and $E_{scatt} = 10$ eV (see fig. 4.14 (b)). Going from higher to lower scattering energies, an asymmetry polarity change is found around 0° and 7.5 eV (see fig. 4.14 (b)). Here, the intensity shows a minimum. These results are in agreement with [56]. In total, three large and elongated red regions with negative asymmetry and one small blue region with positive asymmetry are found in total. The intensity shows three elongated regions

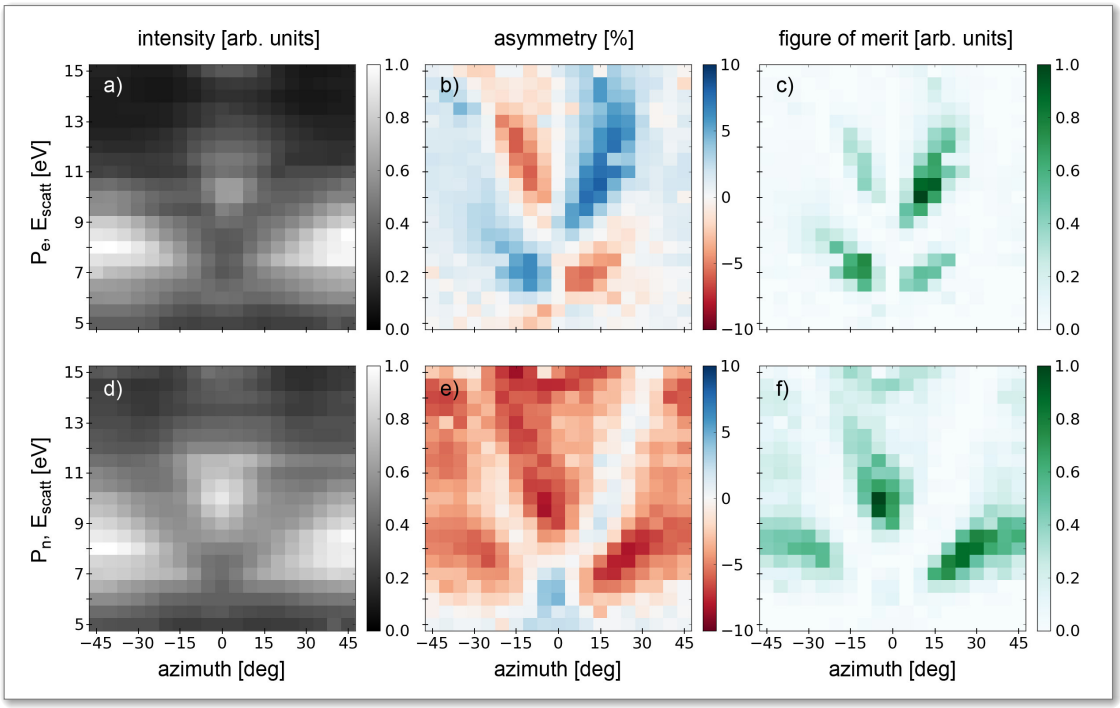

Figure 4.13: Energy and azimuthal dependence on intensity, asymmetry and FoM for an in-plane and out-of-plane spin polarization (P_e, P_n). The pass energy was set to 30 eV and the entrance slit was 3x20 mm^2. E_{kin} and the scattering energy was 10 eV. A bias of ± 5 V was applied to the iridium to vary the scattering energy.

with higher values. An intermediate intensity minimum near 10 eV as seen in theory and experiment from [56] does not appear. The averaging of azimuthal and polar scattering angles as well as scattering energies are a possible explanations for this missing feature. Fortunately, the high-intensity regions match with the red regions of the negative asymmetry, which entails relatively large FoM values. Only the small positive asymmetry region around 6.5 eV coincides with a low-intensity area. It is not surprising that the FoM shows accordingly only three favorable scattering conditions (fig. 4.13 (f)). The already known scattering condition around 10 eV and 0° shows large values within approximately ±1 eV and ±5°. The new regions around 8.0 eV and ± 25° (see fig. 4.14 (a)) have comparable efficiencies and dimensions. We attribute the slight mirror symmetry imbalance around 0° to existent stray fields in our chamber and the macroscopic mosaic spread of slightly misaligned domains.

As expected, the 5-15 eV in-plane setup shows a similar symmetric intensity but an anti-symmetric asymmetry texture (fig. 4.13 (a) and (b)). The mirror symmetry dictates an asymmetry at $\varphi = 0°$ and 45° according to $A(P_e, \varphi) = -A(P_e, -\varphi)$. In this case, two red and two blue regions of high asymmetry and efficiency are found. They are located around 7 eV or 11 eV and ±15° (see fig. 4.14 (c)). Their usable area is smaller than the areas

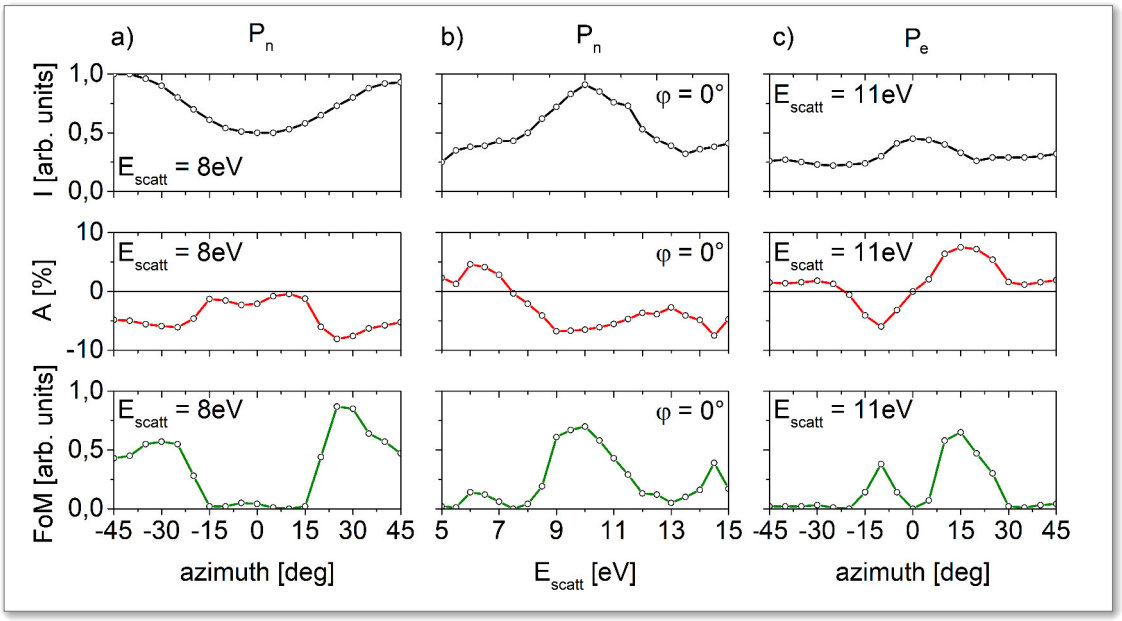

Figure 4.14: Intensity, asymmetry and FoM line scans for (P_n, E_{scatt} = 8 eV, φ = [-45,45]°) (a), (P_n, E_{scatt} = [5,15] eV, φ = 0°) (b) and (P_e, E_{scatt} = 11 eV, φ = [-45,45]°) (c)

found in the out-of-plane setup but the measured peak asymmetry value is very similar to the out-of-plane setup. A P_n component produces interestingly nearly no asymmetry at these scattering conditions according to figure 4.13 (e). A previously unappreciated possibility of generating asymmetry is hereby uncovered. Besides generating asymmetry by changing the scattering energy or switching the initial beam polarization through a sample magnetization reversal, it is also possible to vary the azimuthal angle. Under disregard of iridium domains, opposing azimuthal angles do not require a reflectivity correction as needed for the scattering energy variation method. Furthermore, a contribution of the P_n component vanishes. By the azimuthal variation, scattering energy and beam polarization can be kept constant. This new possibility was announced in [80]. An advantage over the scattering energy variation method is the redundancy of a spin filter lens adaption which would vary imaging properties. Another important advantage is the possibility to tilt the sample to map the perpendicular momentum without losing spin sensitivity by polarization component variations. A disadvantage of the azimuthal variation is the necessity of intensity variation corrections originating from scattering crystal domains. Especially the Gaussian scattering mode suffers from this problem.

For the 34-44 eV out-of-plane setup (fig. 4.15 (d)-(f)), a large intensity around 0° is seen. It decreases with increasing scattering energy. Towards 34 eV, a periodic intensity variation in dependence of the azimuth is visible. As for the asymmetry, three blue areas symmetric around the mirror plane is visible. Maximum asymmetry values are at least two times smaller than seen in the 5-15 eV case. The broad central area around 0° and

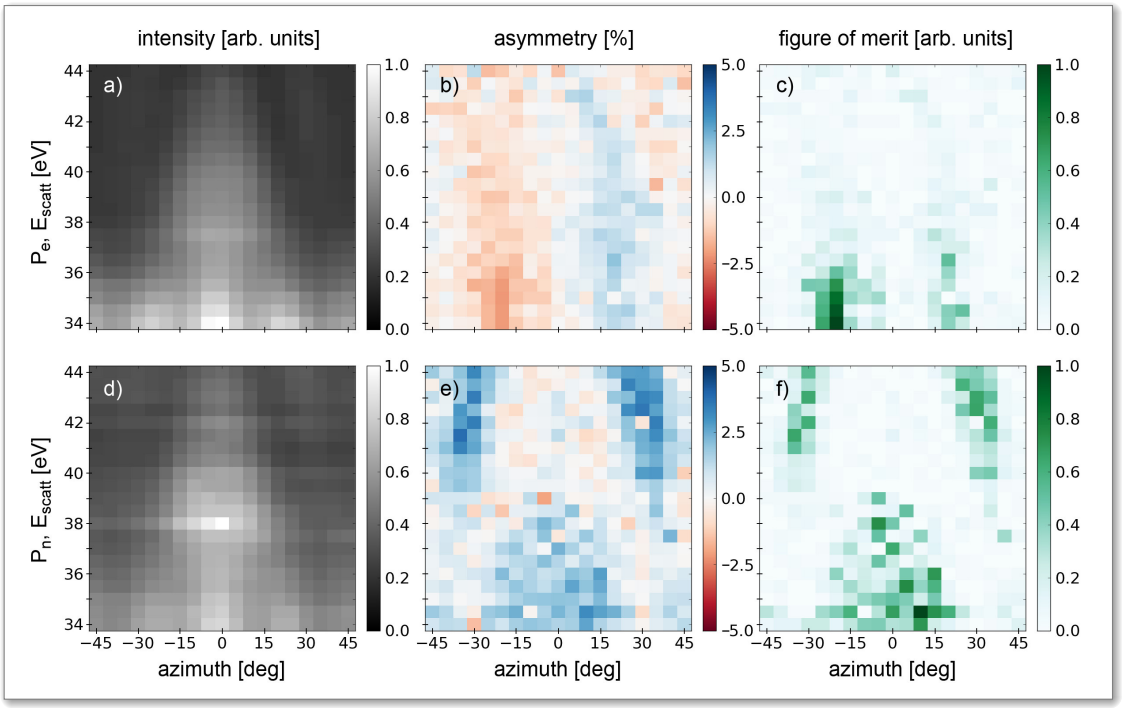

Figure 4.15: Energy and azimuthal dependence on intensity, asymmetry and FoM for an in-plane and out-of-plane spin polarization (P_e, P_n). The pass energy was set to 30 eV and the entrance slit was 7x20 mm^2. E_{kin} and the scattering energy was 39 eV. A bias of ± 5 V was applied to the iridium to vary the scattering energy.

34 eV (see fig. 4.16 (b)) is surprisingly not very pronounced and corresponds to the broad maximum as reported in [56]. It is over 30° broad but has a much lower spin sensitivity. The expected asymmetry feature as calculated and measured in [56] is found at lower energies. The additional two elongated regions are located around 42 eV and ± 30° (see fig. 4.16 (a)). They measure around 3 eV in height and 10° in width. Generally, the FoM is very similar for all three regions. In comparison to the 10 eV setup, the absolute FoM value is lower. Precise values cannot be calculated because the reflectivities are unknown. In the case of the 39 eV in-plane setup, the intensity map remains unchanged but the asymmetry texture is again antisymmetric around 0°. It shows two large vertically aligned areas with opposite sign of several eV in height and around 20° in width. The FoM value is largest around 34-36 eV (see fig. 4.16 (c)). Lower energies were not covered by the measurement series and might be usable. Again, the asymmetric behavior enables the possibility of changing the azimuth instead of scattering energy or magnetization reversal to generate asymmetry.

Generally, the maximum measured asymmetry in the range from 34 to 44 eV was less than half the value of the 5-15 eV region. Besides physical reasons, the higher angular distribution and spread might have contributed to this outcome. Intensity images and

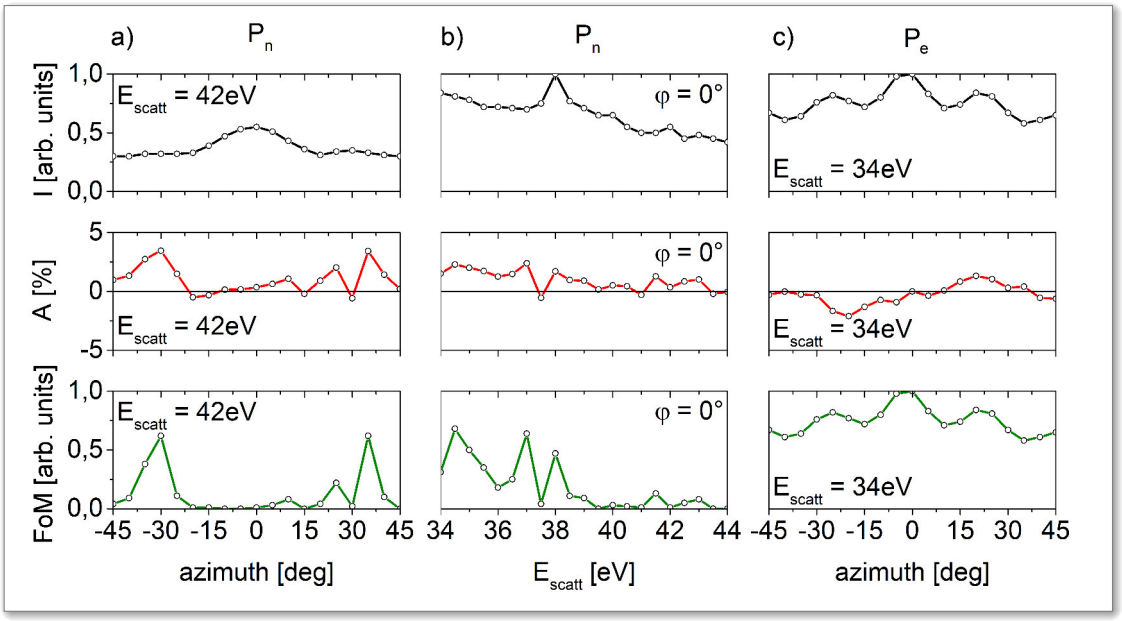

Figure 4.16: Intensity, asymmetry and FoM line scans for (P_n, E_{scatt} = 8 eV, φ = [-45,45]°) (a), (P_n, E_{scatt} = [34,33] eV, φ = 0°) (b) and (P_e, E_{scatt} = 34 eV, φ = [-45,45]°) (c)

the corresponding asymmetry measured in the Gaussian scattering mode for each mentioned scattering condition are shown in figure 4.17 and 4.18. Reflectivity and Sherman function fluctuations as well as field of view shifts are partly visible. The visibility of iridium domains depends on the azimuthal angle. Overall, the highest asymmetry was always observed in Gaussian scattering mode in combination with the wide angle mode at the 10 eV 0° scattering condition for P_n and at the 11 eV ±15° scattering condition for P_e. Directly after a complete iridium preparation cycle, local peak asymmetries of around 15-20% were often measured with the spin-polarized secondary electrons. The obtained maximum asymmetry was dependent on the iridium and iron preparation quality, on the electron gun spot size and position and on the spectrometer settings. A small entry slit drastically minimized the angular spread at the exit plane of the analyzer and thus at the iridium crystal. Assuming a secondary electron polarization of 45%, the measured asymmetry would correspond to a Sherman function of 0.30-0.44.

A measurement of the P_k polarization component was technically possible but demanding. According to figure 4.12, one would expect the same Sherman function ($S_p = S_e$) for the P_e and P_k detection, because they can be split into the components $P_{\parallel}$ and $P_{\perp}$. The Sherman function $S_{\perp}$ for $P_{\perp}$ is zero so that only $P_{\parallel}$ should contribute to the asymmetry. However, calculations for a scattering angle of 44° have shown that this is not the case and S_p is unequal to S_e [7] [45, p. 81]. Although the antisymmetric behavior with respect to the scattering crystal mirror plane similar, there are pronounced differences that must be a consequence of multi-scattering effects and cannot be easily explained. To measure

the asymmetry for P_k (see figure 4.12), the sample had to be magnetized first into the out-of-plane direction with respect to the scattering plane. Then it was tilted by almost 90° in order to produce a longitudinally polarized electron beam. By applying a negative bias voltage, adjusting the position of the sample and the changing the electron gun spot, it was possible to guide the electrons into the spectrometer lens. For a magnetization reversal, the sample was again in the initial orientation. Measurements for 10 eV scattering energy were performed several times but the outcome did not meet the expectations. Although the measured asymmetry became almost 0% around $\varphi = 0°$, it was not antisymmetric for the other angles with respect to 0°. Instead, the symmetry became reproducibly negative to both sides. A combination of magnetic stray fields and bad imaging properties were probably the reason for this.

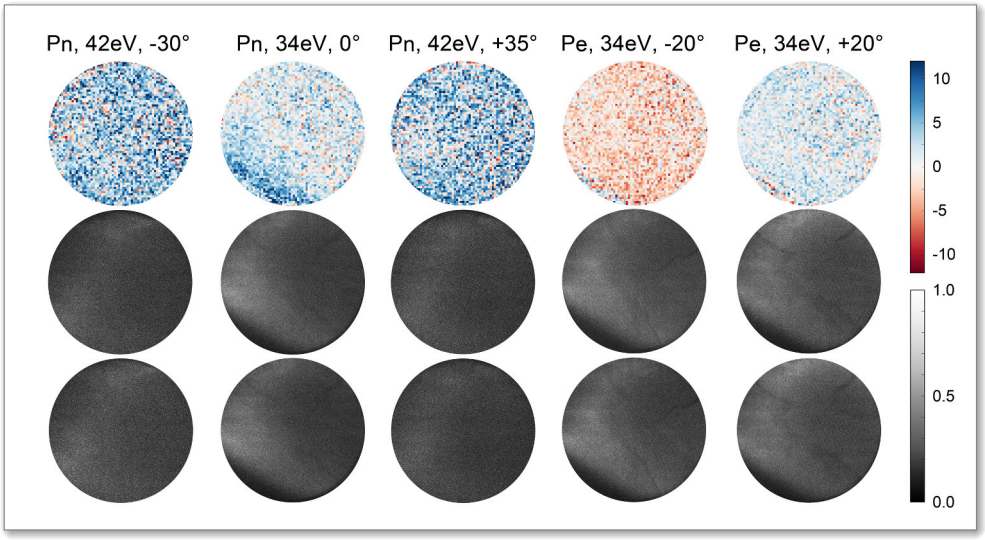

Figure 4.17: Intensity (denoised) and asymmetry (Gaussian blur with $\sigma = 1$ and 8x8 pixel binning) images for different scattering conditions. The field of view is approximately 1.5 eV and ±9°.

4.6 Spin Manipulation with Longitudinal Magnetic Fields

For further investigation of the effect of different spin components on the scattering asymmetry we apply an external longitudinal magnetic field that originates from a current of a few amperes through a ten-turn coil around the vacuum chamber in the vicinity of the magnetically permeable plate valve region. The imaged energy slit arrays were already rotated by 10° without applying any current due to residual magnetic fields. In contrast to that, the angular slit pattern was almost horizontal. This fact indicates a complex image rotation and shear. A vertical alignment of the energy slits is obtained with a current of

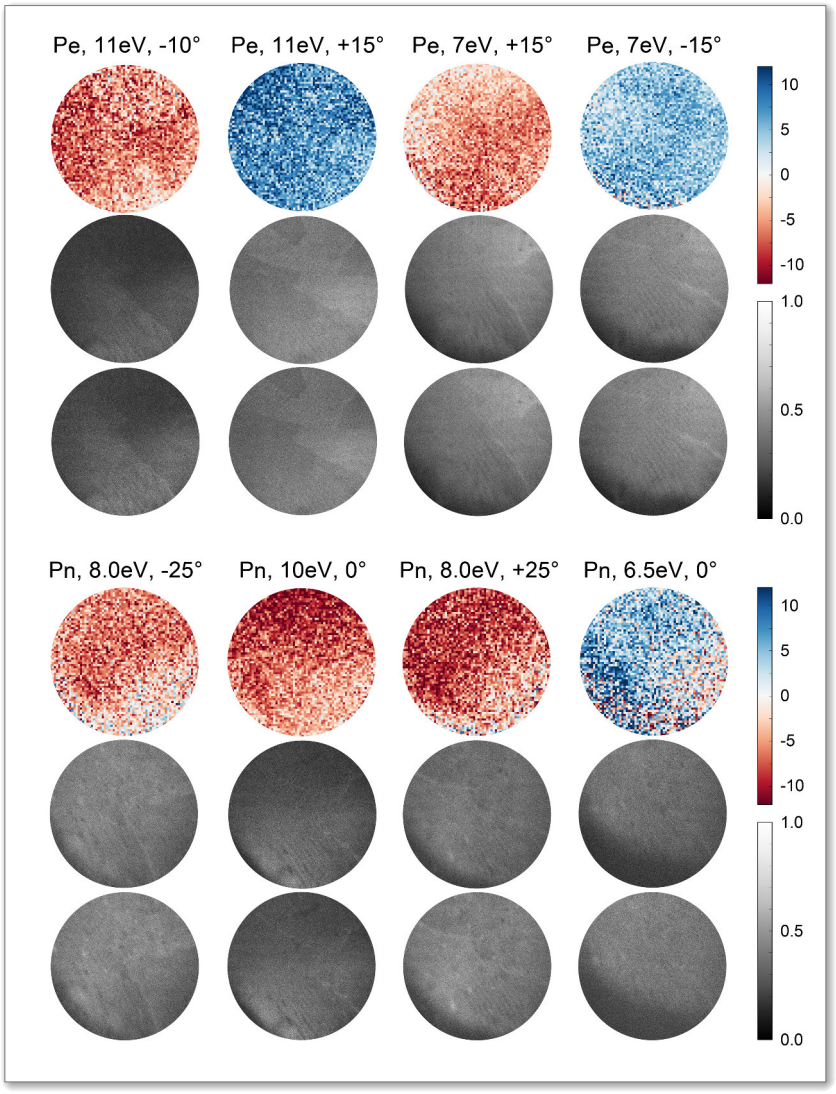

Figure 4.18: Intensity (denoised) and asymmetry (Gaussian blur with $\sigma = 1$ and 8x8 pixel binning) images for different scattering conditions. The field of view is approximately 1.5 eV and ±9°.

+0.75 A. By applying +0.75 (0.03 mT) to -2.5 A (0.14 mT), we could rotate the energy slit array from 0° to 40° (see right figure 4.19).
The image quality decreased slightly with higher currents but all slits were still clearly visible (see right figure 4.20). The scattering energy was fixed at 10 eV while the coil current as well as the azimuthal angle were varied. The result is shown in the left figure 4.20. As expected, a smooth transition from a symmetric (at 0.75 A) to an antisymmetric (at 2.5 A) behavior is visible. The magnetic stray fields that create a small image rotation of 10° explain the small imbalances in the previously shown energy-azimuth maps around 0°.

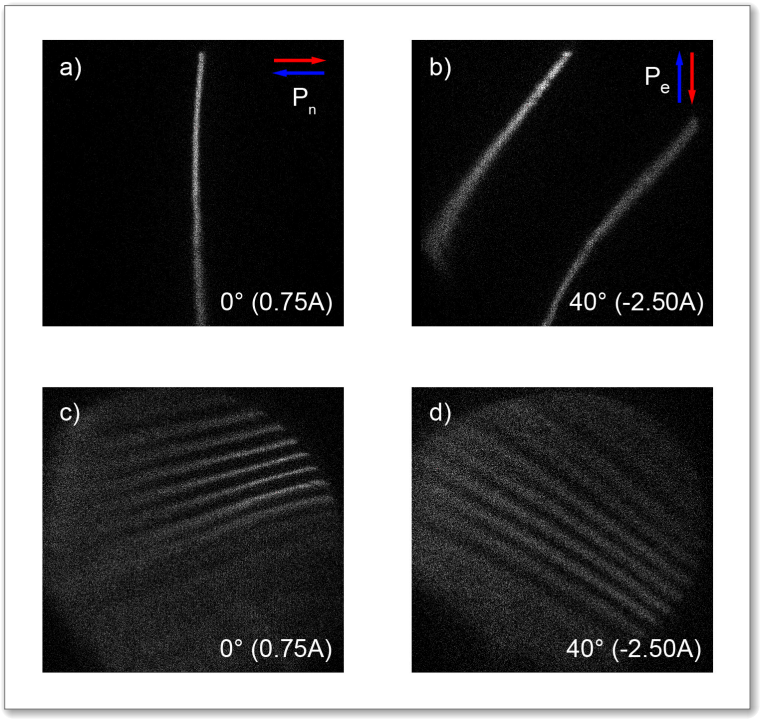

Figure 4.19: Images of the energy slit array and the angular slit array are shown for an applied coil current of 0.75 A (0°, see (a), (c)) and 2.50 A (40°, see (b), (d)).

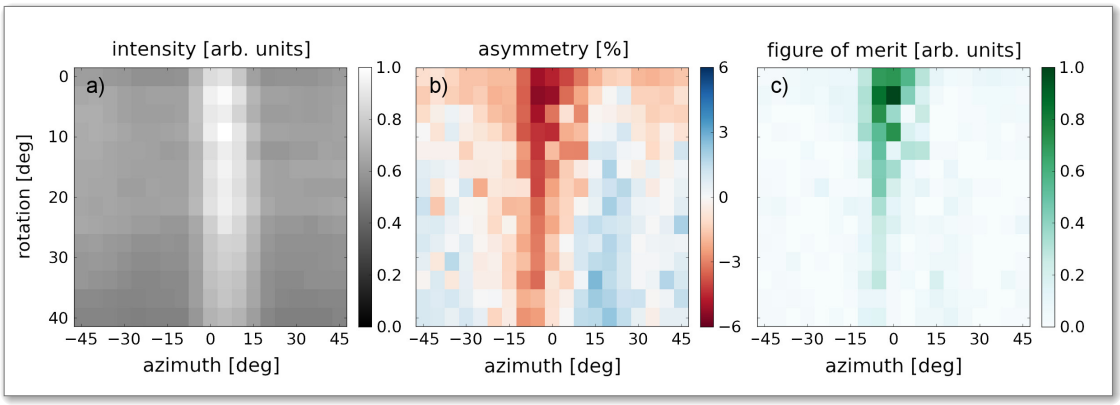

Figure 4.20: Intensitay (a), asymmetry (b) and figure of merit (c) for a scattering energy of 10 eV. A coil current of 0.75 A (0°) to 2.50 A (40°) was applied to transform the out-of-plane spin polarization component (P_n) into the in-plane component (P_e).

4.7 Vectorial Spin Analysis

The results shown in section 4.5 and 4.6 reveal a powerful method for a vectorial 3-dimensional spin analysis without changing the scattering angle or using multiple detector

systems. All three polarization components of the polarization (P_n, P_e, P_k) vector can be determined if the Sherman functions (S_n, S_e, S_k) of the iridium crystal are known from a calibration. This is particularly important for the investigation of the complex spin textures that have been predicted for topologically protected surface states in topological insulators and Weyl systems. The evaluation procedure is explained in the following.
Two disjunct scattering conditions (e.g. W_1:(E_{scatt} = 10 eV, φ = 0°, α_{rot} = 0°) and W_2:(E_{scatt} = 11 eV, φ = -15°, α_{rot} = 0°)) were already successfully used to determine the P_n and P_e polarization components. Due to the time reversal symmetry, the W_1 scattering condition is only sensitive to the P_n component. For the W_2 scattering condition, the P_n asymmetry map fortunately revealed a vanishing sensitivity for the P_n component. Here, only P_k and P_e contribute to the asymmetry. The spin polarization of a ferromagnetic sample can be easily aligned to eliminate a P_k component so that the W_2 represents an unambiguous result for P_e. However, if a P_k component is present a third scattering condition (e.g. W_3:(E_{scatt} = 11 eV, φ = -15°, α_{rot} = 90°)) can be used to unambiguously determine P_e and P_k. Here, a longitudinal field is used to rotate the spin polarization by α = 90°. The P_n component is then filtered with S_e. The P_e component does not affect the measurement since S_n is zero for the scattering condition W_3. P_k is now filtered with S_k. In total, three measurable asymmetry observables (A_1, A_2, A_3) result from the measurements at the three scattering conditions (W_1, W_2, W_3). Inverting the corresponding system of equations (4.7) determines the three components (P_n, P_e, P_k) of the spin polarization vector:

$$\begin{pmatrix} A_1 \\ A_2 \\ A_3 \end{pmatrix} = \begin{pmatrix} S_n & 0 & 0 \\ 0 & S_e & S_k \\ S_e & 0 & S_k \end{pmatrix} \begin{pmatrix} P_n \\ P_e \\ P_k \end{pmatrix}. \tag{4.7}$$

The described method works for magnetic materials, where the asymmetry is generated by a reversal of the magnetization. However, is also possible to determine the full polarization vector of non-magnetic materials where no polarization inversion is producible by a magnetization reversal. Here, the scattering condition conditions have to be varied to generate the asymmetry. Exemplary scattering conditions are W_1:(E_{scatt} = 10 eV & 6.5 eV, φ = 0°, α_{rot} = 0°), W_2:(E_{scatt} = 11 eV, φ = +15° & -15°, α_{rot} = 0°) and W_3:(E_{scatt} = 11 eV, φ = +15° & -15°, α_{rot} = 90°). The first scattering condition generates a high asymmetry by changing the scattering energy. The second and third scattering conditions exploit the asymmetric azimuthal dependence to obtain a high asymmetry. Once the three Sherman functions S_i have been determined, equation (4.7) can be used to determine the three polarization vector components P_i from the three measurements A_i. The corresponding system of equations is again described by (4.7). A measurement of all three observables and the inversion leads to the polarization components.

4.8 Comparison to Theory

The measured maps are compared to theoretical asymmetry and effective reflectivity maps from spin-polarized low energy electron diffraction calculations based on fully relativistic multiple scattering in the framework of spin-polarized density functional theory (see e.g. [11]). Fully polarized and well defined spin-components (P_n, P_e, P_k) are scattered at an iridium crystal with $\theta = 45°$. Due to technical reasons, a (5x1) iridium surface reconstruction could not be implemented. The calculations were done by Stephan Borek[1]. The results are shown in figures 4.21 and 4.22.

The 34-44 eV P_n map shows three areas with relatively strong asymmetry. The areas around $\varphi = 0°$ and 37 eV as well as $\pm 45°$ and 42 eV resemble the active areas in the measured map. For P_e, the antisymmetric behavior around 0° is visible. As expected from the measurements, the tendency of having mainly positive asymmetry between 0° and 45° and negative asymmetry between 0° and -45° is seen. The calculated areas near $\pm 45°$ and 40 eV appear marginally in the corners of the measured map. The calculation for P_k is mostly similar to P_e. Small differences occur in the range of $\pm 5\%$. Overall, the asymmetry for P_k is approximately half as large as for P_e. This fact demonstrates the inequality of P_k and P_e.

The calculations for 6-15 eV and P_n show a large area with high asymmetry around 11 eV and 0 °. This corresponds to the described experimental scattering condition around 10 eV. Also the V-shaped form towards higher energies is similar to the experimental data. The positive upwards directed side branches around 8 eV and $\pm 25°$ as found in the experiment are not found in the theory. Here, most of the area shows a negative asymmetry. Only around 6-7 eV, a positive asymmetry is found in the theory. For P_e, the expected asymmetric behavior around 0° is seen. The V-shaped structure around 11-12 eV and $\pm 10°$ is assigned to the experimental scattering conditions at 11 eV and $\pm 15°$. However, the experimental scattering conditions at 7 eV and $\pm 15°$ are not clearly represented. They might correspond to the calculated areas around 6 eV and $\pm 20°$. However, many fine structures are visible that do not occur in the experiment. For P_k, the behavior is partly similar to P_e. The main sensitive areas around $\pm 10°$ are existent but the asymmetry is visually exclusively positive between 0° and 45° and negative between 0° and -45°. Except of some changes in the magnitude, this is the major difference between these components.

The reflectivities for 34-39 eV (figure 4.22 (a)) show three vertical areas with relatively large values of 0.1. The central high-reflectivity region can be assigned to the large experimental high-intensity area around $\varphi = 0°$. At 34 eV the theoretical map reveals a similar intensity variation with peaks around $\pm 45°$, $\pm 25°$ and 0° which is also found in the experiment. Towards higher scattering energies and azimuthal angles, the deviation between experiment and theory becomes larger. For the 6-15 eV calculation, the relatively high reflectivities around 14 eV and 0° represents probably the high experimental

[1] stephan.borek@cup.uni-muenchen.de, Department of Chemistry, Ludwig-Maximilians-Universität München, Butenandtstraße 11, D-81377 München

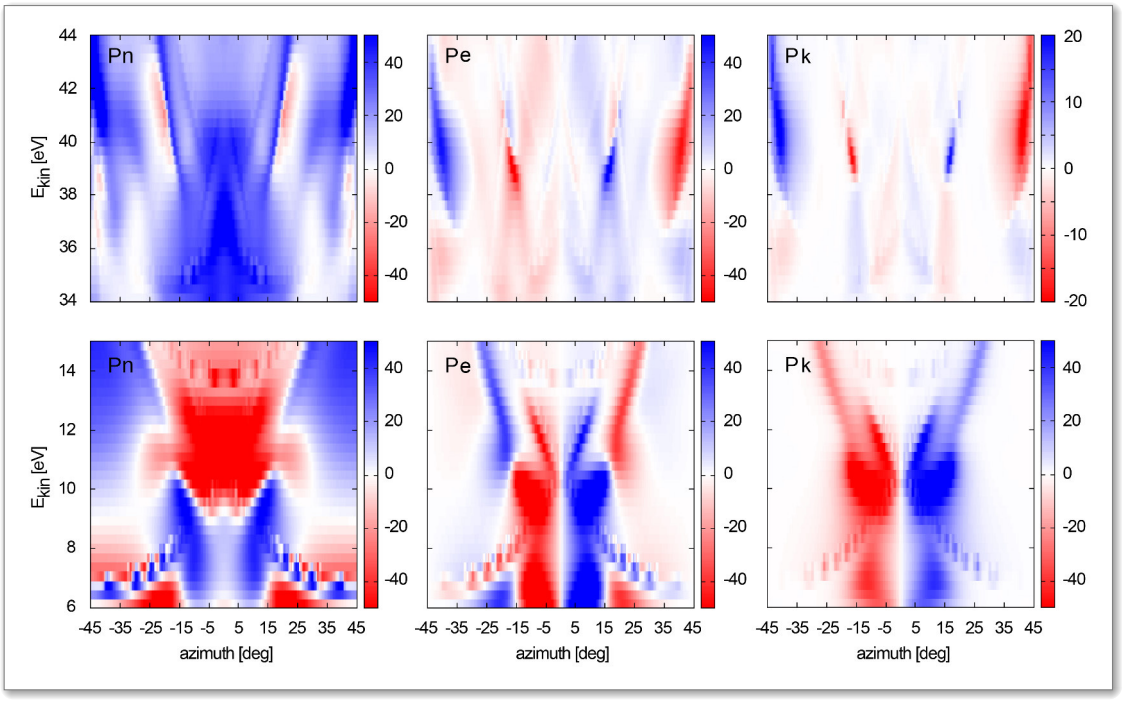

Figure 4.21: Calculations of the asymmetry in percent for each incoming spin polarization (P_n, P_e and P_k). The azimuthal angle ranges from -45 to 45° with respect to the scattering plane as defined in figure 4.12. (a)-(c) show an energy range from 34-44 eV and (d)-(f) show a range of 6-15 eV (taken from [76]).

intensity around 10 eV and 0°. The two theoretical areas around 10-15 eV and ±45° can be assigned to the experimental high intensity around 8 eV and ±45°. The experimental intensity minimum at 7.5 eV is much larger in the theory.

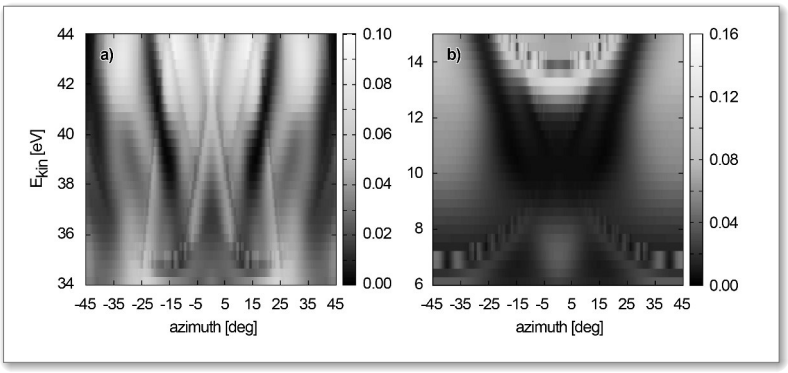

Figure 4.22: Calculations of the reflectivity in the ranges from -45 to 45° with respect to the scattering plane (a) for an energy range from 34-44 eV and (b) for a range of 6-15 eV (taken from [76]).

To summarize, the calculations fit qualitatively to the experimentally observed asymmetry and intensity. They are also comparable to the results from reference [56]. The remaining

differences are attributed to the electron optical imaging which comes along with an angular spread. As a consequence, an averaging over several scattering angles that deviate from the 45° scattering angle setpoint takes place (see section 4.1). The crystallographic misorientations and the asymmetry averaging over a circular field of view (0.75 eV and 12.5°) for the value calculation of each pixel in the map also contribute to the deviations. Finally, the (5x1) iridium reconstruction was not covered by the theory and its effect on the result is not known.

4.9 Spin- Energy- and Angle-Resolved Spectra of Fe/W(110)

Several spin and angle-resolved spectra of >30 ML Fe/W(110) have been recorded with the multichannel spectrometer and a He-VUV lamp ($h\nu = 21.2$ eV, 45° angle of incidence) at room temperature in the wide angle mode. The sample has been grown on a clean tungsten crystal at room temperature. Annealing of the Fe layer at 500-600 K for 10 minutes resulted in a smooth surface. The angular dispersive axis was along $(\overline{\Gamma H})/[001]$. Since the iron film thickness was >30 ML, the easy axis magnetization was along $(\overline{\Gamma H})$ and electrons were scattered in a full in-plane (P_e) geometry at the scattering crystal. The scattering energy and E_{kin} were set to 10 eV and φ was 15°. A bias voltage of 7.25-7.50 V was applied to the sample during measurement.

Measured intensities and asymmetries largely dependent on the excitation source polarization [108, p. 234], excitation energy [108, p. 236] and Fe thickness [108, p. 243]. Additionally, features of majority and minority electrons respond differently strong on the change of the light angle of incidence [12]. Dipole selection rules and transition probabilities have to be taken into account. For example, only bands with Σ_1, Σ_3 or Σ_4 can be observed at normal emission.

Figure 4.23 (a)-(f) shows two sets of (S)ARPES images. The top row was recorded at a pass energy of 30 eV, while the bottom row was recorded at 50 eV. This was possible by adjusting the spin filter lens as described in section 4.3. The Fermi level was set to the intensity cutoff position. Figure 4.23 (a) and (b) show the calculated asymmetry with a 8x8 pixel binning and an applied Gaussian blur ($\sigma = 3$) to the raw data. The images (c)-(f) show the denoised intensity data for both sample magnetizations (M^+ and M^-). The acquisition time of each picture was 1 minute. No distortion correction has been applied to the images.

Within the displayed angle and energy range of approximately ±9° and 1 eV ($E_p = 30$ eV) or 1.7 eV ($E_p = 50$ eV), the Fermi edge can be clearly seen. The minority electrons dominate below the Fermi edge due to the exchange splitting and produce two features with small dispersion. The sharp structure at -0.1 eV matches to a minority electron surface state as reported in reference [74], where the peak position does not change under variation of the excitation energy. The other features such as the asymmetry peak at -0.3 eV (minority state with Σ_1 symmetry) can be assigned to direct transitions. Possible

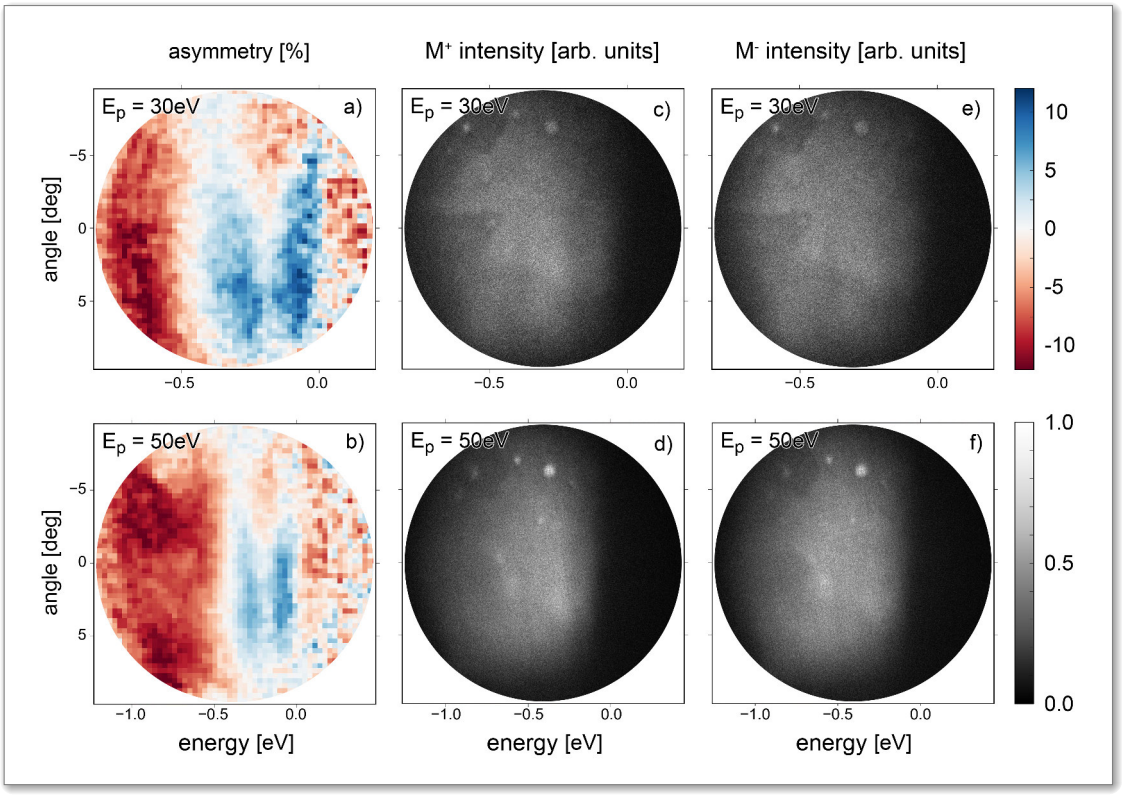

Figure 4.23: Spin-, energy- and angle-resolving photoemission spectroscopy for opposite sample magnetization (c)(e)(d)(f) and calculated asymmetry images (a)(b) from >30 ML Fe/W(110) recorded in the wide angle mode with the angular dispersive axis along ($\overline{\Gamma H}$) at E_p = 30 eV (a)(c)(e) and E_p=50 eV (b)(d)(f).

direct transitions into the primary Mahan cone can be identified as crossing points of the calculated band structure and the free energy parabola shifted down by the excitation energy [81] (see figure 4.25 (c)).

On closer inspection, a higher intensity of minority electrons can be also seen in figure 4.23 (c)(d). The features diverge and vanish towards larger emission angles. Their asymmetry around normal emission reaches locally peak values of 10% and 8%. This corresponds to a spin polarization of 26% and 21% when assuming a Sherman function of 0.38. As expected, a pronounced polarity change of the asymmetry is visible around -0.5 eV below the Fermi edge (see [53]). The majority electrons (Σ_1 and Σ_4 symmetry states) start to dominate at energies <-0.5 eV and produce asymmetries of up to 16%, which is equivalent to a spin polarization of 42%. These observed peak values are by a factor of two smaller than observed in reference [53] for 10 ML Fe/W(110). Possible reasons for this are a surface contamination of the iron sample, lifetime effects of the iridium spin filter and the averaging of azimuthal and polar angles caused by the lens and analyzer settings.

Figure 4.24 shows line scans taken from 4.23 (a) and (b) within an interval of ±1.7°. Both diagrams show the same behavior whereas the noise is lower for E_p = 50 eV due to the

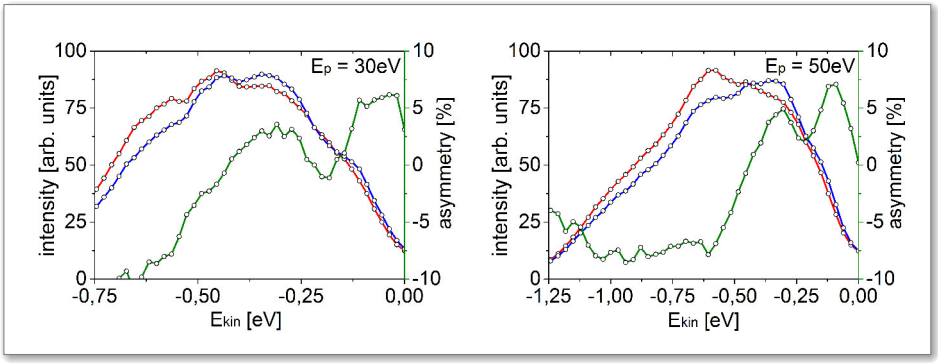

Figure 4.24: Line scans taken from the data shown in figure 4.23. The red and blue line depict the intensities measured for the different sample magnetizations. The green line is the calculated asymmetry. The energy has been calibrated by analyzing E_F shifts with bias voltages.

higher intensity. The total intensity near the Fermi edge is dominated by 3*d* states and in accordance to experimental results shown in figure 4.25 (a) [93], which were measured at similar conditions. A small shoulder around -0.1 eV, which was identified as a minority electron surface state, as well as two maxima around -0.5 eV are distinctive features. A kink at -0.6 eV for the 50 eV image originates from an iridium domain boundary where intensity and Sherman function obviously changes. For the asymmetry, the first positive peak at -0.1 eV is higher than the peak at -0.3 eV. Overall, we see the expected behavior. A band structure calculation is shown in figure 4.25 (b). As observed in the measurement, the two minority electron bands diverge for higher emission angles. However, a gap of 0.2 eV is not seen in the theory for normal emission.

Using the same configuration, the Fe/W(110) sample bias was varied to map a larger energy range and shift the Fermi edge through the detector image. The acquisition time of one image was 2 minutes. In total, 8 asymmetry images have been assembled to a large-scale asymmetry image covering 0 eV to -9 eV and ±9° (see figure 4.26). Line scans calculated from ±3.4° are plotted below. Again, the twin minority electron feature is visible right below the Fermi edge. Below the polarity change around -0.5 eV, the negative asymmetry becomes successively stronger until it reaches its maximum between -1.5 eV and -3 eV. It then decreases continuously to a value of -4% at -5.5 eV and stays relatively constant. The resulting line profile shows a very smooth transition between the measurements if only 1.0 eV or 1.5 eV of each measurement is used. It is remarkable that the individual profiles fit very well together. This means that the Sherman function hardly changes in an energy interval of at least ±0.5 eV for the employed imaging and scattering condition settings of $E_{kin} = 10$ eV and $\varphi = 15°$. This is as expected from the asymmetry map in figure 4.13.

To additionally map the angles along the $(\overline{\Gamma N})$ direction of the Fe/W(110) sample, it was rotated around the [001] axis. Angles from +4° to -20° in steps of 2° degrees were

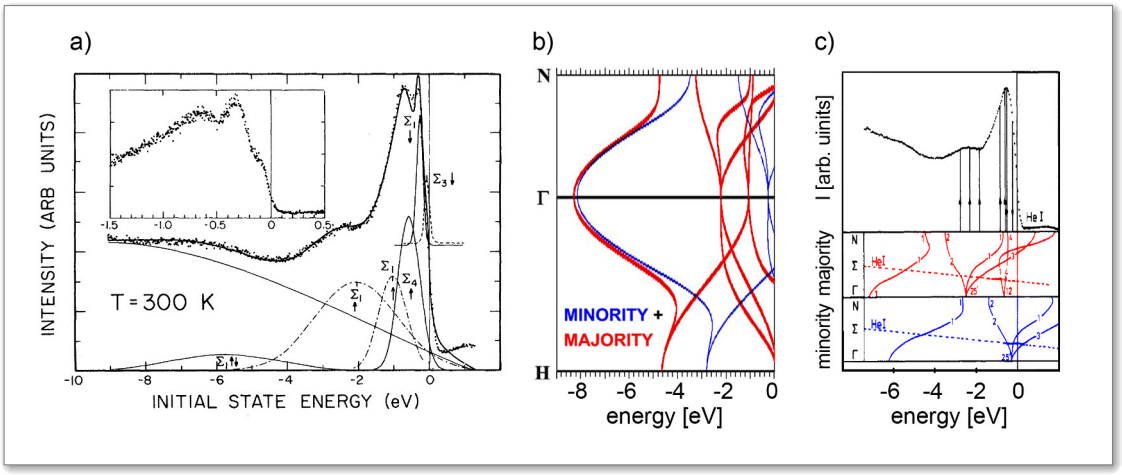

Figure 4.25: (a) Normal emission PES measurement of Fe(110) with peak compositions taken from [93]. (b) DFT-GGA band structure calculation for minority and majority electrons of Fe(110). Taken and modified from [77]. (c) Normal emission intensity profile of Fe(110) measured with a 21.2 eV He-I lamp. Contributions from direct transitions are marked by arrows (top). Band structure calculation for majority (red) and minority (blue). Crossing points with the shifted free electron parabola (dashed line) indicate possible direct transitions (bottom) (taken and modified from [81]).

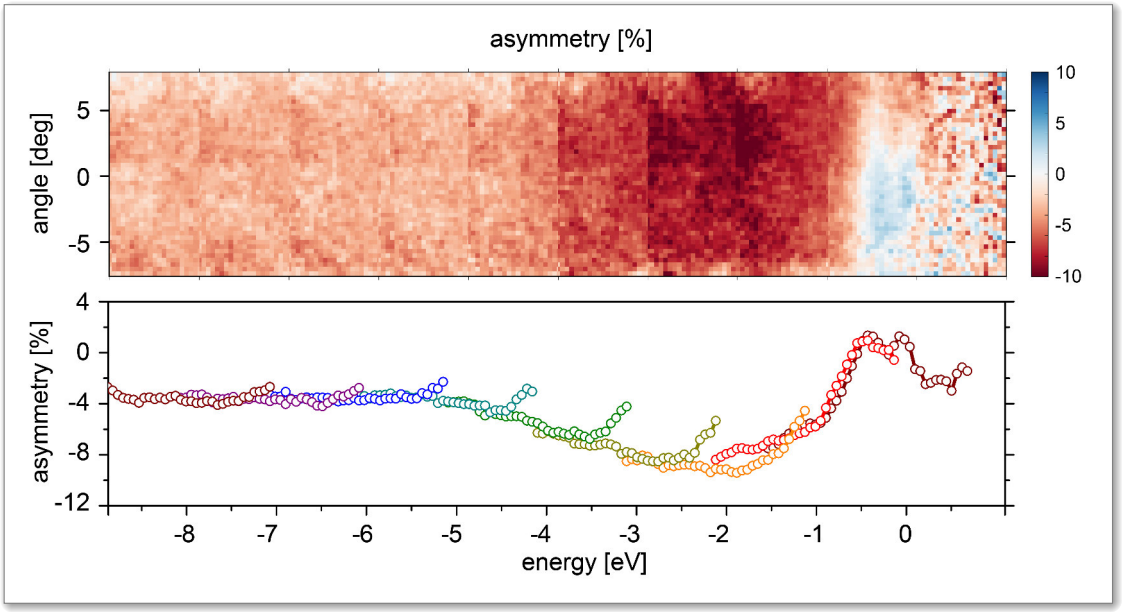

Figure 4.26: 8 SARPES images of Fe/W(110) along ($\overline{\Gamma H}$) are merged to one image (top). An asymmetry line scan was calculated from ±3.4° (bottom). Image boundaries are located at each eV between -9 eV and -3 eV and at -1.5 eV.

measured (see figure 4.27 (a)). Line scans averaged from ±3.4° were used to construct an image with the angular dispersive axis in the ($\overline{\Gamma N}$) direction (see figure 4.27 (b)). The acquisition time per image and magnetization direction was 1 minute. The in-plane spin polarization P_e was constantly aligned parallel to the rotation axis. A loss of the asymmetry signal to the power of cosine due to a spin component change with increasing rotation angle was therefore avoided.

The observed intensities for opposite magnetization directions clearly differ below the Fermi edge. The attenuation below -1 eV is caused by the limited scattering crystal dimension. The intensity drop for larger angles and higher binding energies and the calculated asymmetry is very similar to the ($\overline{\Gamma H}$) direction. The features in the ($\overline{\Gamma N}$) direction diverge slightly towards larger emission angles. The negative spin polarization of the lower feature is starting to become visible around -16° while the upper one appears around -6°.

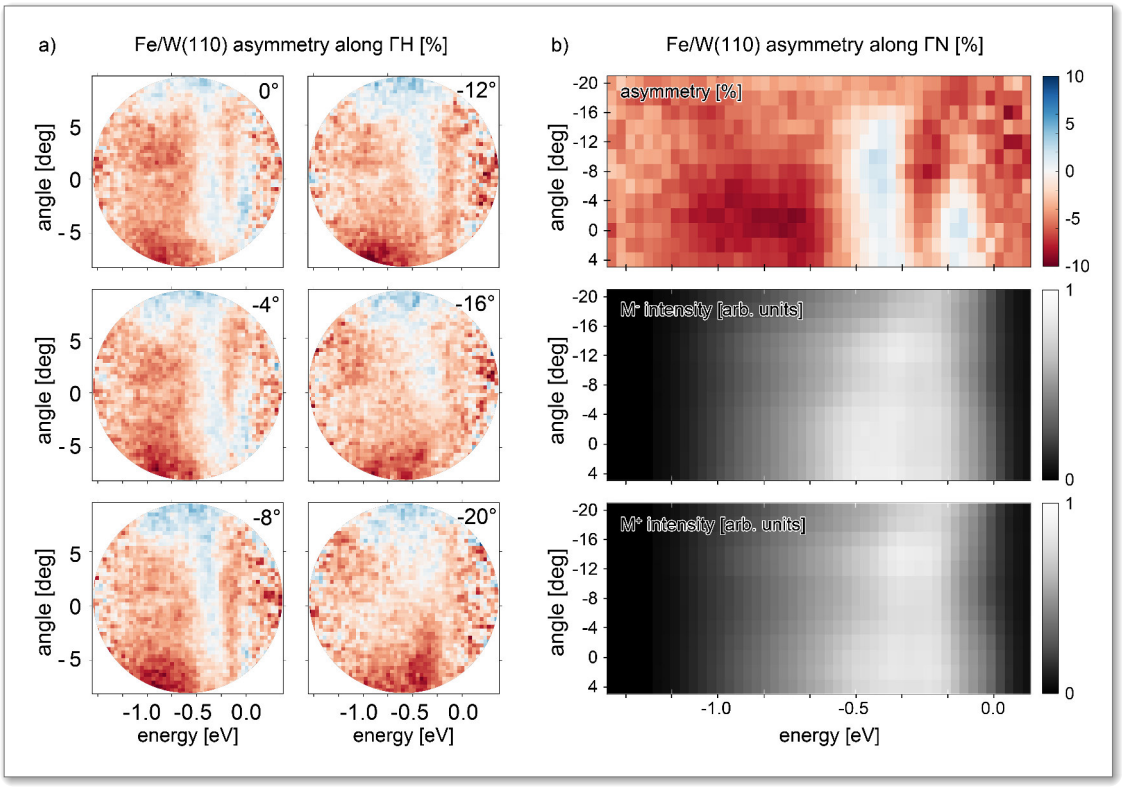

Figure 4.27: (a) Exemplary Fe/W(110) SARPES images along ($\overline{\Gamma H}$) for different sample tilts. (b) Calculated asymmetry images along ($\overline{\Gamma N}$) (top) and corresponding intensities for opposite sample magnetizations (bottom).

4.10 H_2TPP on Fe/W(110) with multichannel SARPES

The organic molecule tetraphenylporphyrine or H_2TPP ($C_{44}H_{30}N_4$) was deposited on 25 ML Fe/W(110) by using thermal evaporation from a crucible. The evaporator was

warmed up before starting the deposition of approximately $\frac{3}{4}$ of a monolayer. To determine the thickness, a calibration with a quartz micro balance was done. Although there is no ordered molecule growth, the crystalline H_2TPP layer-to-layer distance of 350 pm was assumed for this purpose. Combined with the usual density of 1.244 $\frac{g}{cm^3}$ and an AT-cut 10 MHz quartz crystal, a frequency change of 9.68 Hz was defined to be equivalent to one monolayer of H_2TPP.

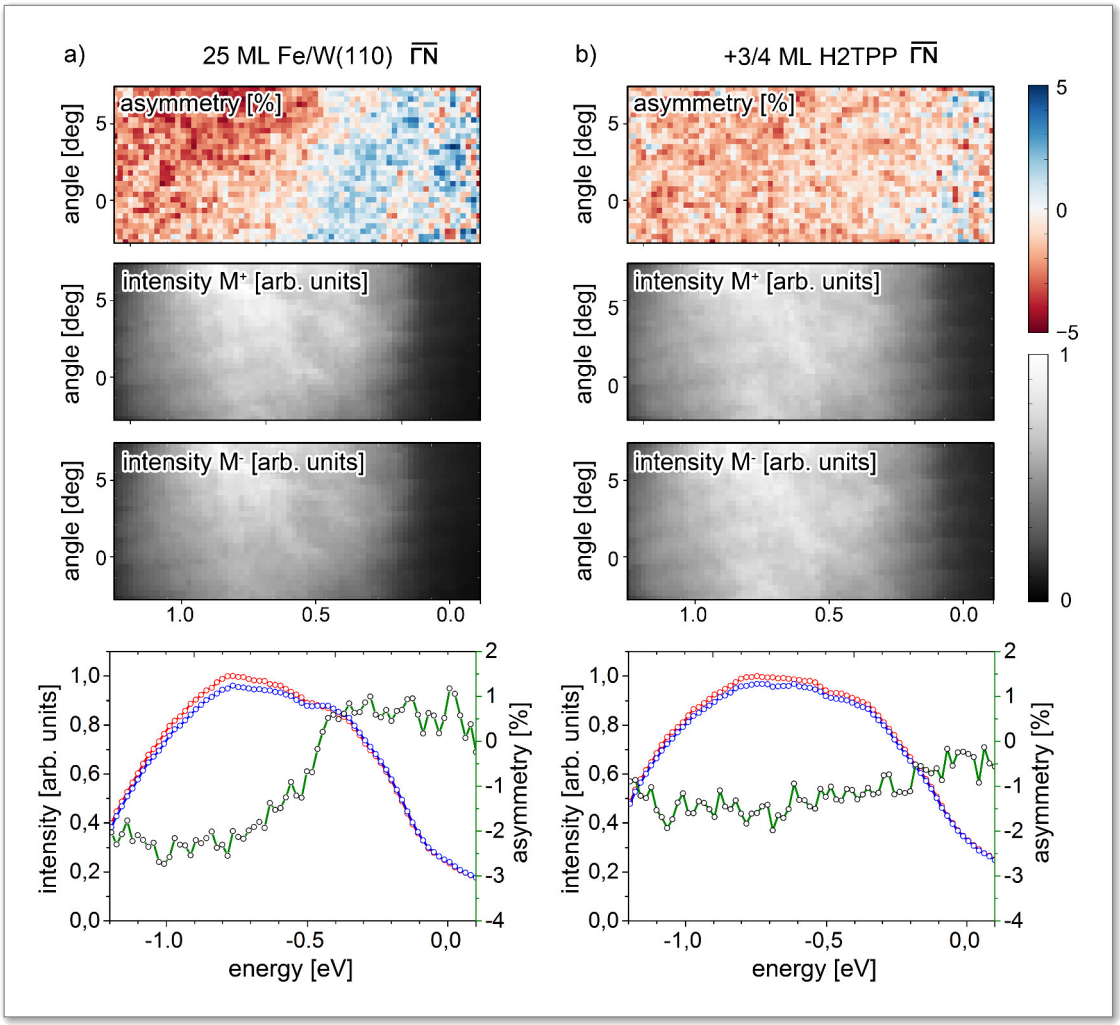

Figure 4.28: (a) Multichannel SARPES and intensity images and line scans of 25 ML Fe/W(110) along ($\overline{\Gamma H}$). (b) SARPES and intensity images and line profile of $\frac{3}{4}$ ML H_2TPP on 25 ML Fe/W(110) along ($\overline{\Gamma H}$)

A multichannel SARPES measurement of the 25 ML Fe/W(110) along with the angular dispersive axis along ($\overline{\Gamma H}$) was performed prior to the H_2TTP deposition. The result is shown in figure 4.28 (a). According to the asymmetry image, the quality of the iron film was not ideal. A polarization change around 0.5 eV is visible, but the pronounced double feature as seen before in figure 4.23 is not observed. Furthermore, with 0.5% at the positive feature and -2.5% below 0.5 eV the asymmetry signal is lower than observed

for an optimal Fe film. Compared to figure 4.24, the intensity profile is less characteristic. This is partly caused by the larger averaging window of -2.5 to 7.5°, over which the profile was generated. The poorer film quality was caused by a rough W(110) substrate surface and thus a less well ordered film growth. Electron-dispersive X-ray spectroscopy and the scanning electron microscope revealed small amounts of iron and a deformed surface. This indicated alloying processes and surface reconstructions [59, 69]. This assumption was fortified by a LEED measurements where the W(110) spots were more blurred than usual. LEED spots of Fe/W(110) were accordingly also relatively unsharp. This imperfect tungsten substrate was used only for this measurement series and could not be substituted to this time.
However, $\frac{3}{4}$ ML H_2TPP have been deposited onto the iron to analyze the effect of the molecules on the spectrum. The result is shown in figure 4.28 (b). With the deposited molecules, no dispersion or additional states are visible in the asymmetry and intensity images. The positive valence state polarization as observed in figure 4.23 is suppressed. The asymmetry profile changes from nearly 0% at E_F to -1.5% at 0.75 eV and is thus much smaller than prior to the molecule deposition.

4.11 SARPES at the Hiroshima Synchrotron Radiation Center

The ESPRESSO machine was used to measure spin-resolved photoemission spectra of the H_2TPP-Fe/W(110) interface. Different molecule layer thicknesses have been produced to analyze the influence of the interface. Some of the spectra shown here were evaluated and visualized using the KuroMacro and the InoMacro[2] for Igor Pro.

Spectra of Clean W(110)

The first ARPES measurements were dedicated to the clean tungsten substrate. The crystal was annealed in an oxygen atmosphere and flashed to 1800 °C. The LEED image was checked in advance and showed sharp spots. A momentum map and standard ARPES images with the angular dispersive axis along ($\overline{\Gamma H}$) and ($\overline{\Gamma N}$) were measured covering an energy range of up to 1.8 eV below the Fermi edge. The measurements were done with a He-VUV lamp ($h\nu = 21.2$ eV) and the results are shown in figure 4.29. For the momentum map, only three exemplary constant-energy cross sections are shown. Similar to [62] where separate measurements with p- and s-polarized light were done, the surface state S_2 (Σ_1 symmetry) and the anisotropic Dirac-cone-like surface state S_1 1.25 eV below E_F (mainly Σ_3 symmetry) can be clearly identified in the ($\overline{\Gamma H}$) and ($\overline{\Gamma N}$) ARPES image. High intensity bulk states around 1.5 eV below E_F and steep dispersions starting from the Fermi surface are additionally visible. The intensity imbalance in both ARPES images and in the ($\overline{\Gamma N}$) direction of the map is a result of the linear dichroism. In the -0.25 eV momentum image,

[2] Akihiro Ino, ino@hiroshima-u.ac.jp, Hiroshima Synchrotron Radiation Center, Hiroshima University, 2-313 Kagamiyama, Higashi-Hiroshima City

the surface state S_1 is visible at $(k_x, k_y) = (\pm 0.2,\ 0.0)$ Å^{-1}. In the k_y direction it is less pronounced. At -0.5 eV, it merges with the steep dispersion and creates a ring like structure. Its shape and size changes towards -0.75 eV.

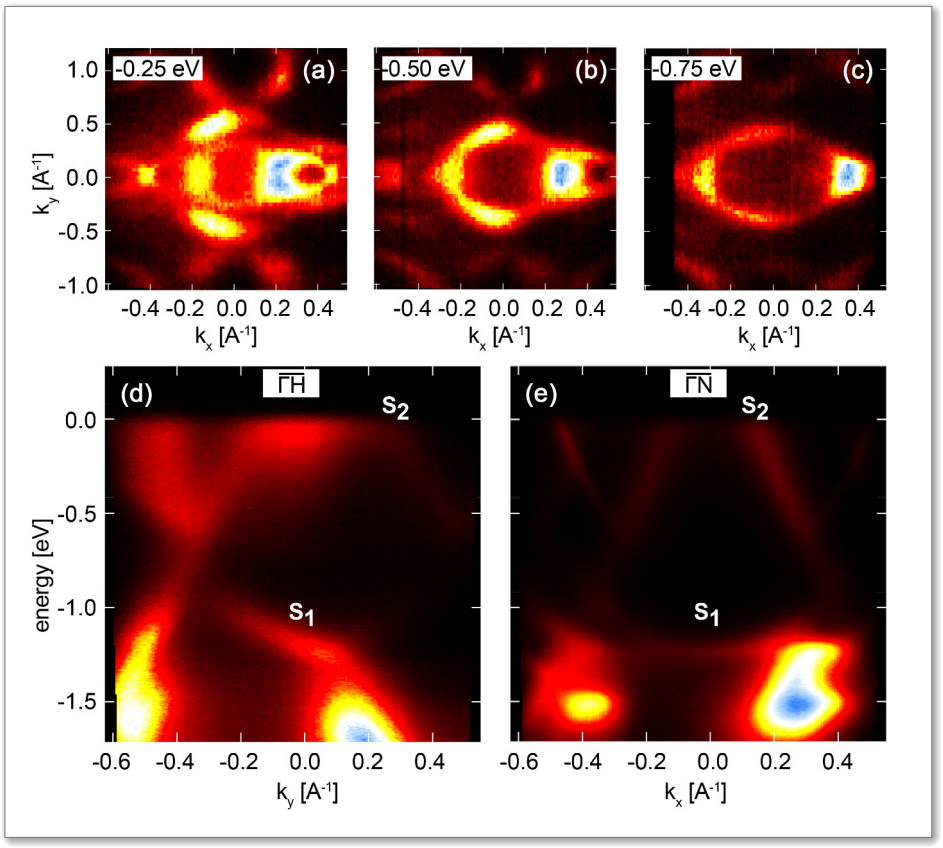

Figure 4.29: Momentum images of W(110) at energies of (a) -0.25 eV, (b) -0.50 eV and (c) -0.75 eV and cross sections with higher resolution (d) along ($\overline{\Gamma H}$) and (e) along ($\overline{\Gamma N}$). Each constant-energy momentum image was calculated from a 10 meV slab. The images were measured with the ESPRESSO experiment in Hiroshima using a He-VUV lamp ($h\nu = 21.2$ eV).

Fe Layers on W(110)

With an inhomogeneously covered Fe/W(110) sample, we have recorded the change of the spectrum with the angular dispersive axis along ($\overline{\Gamma N}$). The coverage ranges from $\theta \approx 7$ at the corner of the crystal to almost 0 towards the opposite corner. It was estimated by LEED images showing the typical speckle patterns as seen in [30]. Figure 4.30 shows spectra and the corresponding line scans around the $\overline{\Gamma}$-point. The acquisition time was not constant and the noise level is not representative for the absolute intensity change. Generally, the IMFP of the electrons will cause an intermixture of tungsten and iron features. For extremely low iron coverages below 1 ML, the first spectrum shows that the background intensity clearly increases (see figure 4.30 (a)). Except of the extreme

borders, the background intensity is slightly stronger on the right side. As expected, the previously observed tungsten surface states S_1 and S_2 are quenched. Only the steep dispersion starting at the Fermi surface and the high-intensity bulk features at -1.5 eV is still visible. The intensity at -0.4 $Å^{-1}$ and -1.5 eV is higher compared to the intensity on the opposite site. The latter point has also shifted its center from originally 0.3 to 0.2 $Å^{-1}$. Spectrum (b) shows the sample with a larger iron coverage of few monolayers. The steep dispersion features almost disappear in the high intensity caused by the iron. At the $\overline{\Gamma}$-point, the higher bulk feature intensity of tungsten around -1.5 eV has also diminished as seen in the line scan. Especially the intensity near the Fermi edge strongly rises and shows two off-center peak regions around -0.25 and -0.75 eV. In the line scan, a weak shoulder at -0.1 eV has appeared, as already observed in figure 4.24. With a coverage of 7 molecular layers (see figure 4.30 (c)), the intensity around -1.5 eV has further dropped and the typical iron intensity distribution is obtained. The intermediate minimum at 0.5 eV is now clearly pronounced.

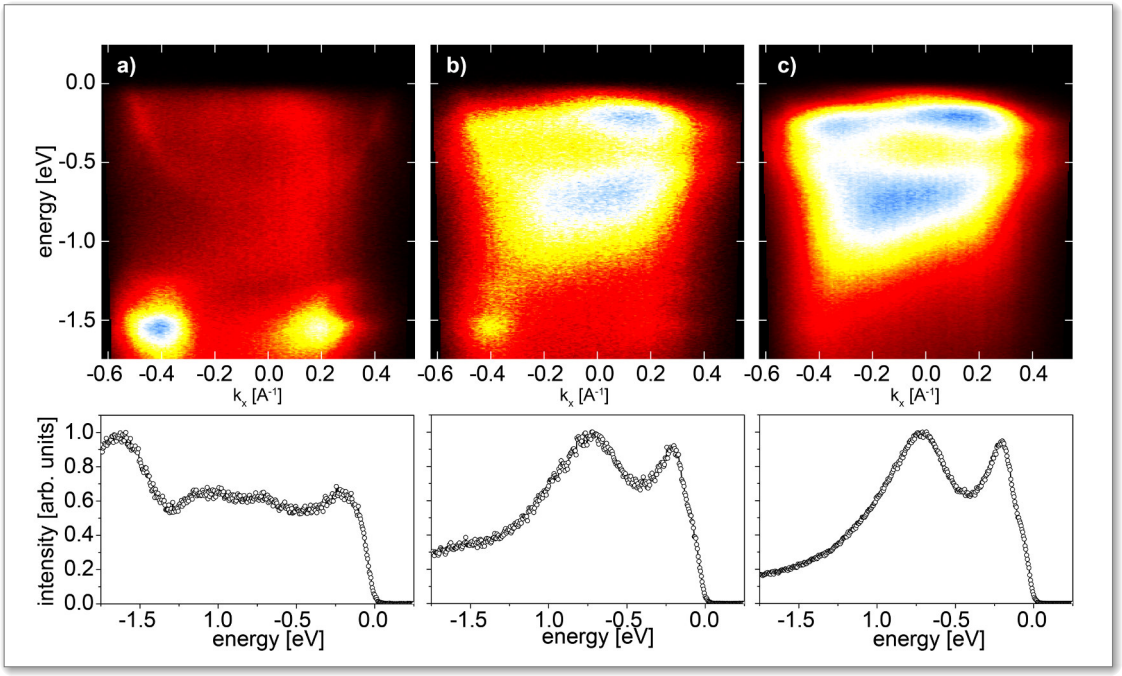

Figure 4.30: ARPES spectra of Fe/W(110) (a) with extremely low coverage under 1 ML, (b) with few ML coverage and (c) with $\theta \approx 7$ ML. The corresponding line profiles are shown below and calculated from $\pm 0.7°$ at the $\overline{\Gamma}$-point. The data was measured in Hiroshima.

Spectra of 15 ML Fe/W(110)

Similar to the bare tungsten crystal, a momentum map and ARPES images with the angular dispersive axis along ($\overline{\Gamma H}$) and ($\overline{\Gamma N}$) has been measured for 15 ML Fe/W(110). The results are shown in figure 4.31. The exemplary constant-energy momentum maps

show a high intensity around the $\overline{\Gamma}$-point. The circular shape of the high-intensity at -0.20 eV changes to a cross-shaped intensity distribution towards -0.75 eV. An intermediate intensity minimum is found at the $\overline{\Gamma}$-point around -0.50 eV. This behavior is also reflected in the ($\overline{\Gamma H}$) and ($\overline{\Gamma N}$) cross sections below and the line profile of figure 4.30. Here, the overall imbalance in the intensity is again a result of the VUV-light angle of incidence. The shape of the high intensity region in the ($\overline{\Gamma H}$) direction is drop shaped according to the not shown cross sections of the momentum map data. A separated minority electron surface state S right below the the Fermi edge with a relatively low intensity can be seen in both directions around the $\overline{\Gamma}$-point. The width of this surface state along the $\overline{\Gamma N}$-direction is significantly larger. In the momentum map data, a band around $k_y = \pm 0.6$ Å^{-1} and a band around $k_y = \pm 1.2$ Å^{-1} fits to the majority and minority band structures at the Fermi edge from the DFT calculation in figure 4.25. Towards higher binding energies, both bands move to the center and merge with the high intensity.

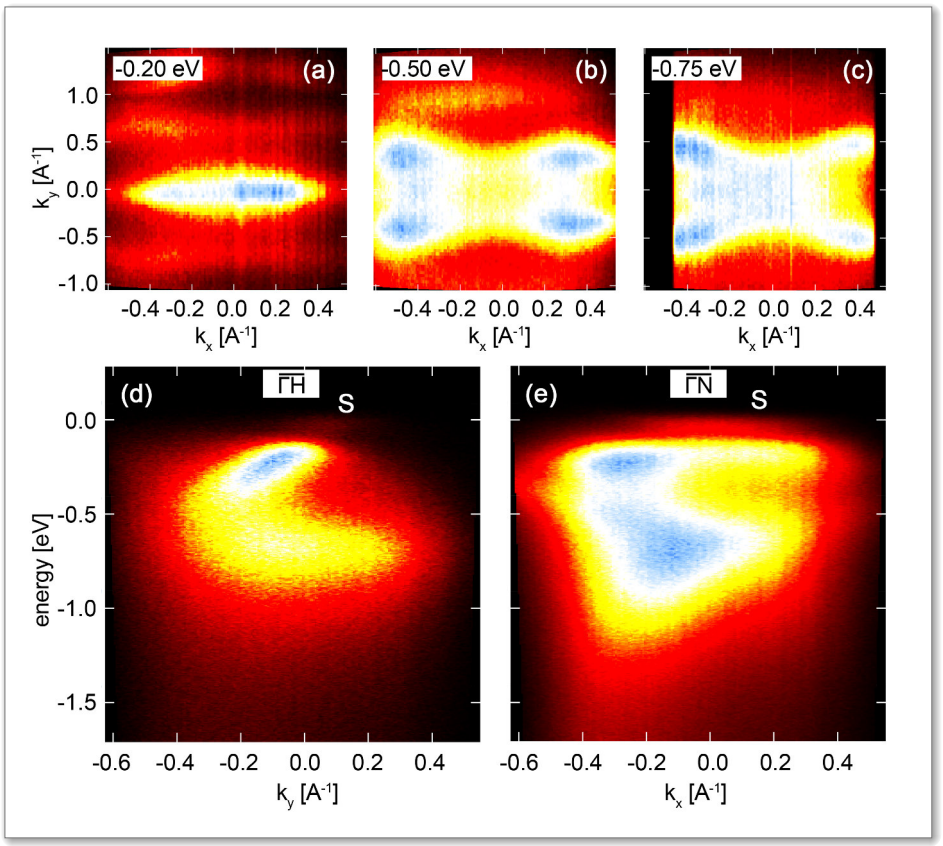

Figure 4.31: Momentum images of 15 ML Fe/W(110) at energies of (a) -0.20 eV, (b) -0.50 eV and (c) -0.75 eV and cross sections with higher resolution (d) along ($\overline{\Gamma H}$) and (e) along ($\overline{\Gamma N}$). Each constant-energy momentum image was calculated from a 10 meV slab. The spectra was measured in Hiroshima.

Fermi Surface

A comparison of the measured Fermi surfaces of clean tungsten and 15 ML Fe/W(110) to results from references [73, 77] is shown in figure 4.32. The measured Fermi surfaces were symmetrized with respect to both mirror axes to eliminate intensity imbalances from the linear dichroism due to the VUV light angle of incidence. Except for the intensity distribution around the $\overline{\Gamma}$-point, the tungsten Fermi surfaces are relatively similar (figure 4.32 (a), (c)). Two branches along the [001] direction are clearly reproduced. For the iron film, the measured structures are more diffuse. The measured intensity around the $\overline{\Gamma}$-point (figure 4.32 (b)) does not clearly show the oval structure (figure 4.32 (d)). Also the outer bands are located at slightly different positions. The deviations seen for tungsten and iron are attributed to the different excitation energies of 100 eV and 139 eV and the use of a standard VUV lamp instead of a synchrotron light source.

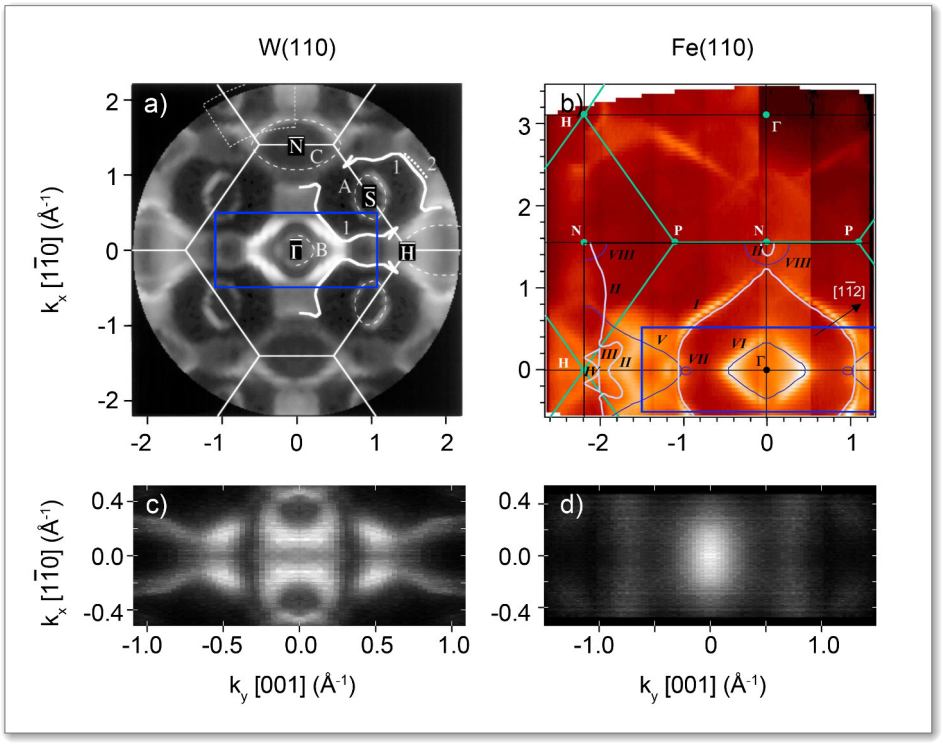

Figure 4.32: (a) Fermi surface of W(110) with $h\nu$ = 100 eV [73] and (b) of Fe(110) with $h\nu$ = 139 eV [77]. Symmetrized measured intensities of the Fermi level intensities of (c) W(110) and (d) 15 ML Fe/W(110) with $h\nu$ = 21.2 eV measured in Hiroshima. The blue rectangles in (a) and (b) mark the measured area of (c) and (d).

H_2TPP on Fe/W(110)

Following the tungsten and iron characterization, a first measurement series of different H_2TPP coverages on 15 ML Fe/W(110) was carried out. The H_2TPP molecules

were deposited using a thermal evaporator with a rate of 3.2 $\frac{ML}{h}$. The rate was checked with a quartz microbalance before and after the deposition (2.46$\frac{Hz}{ML}$ for 5 MHz AT-cut quartz crystal and C_f=56.6$Hz\frac{cm^2}{\mu g}$). The pressure in the preparation chamber was around $1 \cdot 10^{-9}$ mbar during the evaporation. A constant pressure served as an indicator for a constant deposition rate. In each measurement series, different layer thicknesses were produced by consecutively depositing the molecules. The evaporator was usually left on the deposition settings to avoid warm-up periods between the photoemission experiments. A cleaning of the Fe/W(110) substrate from H_2TPP by simply heating the sample was unfortunately not successful. Around 200°C, a hazy film started to become visible at the curved coverage border of the iron film (checked by LEED) and slowly covered the whole sample (see figure 4.33 (a) and (b)). After another 5 minutes at 230°C, the Fe/W(110) substrate was shiny. Further heating to 300°C did not change anything visually (see figure 4.33 (c)). The resulting LEED spots were relatively weak and a high background intensity was present. A simple high-power flash resulted in sharp LEED spots showing a strong carbon contamination so that an annealing under oxygen atmosphere was necessary to obtain a clean tungsten surface again.

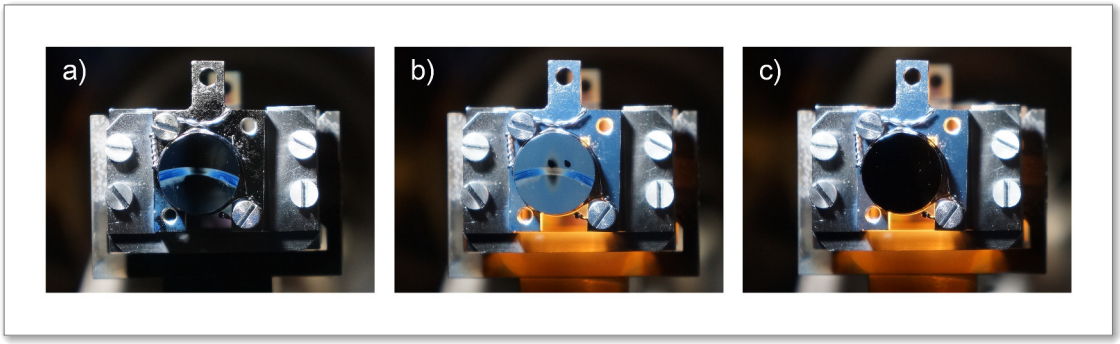

Figure 4.33: A half-covered Fe/W(110) sample was heated to 200°C (a), held at 230°C (b) and heated up to 300°C (c). The curved line on the sample is the border of the iron film. This was confirmed by several LEED measurements along a line perpendicular to the iron border.

A properly prepared Fe/W substrate showed a carbon and oxygen-free LEED pattern. The fabricated metal-organic interfaces were analyzed by LEED, Auger spectroscopy (see figure 4.34) and photoemission spectroscopy before evaporating the next molecules on top of the sample. Spin-integrated and spin-resolved photoemission spectra of H_2TPP films with thicknesses of 0.87 ML and 1.74 ML as well as the bare 15 ML Fe/W(110) substrate are shown in figure 4.35.

The Auger spectroscopy of the H_2TPP-iron interface shows several peaks (see figure 4.34 (a) and (c)) that can be assigned to literature values of carbon (270 eV), nitrogen (380 eV), oxygen (510 eV) and iron (600 eV, 654 eV, 705 eV). The measured peak position are located marginally below the literature values probably due to calibration errors. The nitrogen

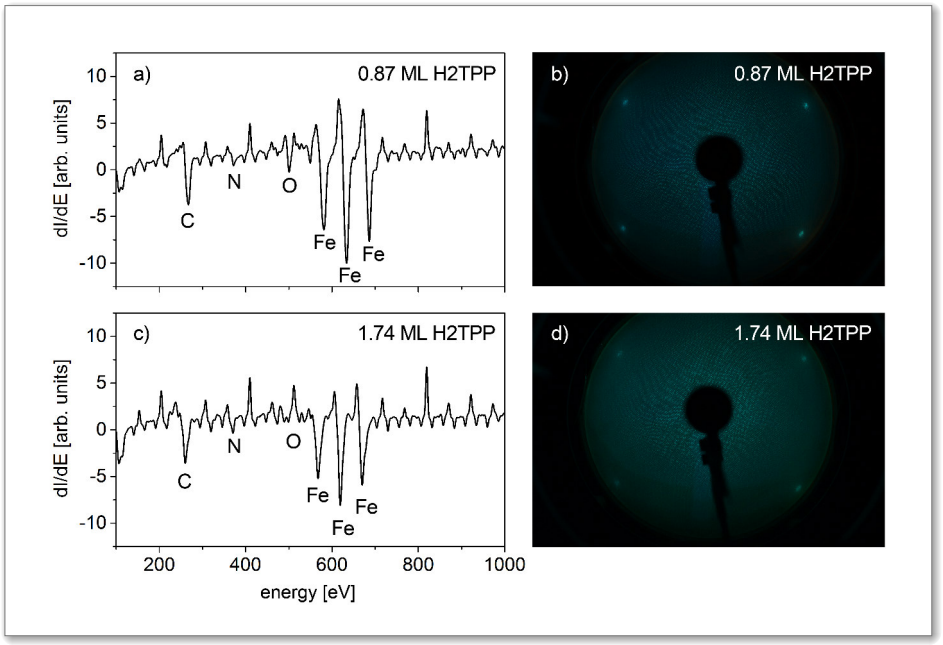

Figure 4.34: (a)(c) Auger electron spectroscopy and LEED images at 115 eV of 0.87 ML H_2TPP on 15 ML Fe/W(110) (b) and (d) 1.74 ML H_2TPP on 15 ML Fe/W(110).

and carbon peaks originate from the organic molecule. Surface contaminations from residual gas atoms further contribute to the carbon peak and induce the oxygen peak. Further peaks around 210 eV, 410 eV and 820 eV cannot be clearly identified. The comparison between the spectrum of 0.87 ML and 1.74 ML reveals an iron signal decrease of approximately 20% which is obviously a consequence of the molecule coverage. Furthermore, the oxygen peak is differently pronounced. The other peaks remain surprisingly unchanged. For both molecule coverages, the LEED images still show the iron pattern. The relatively high background intensity originates from the arbitrarily oriented H_2TPP molecules. It rises with increasing H_2TPP thickness, while the iron pattern intensity decreases (see figure 4.34 (b) and (d)).

In the ARPES images in figure 4.35 (a)(d)(g), a decreased intensity of the iron features is clearly visibly with increasing H_2TPP coverage. For 1.74 ML H_2TPP, the iron features have mostly vanished. The slope of the intensity at the Fermi edge has additionally decreased. The minority electron surface state 0.1 eV below the Fermi edge disappears already for 0.87 ML of H_2TPP and the intensity becomes less dependent on the emission angle. Accordingly, the surface state shoulder at -0.1 eV also disappears in the $\overline{\Gamma}$-point intensity line scans and also the peak at -0.25 eV is significantly suppressed. Generally, the profile becomes more flat and smooth (see figure 4.35 (b)(e)(h)). The absolute intensity decreases significantly. Attenuation values for the absolute intensity could not be determined due to variations of the VUV lamp intensity that had to be switched off and restarted between the measurements.

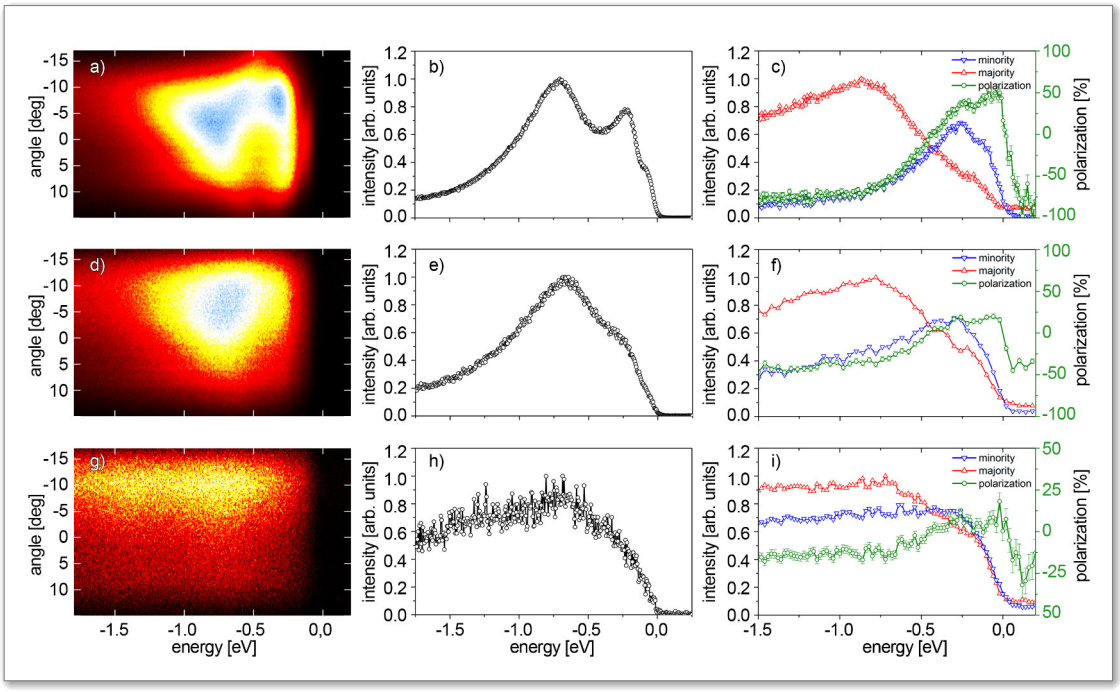

Figure 4.35: ARPES images along ($\overline{\Gamma N}$), relative intensities at the $\overline{\Gamma}$-point (averaged over $\pm 0.7°$ and spin polarization with relative minority (blue) and majority (red) electron intensities for 15 ML Fe/W(110) (a)-(c), 0.87 ML H_2TPP on 15 ML Fe/W(110) (d)-(f) and 1.74 ML H_2TPP on 15 ML Fe/W(110) (g)-(i) measured in Hiroshima.

The intensity line profiles at the $\overline{\Gamma}$-point for the spin-integrated ARPES setup are shown in figure 4.35 (b)(e)(h). Spin-resolved line profiles at the $\overline{\Gamma}$-point are shown in (c)(f)(i). The polarization was calculated by assuming a Sherman function of 0.3 for the VLEED-based spin detector (see equation (4.8)). Deviations of the majority and minority electron intensity sum to the spin-integrated ARPES intensity profiles as well as background intensity differences are attributed to the scattering procedure at the spin filter. A set of four successively measured intensity profiles (I^-, I^+, I^+, I^-) was used to calculate the spin polarization:

$$P = \frac{I^{\uparrow} - I^{\downarrow}}{I^{\uparrow} + I^{\downarrow}} = \frac{1}{S}\frac{I^{+} - I^{-}}{I^{+} + I^{-}}, \qquad \text{with } I^{+} + I^{-} = I^{\uparrow} + I^{\downarrow}. \tag{4.8}$$

Together with an intensity calibration procedure, a reliable spin polarization profile was calculated for all measurements. Instead of showing the measured intensities I^+ and I^- for the different spin-detector magnetizations, the calculated intensities $I^{\uparrow}$ and $I^{\downarrow}$ of the majority and minority electrons are plotted in the diagrams. The majority and minority

electron intensities were calculated by the following equations:

$$I^{\uparrow} = \frac{1}{2}\left[\left(\frac{1}{S}+1\right)I^{+} - \left(\frac{1}{S}-1\right)I^{-}\right], \tag{4.9}$$

$$I^{\downarrow} = \frac{1}{2}\left[\left(\frac{1}{S}+1\right)I^{-} - \left(\frac{1}{S}-1\right)I^{+}\right]. \tag{4.10}$$

Here, variations of the film thickness dependent features are better visible because the partial superposition of minority and majority electron intensities as seen in the raw intensities I^{+} and I^{-} is eliminated.

Figure 4.35 (c) shows two polarization maxima with values of up to 55% and 40% around -0.05 eV and -0.25 eV for the clean 15 ML Fe/W(110). Compared to section 4.9, the energy values are shifted by 0.05 eV due to a different E_F reference position. The intensity of the minority electrons show the corresponding double peak structure and a steep intensity increase compared to the majority electron intensity. Below -0.25 eV, the intensity decreases from 0.6 arbitrary units exponentially and reaches a value of under 0.15 arbitrary units at -1.0 eV. Here the polarization remains approximately constant with -75%. The majority electron intensity shows a small hump at -0.2 eV with an intensity of 0.3 arbitrary units and the global maximum at -0.8 eV. Below that, the intesity decreases linearly.

For 0.87 ML H_2TPP, figure 4.35 (f) reveals a much smaller polarization at the Fermi edge. The peak values around -0.05 eV and -0.25 eV have decreased to roughly 20% and 19%. An intermediate minimum between these peaks is hardly pronounced. The spin-polarized surface state is obviously quenched which is also illustrated by the disappearance of the minority electron intensity shoulder at -0.05 eV. Below -0.25 eV, the minority electron intensity decreases now rather linear and equals 0.3 at -1.5 eV. Here, the polarization settles between -40% and -45%. The spectral weight of the majority electrons is enhanced from 0 eV to -0.75 eV so that the hump at -0.2 eV reaches almost 0.5 arbitrary units.

For 1.74 ML H_2TPP (see figure 4.35 (i)), the positive polarization below the Fermi edge is around 0-5%. Towards -0.75 eV, it changes slowly to -15% and stays constant. The spectral weight of minority and majority electrons has increased significantly below -0.75 eV. The minority electron intensity rises to 0.75 arbitrary units and shows no pronounced structures and decreases monotoneously with increasing binding energy. The majority electron intensity rises to 0.95-1.00 arbitrary units towards -0.75 eV and decreases also slowly. Only a kink in the slope at 0.2 eV remains from the former hump position.

Finally, an ARPES image of >10 ML H_2TPP was measured. The precise thickness is unknown because the deposition rate increased exponentially during the evaporation due to an insufficient warm-up time. The rate before and after the deposition of 24 minutes was 5.7 $\frac{ML}{h}$ and 67,1 $\frac{ML}{h}$. The resulting sample did not suffer from charging. The result is seen in figure 4.36 together with an intensity line scan at the $\overline{\Gamma}$-point. In contrast to lower molecule coverages, the absolute intensity has decreased and the first significant signal is seen around -2.0 eV. It belongs to the highest occupied molecule orbital (HOMO) of the

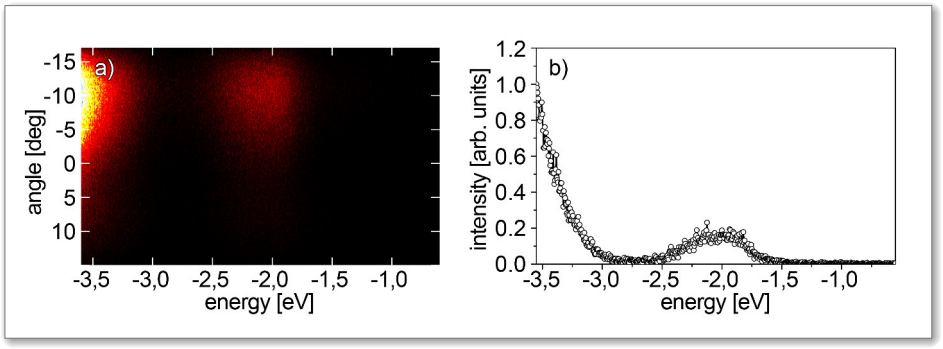

Figure 4.36: (a) ARPES image along ($\overline{\Gamma N}$) of >10ML H2TPP on 15 ML Fe/W(110) along ($\overline{\Gamma N}$) and corresponding line profile at the $\overline{\Gamma}$-point calculated from $\pm 0.7°$ and measured in Hiroshima.

H_2TPP. A second intensity signal is found with a peak position somewhere below -3.5 eV. For a 50 nm thick H_2TPP layer on oxide/Si(100), the HOMO is found at -2.5 eV (from a_{1u} and a_{2u} π orbital) and -4.5 eV (from π orbitals) as reported by [63]. They can be assigned to the measured peak positions. The discrepancy is probably caused by a different work function or an interface dipole formation effect.

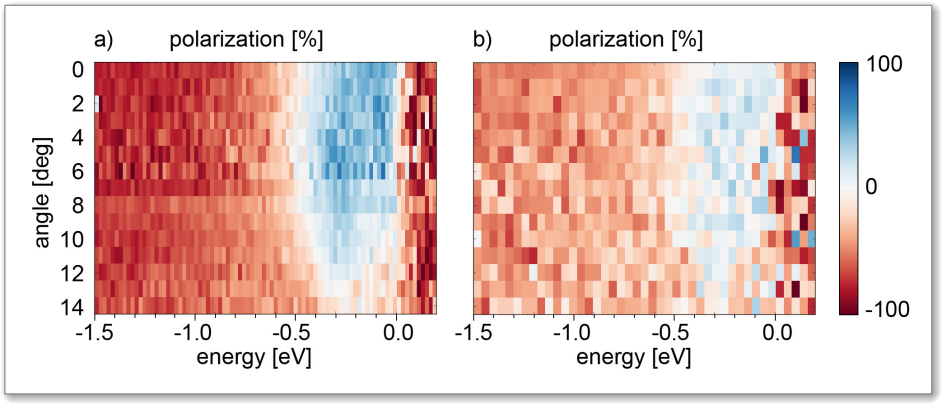

Figure 4.37: (a) SARPES image of 15 ML Fe/WW(110) along ($\overline{\Gamma N}$) and (b) for and additional 0.87 ML H2TPP film on 15 ML Fe/W(110). The sample was tilted to cover emission angles from 0° to 14°.

To compare not only the $\overline{\Gamma}$-point evolution upon H_2TPP deposition, a SARPES image was measured for 15 ML Fe/W(110) and for 0.87 ML H_2TPP on 15 ML Fe/W(110). The result is shown in figure 4.37. It shows an area of 1.5 eV and emission angles from 0-14°. Differences in the signal to noise ratio originates from different VUV lamp intensities. The SARPES image of iron resembles the results from section 4.9. The positive spin polarization at -0.1 eV and -0.3 eV ranges up to 10 and 13 degree but they are not as clearly separated as seen before. With 0.87 ML H_2TPP the overall polarization decreases and

only one large area with positive polarization is left. The dimension can be described as virtually unchanged.

H_2TPP on Fe/W(110)-c(2x2)O

In a second measurement series, different H_2TPP coverages on 15 ML Fe/W(110)-c(2x2)O were analyzed. The oxygen exposure is unknown since the superstructure formation was a side effect of residual oxygen presence during the iron film annealing at up to 600 K. The LEED image of the annealed iron film showed a clear c(2x2) superstructure (see figure 4.38 (b)). The corresponding Auger spectroscopy analysis in figure 4.38 (a) shows the three characteristic iron peaks. A strong peak around 500 eV is attributed to the oxygen. Carbon is virtually absent in the spectrum. H_2TPP was subsequently deposited with a rate of 1.0 $\frac{ML}{h}$. The c(2x2) superstructure in the LEED pattern vanishes surprisingly already for a coverage of 0.25 ML H_2TPP (see figure 4.38 (c)). This behavior was also observed in another independent measurement series. The signal of iron and oxygen drops significantly. For 0.50 ML, the background intensity increases in relation to the iron spot intensity. Compared to 0.25 ML, the iron and nitrogen signal stay nearly unchanged. The carbon and nitrogen peak increases as a result of the molecule coverage.
Looking at the angle-resolved photoemission spectra of 15 ML Fe/W(110)-c(2x2)O, the line profile at the $\overline{\Gamma}$-point and the polarization with minority and majority electron intensities in figure 4.39 (a)-(c), the result is very similar to the clean iron shown in figure 4.35 (a)-(c). Only the relative intensity peak heights at -0.10 eV and -0.25 eV in the $\overline{\Gamma}$-point profile are significantly lower in comparison to -0.75 eV. This is in accordance to results reported in reference [44]. The line profile shape remains mostly unchanged for the assumed low oxygen exposure. Additional spin-polarized features or significant variations should emerge only at higher binding energies or higher emission angles and higher oxygen exposures [101]. The spin polarization of the double peak structure below the Fermi edge is higher with 75% and 49%. However, the negative polarization below -1.0 eV reaches only values around -60%. A systematic error responsible for a polarization bias is therefore likely. Nevertheless, the shape of the profiles are untouched from this error. The remaining differences can be attributed to variations in the sample quality.
With the adsorption of 0.25 ML H_2TPP, the spectrum becomes more blurred as expected. The double peak intensity structure is still visible but becomes less pronounced in the $\overline{\Gamma}$-point profile. The spectral weight at -0.2 eV has decreased and the intensity dropped from 0.75 to 0.65 arbitrary units. At -1.75 eV, it has increased slightly. This is also reflected in the minority electron intensity. In relation to the minority electron intensity, the majority electron intensity has gained weight. The hump at -0.2 eV becomes again more pronounced. Below the Fermi edge, peak values of 62% and 39% are measured for the double structure. Towards -1.5 eV, the spin polarization is around -50%.
With a total film thickness of 0.50 ML, the described tendency continues. The intermediate intensity minimum in the $\overline{\Gamma}$-point profile at -0.4 eV has disappeared now. At -1.75 eV,

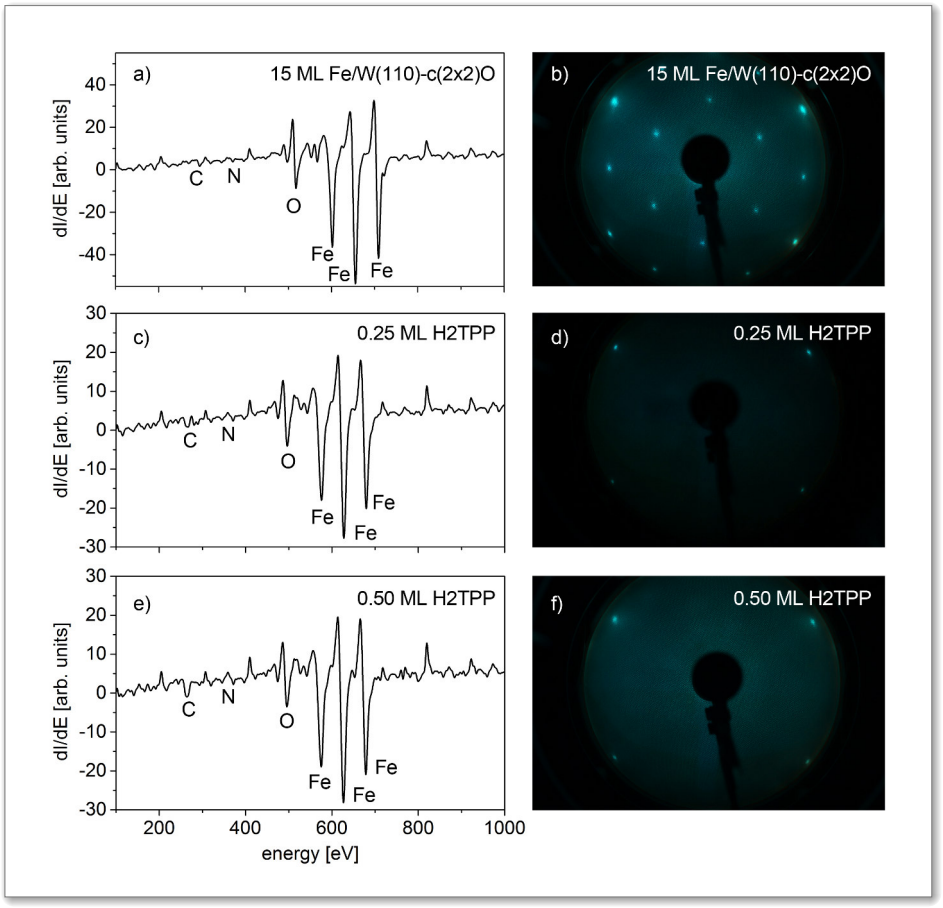

Figure 4.38: (a)(c) Auger electron spectroscopy and LEED images at 100 eV of 15 ML Fe/W(110)-c(2x2)O, (b)(d) with 0.25 ML H_2TPP deposited and (e)(f) with 0.50 ML H_2TPPdeposited. Total intensity variations in the LEED images originate from exposure and filament current differences.

the intensity reaches 0.2 arbitrary units. The polarization at -1.5 eV is approximately -50%. The double peak structure below the Fermi edge possess now polarizations of 49% and 29%.

Despite the fact that the second measurement series was measured with an oxygen covered sample, the behavior is similar to the first series without oxygen. Overall, the second series fits qualitatively between the clean iron film and 0.87 ML H2TPP on Fe/W(110). According to the results, the absorption of H_2TPP suppresses the spin polarization of the iron. The spin-polarized minority electron surface state is quenched between 0.50 ML and 0.87 ML H_2TPP. With increasing H_2TPP film thickness, the positive polarization below the Fermi edge decreases faster than the negative polarization below -0.5 eV. Characteristic features from iron are strongly blurred, damped and finally suppressed. The reduced spin polarization is probably a consequence of the electrical resistance difference, which limits the spin-injection efficiency. This is known as the impedance-mismatch problem [78]. Further spin relaxation mechanisms were already described in subsection 2.4.1.

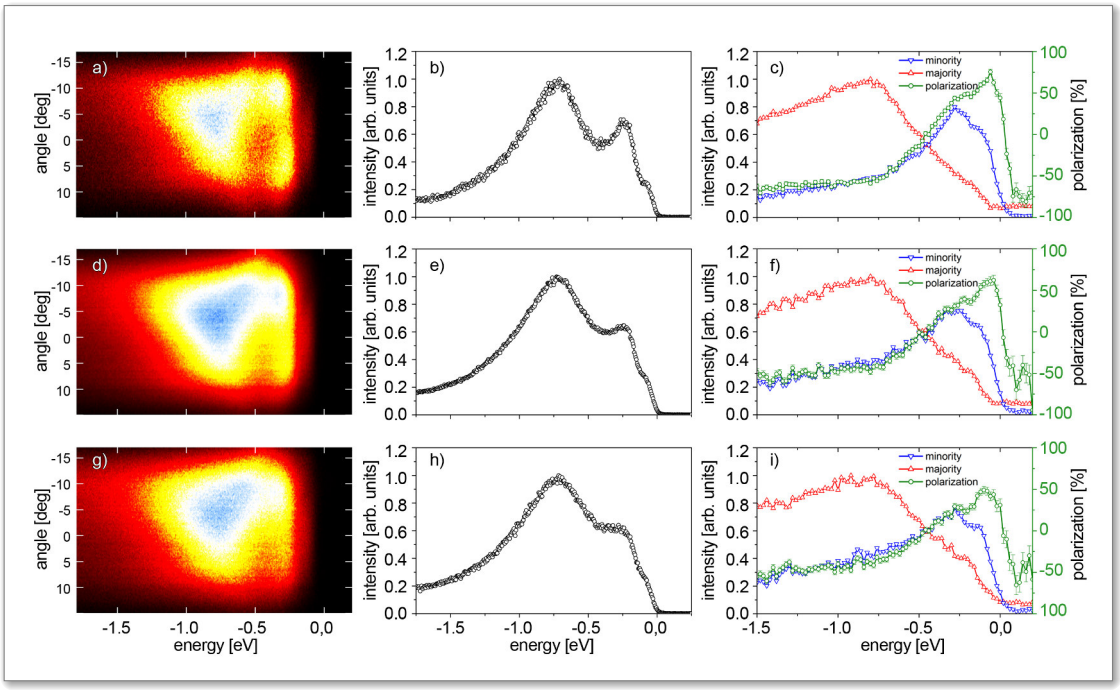

Figure 4.39: ARPES images along ($\overline{\Gamma N}$), relative intensities at the Γ-point (averaged over ±0.7° and spin polarization with relative minority (blue) and majority (red) electron intensities for 15 ML Fe/W(110)-c(2x2)O (a)-(c), 0.25 ML H_2TPP on 15 ML Fe/W(110)-c(2x2)O (d)-(f) and 0.50 ML H_2TPP on 15 ML Fe/W(110)-c(2x2)O (g)-(i). The spectra were measured in Hiroshima.

It is important to keep in mind that all spectra show a superposition of the iron film, the H_2TPP and possible hybrid interface states (HIS). For an excitation energy of 21.2 eV, the inelastic mean free path is 4.7 Å (for organic compounds) and 5.7 Å (for metallic elements) according to the universal curve from reference [82]. Moreover, the spin polarization at the non-planar H_2TPP molecule is locally varying. For CoPc on Fe for example, an amplification and inversion of the spin polarization is locally observed [13]. In the case of H_2TPP on Fe/W(110), the molecule-substrate interface states should not show any dispersion due to the arbitrary molecule orientation. According to figure 4.36, no bulk states of H_2TPP spectra are present near the Fermi edge. With increasing H_2TPP thickness, photoemission contributions of the iron substrate and the interface are reduced while the contribution of the bulk H_2TPP is increased. In the measured intensity profiles, only a broadening of peaks but not shifts or additional peaks are observed. The individual majority and minority electron intensities show a more varied behavior dependent on spin and binding energy. HIS as a consequence of partial charge-transfer, screening by the metal, Pauli push-back or bond formations [85] can be uniquely identified as a deviation from the iron spectrum (see e.g. [60]). In contrast to the used CoPc molecule with magnetic central ion in reference [13], the non-magnetic central ion of the CuPc from reference [60] resulted already in an energy-independent reduction of the spin polarization. HIS can

therefore only originate from the ring ligand π-electrons. Due to the missing central ion, HIS originating from a hybridization of π-molecular orbitals and iron d-states according to the $P_z - d$ Zener exchange mechanism [2], for example, cannot be seen here.

Spin Diffusion Length

To analyze the spin-transport properties, the relative spin polarization values at characteristic energy points were plotted against the molecule layer thickness. After the spin-injection from the iron film into the molecule layer, the polarization decreases with increasing molecule thickness. The characteristic spin diffusion length λ_d was determined by fitting an exponential curve ($y = e^{-x/\lambda_d}$) into the data points.

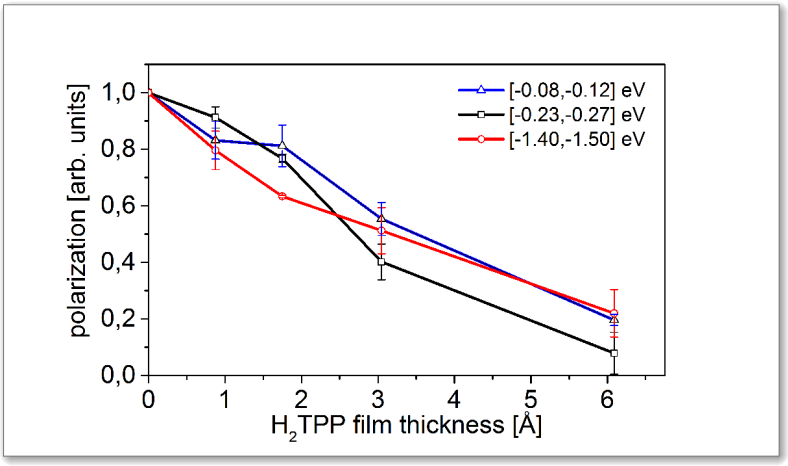

Figure 4.40: Average spin polarization values calculated for three different energy intervals of characteristic points. The intervals are [-0.08,-0.12] eV (black line), [-0.23,-0.27] eV (red line) and [-1.40,-1.50] eV (blue line) of the data shown in figure 4.39 (c), (f) and (i) are plotted against the H_2TPP layer thickness. The variation in the value errors originates from different statistics. The curve of the different exponential fits is omitted for clarity.

To enhance the accuracy of the spin diffusion length determination, polarization values were calculated by averaging over a small energy range od 0.05 eV. Furthermore, the results of the first and second measurement series were used together and plotted in one diagram since no remarkable difference in the behavior evinced from the data. Additionally, the polarization values were normalized by the values of the iron measurements without deposited molecules. This was needed, since the initial iron polarization values between the two measurement series were unequal probably due to a different iron surface quality. The considered energies were located at the two positive peaks energies below the Fermi edge (-0.1 eV and -0.25 eV) and at the negative end of the recorded spectrum (-1.45 eV). The results in dependency of the H_2TPP thickness in Å are shown in figure 4.40. The two

measurement series fit qualitatively. The calculated spin diffusion lengths according to the fit parameter λ_d are 3.85±0.74 Å (for -0.1 eV), 4.13±0.14 Å (for -0.25 eV) and 4.90±0.63 Å (for -1.45 eV). The resulting values are relatively close to each other and represent therefore a reliable value for the spin diffusion length of the H_2TPP-iron interface.

5 Summary and Outlook

It was demonstrated that the concept of multichannel spin- and angle-resolved photoemission spectroscopy with an imaging-type spin filter is a powerful emerging method. The versatility and flexibility of the employed spin filter lens in combination with the 15 mm iridium scattering crystal has been shown by the use of different imaging modes (Gaussian and reciprocal scattering) and spectrometer settings. To this date, this spin-resolving multichannel spectrometer based on a hemispherical analyzer is unique and increases the overall measuring efficiency for spin-resolved data by over 3 orders of magnitude compared to the conventional single channel measurement.

In the Gaussian scattering mode, the spin-resolving spectrometer has an energy resolution of 27 meV and an angular resolution of 0.23° for E_p = 30 eV and E_{kin} = 10 eV. In this case, the maximum energy and angular acceptance amounts to 1.5 eV and ±10°. At E_{kin} = 39 eV, a resolution of 134 meV and 0.44° is determined and the reciprocal scattering mode at E_{kin} = 10 eV shows a resolution of 67 meV and 0.33°. By investing more time in delicate lens voltage optimization, these values can be further optimized.

In the Gaussian imaging mode, the experimental setup allows for a microscopic crystallographic characterization of the spin filter crystal. The detected reflectivity differences originating from the mosaicity and defects can be exploited to assess the crystal preparation quality.

In the optimized 10 eV scattering condition, the iridium spin filter produces with spin-polarized secondary electrons asymmetry values of up to 15-20% for a freshly prepared Fe/W(110) sample and iridium crystal. This corresponds to a Sherman function of up to 0.37 ± 0.07. For the lifetime, i.e. the available time before the spin filter crystal has to be cleaned, values of up to 9.5 h have been observed at a pressure of $1 \cdot 10^{-10}$ mbar. Furthermore, a second high-temperature flash after several hours was able to partly recover the spin sensitivity.

A standard He-VUV lamp supplies sufficiently high intensity to measure multichannel spin- and angle-resolved spectra of iron within 1 minute per sample magnetization. This allows a fast momentum mapping in a small laboratory environment as shown for Fe/W(110).

A major advantage over conventional spin filter systems is the diversity of highly-efficient scattering conditions. They have been uncovered by a large-scale parameter mapping. Besides the standard conditions for the P_n polarization detection, additional conditions are detected at different azimuthal angles and scattering energies. Also for the previously unstudied P_e component, scattering conditions with comparable Sherman functions are measured. The azimuthal variation provides a new possibility for the polarization detection. With the P_e sensitivity, it is possible to tilt ferromagnetic samples for a k_x-k_y mapping without losing spin sensitivity due to changes in the polarization components. Until now, this possibility has not been considered for conventional SPLEED detector

systems. Finally, the results are confirmed by calculations.

An attached spin rotation lens allows to swap or intermix the P_n and P_e component arbitrarily. The spin rotator element also enables the three-dimensional vectorial spin polarization analysis as a special feature. For ferromagnetic samples, a combination of three scattering conditions leads to the determination of the full polarization vector (P_n, P_e, P_e). Even with non-magnetic samples, where the asymmetry cannot be produced by an initial beam polarization reversal, a full three-dimensional spin polarization analysis is possible. Here, 6 scattering conditions are needed to measure 3 asymmetries via the variation of scattering energies and azimuthal angles.

These findings are a considerable advantage since the three-dimensional spin polarization analysis was impossible without using several detectors or changing the experimental setup.

Finally, multichannel spin- and angle-resolving photoemission spectroscopy has been successfully used for the analysis of Fe/W(110) and H_2TPP on Fe/W(110) in different scattering conditions. Further experiments have been performed at the Hiroshima Synchrotron Radiation Center. The spin-resolved photoemission experiments of the metal-organic interface results in a spin diffusion length of 3.85-4.90 Å as an important input parameter for the design of metal-organic devices.

In summary, the experimental setup enables the fast and efficient spin-resolved photoemission spectroscopy. The spin filter characterization not only reveals new scattering conditions and analysis methods, but also the potential of a previously unexpected three-dimensional vectorial spin analysis. For the future, an extensive characterizations of the Au/Ir spin filter system [48] is envisioned. Adapting the spin filter method developed here to other techniques like the time-of-flight momentum microscopy can further enhance the efficiency of multichannel spin polarimetry. Ultimately, this paves the way for new developments and insights in solid state physics.

Bibliography

[1] R. Allenspach, M. Taborelli, M. Landolt, and H. C. Siegmann. Precursor to magnetic-domain nucleation observed by secondary-electron spin polarization. *Physical Review Letters*, 56(9), 1986.

[2] Nicolae Atodiresei, Jens Brede, Predrag Lazić, Vasile Caciuc, Germar Hoffmann, Roland Wiesendanger, and Stefan Blügel. Design of the local spin polarization at the organic-ferromagnetic interface. *Phys. Rev. Lett.*, 105:066601, Aug 2010.

[3] C. H. Back, C. Würsch, D. Kerkmann, and D. Pescia. Giant magnetic susceptibility in Fe and Co epitaxial films. *Zeitschrift für Physik B*, 96:1–3, 1994.

[4] Supriyo Bandyopadhyay. Dominant spin relaxation mechanism in compound organic semiconductors. *Phys. Rev. B*, 81:153202, Apr 2010.

[5] Supriyo Bandyopadhyay and Marc Cahay. *Introduction to Spintronics*. CRC Press, 2nd edition, 2016.

[6] P. Bauer, W. Eckstein, and N. Müller. Experimental study of longitudinal and transverse spin polarization in leed from platinum (111). *Zeitschrift für Physik B: Condensed Matter*, 52:185–192, 1983.

[7] P. Bauer, R. Feder, and N. Müller. Longitudinal spin polarization and symmetries in low-energy-electron diffraction: Experiment and theory for Pt(111). *Solid State Communications*, 36:249–251, 1980.

[8] P. Bauer, R. Feder, and N. Müller. Spin polarization in low-energy electron diffraction from Pt(111) experiment and theory. *Surface Science*, 99:395–401, 1980.

[9] G Bihlmayer, O Rader, and R Winkler. Focus on the rashba effect. *New Journal of Physics*, 17(5):050202, 2015.

[10] G. L. Bir, A. G. Aronov, and G. E. Pikus. Spin relaxation of electrons due to scattering by holes. *Sov. Phys.-JETP*, 42(4):705–712, 1975.

[11] Stephan Borek, Jürgen Braun, Ján Minár, and Hubert Ebert. *Ab initio* calculation of spin-polarized low-energy electron diffraction pattern for the systems Fe(001) and Fe(001)-$p(1 \times 1)$O. *Phys. Rev. B*, 92:075126, Aug 2015.

[12] J. Braun, C. Math, A. Postnikov, and M. Donath. Surface resonances versus surface states on Fe(110). *Phys. Rev. B*, 65:184412, Apr 2002.

[13] Jens Brede, Nicolae Atodiresei, Stefan Kuck, Predrag Lazić, Vasile Caciuc, Yoshitada Morikawa, Germar Hoffmann, Stefan Blügel, and Roland Wiesendanger. Spin-

and energy-dependent tunneling through a single molecule with intramolecular spatial resolution. *Phys. Rev. Lett.*, 105:047204, Jul 2010.

[14] Céphise M. Cacho, Sergio Vlaic, Marco Malvestuto, Barbara Ressel, Elaine A. Seddon, and Fulvio Parmigiani. Absolute spin calibration of an electron spin polarimeter by spin-resolved photoemission from the Au(111) surface states. *Review of Scientific Instruments*, 80:043904, 2009.

[15] Robert Celotta and Judah Levine, editors. *Methods of Experiment Physics*, volume 22. Academic Press, Inc., 1985.

[16] Tomasz Dietl, David D. Awschalom, Maria Kaminska, and Hideo Ohno, editors. *Spintronics*. Academic Press, 2008.

[17] Fatima Djeghloul, Manuel Gruber, Etienne Urbain, Dimitra Xenioti, Loic Joly, Samy Boukari, Jacek Arabski, Hervé Bulou, Fabrice Scheurer, François Bertran, Patrick Le Fèvre, Amina Taleb-Ibrahimi, Wulf Wulfhekel, Guillaume Garreau, Samar Hajjar-Garreau, Patrick Wetzel, Mebarek Alouani, Eric Beaurepaire, Martin Bowen, and Wolfgang Weber. High spin polarization at ferromagnetic metal-organic interfaces: A generic property. *The Journal of Physical Chemistry Letters*, 7(13):2310–2315, 2016.

[18] T. Duden and E. Bauer. A compact electron-spin-polarization manipulator. *Review of Scientific Instruments*, 66, 1995.

[19] M. I. D'yakonov and V. I. Perel'. Spin relaxation of conduction electrons in noncentrosymmetric semiconductors. *Soviet Physics - Solid State*, 13(12):3023–3026, 1972.

[20] R. F. Egerton. *Physical Principles of Electron Microscopy - An Introduction to TEM, SEM and AEM*. Springer-Verlag, 2005.

[21] Albert Einstein. Über einen die Erzeugung und Verwandlung des Lichtes betreffenden heuristischen Gesichtspunkt. *Annalen der Physik*, 322:132–148, 1905.

[22] R. J. Elliott. Theory of the effect of spin-orbit coupling on magnetic resonance in some semiconductors. *Physical Review*, 96(2):266–279, 1954.

[23] H. J. Elmers, J. Hauschild, and U. Gradmann. Onset of perpendicular magnetization in nanostripe arrays of Fe on stepped W(110) surfaces. *Physical Review B*, 59(5):3688–3695, 1999.

[24] H. J. Elmers, J. Hauschild, H. Hoche, U. Gradmann, H. Bethge, D. Heuer, and U. Kohler. Submonolayer magnetism of Fe(110)on W(110): Finite width scaling of stripes and percolation between islands. *Physical Review Letters*, 73(6):898–901, 1994.

[25] Hans-Joachim Elmers. *Handbook of Magnetism and Advanced Magnetic Materials - Novel Techniques for Characterizing and Preparing Samples*, volume 3. John Wiley & Sons, Inc., 2007.

[26] W. Erley and H. Ibach. Vibrations excitations and structure of oxygen on Fe(110). *Solid State Communications*, 37:937–942, 1981.

[27] Claudia Felser, Lukas Wollmann, Stanislav Chadov, Gerhard H. Fecher, and Stuart S. P. Parkin. Basics and prospective of magnetic Heusler compounds. *APL Mater.*, 3(4), 2015.

[28] O Fruchart, P O Jubert, M Eleoui, F Cheynis, B Borca, P David, V Santonacci, A Liénard, M Hasegawa, and C Meyer. Growth modes of fe(110) revisited: a contribution of self-assembly to magnetic materials. *Journal of Physics: Condensed Matter*, 19(5):053001, 2007.

[29] Brent Fultz and James Howe. *Transmission Electron Microscopy and Diffractometry of Materials*. Springer-Verlag, 4th edition, 2013.

[30] U. Gradmann and G. Waller. Periodic lattice distortions in epitaxial films of Fe(110) on W(110). *Surface Science*, 116:539–548, 1982.

[31] L. G. Gray, M. W. Hart, F. B. Dunning, , and G. K. Walters. Simple, compact, medium-energy Mott polarization analyzer. *Review of Scientific Instruments*, 55:88–91, 1984.

[32] M. Z. Hasan and C. L. Kane. *Colloquium* : Topological insulators. *Rev. Mod. Phys.*, 82:3045–3067, Nov 2010.

[33] U. Heinzmann. New vacuum-ultraviolet absorption data for lead vapour obtained by spin-polarisation measurements. *J. Phys. B: Atom. Phys.*, 11:399–412, 1978.

[34] Heinrich Rudolf Hertz. Ueber den Einfluss des ultravioletten Lichtes auf die electrische Entladung. *Annalen der Physik*, 267:983–1000, 1887.

[35] F. U. Hillebrecht, R. M. Jungblut, L. Wiebusch, Ch. Roth, H. B. Rose, D. Knabben, C. Bethke, N. B. Weber, St. Manderla, U. Rosowski, and E. Kisker. High-efficiency spin polarimetry by very-low-energy electron scattering from Fe(100) for spin-resolved photoemission. *Review of Scientific Instruments*, 73:1229–1234, 2002.

[36] P. Hohenberg and W. Kohn. Inhomogeneous electron gas. *Physical Review*, 136(3B):864–871, 1964.

[37] Stefan Hüfner. *Photoelectron Spectroscopy*. Springer-Verlag, third edition, 2003.

[38] Harald Ibach. *Physics of Surfaces and Interfaces*. Springer-Verlag, 6th edition, 2006.

[39] Fuhao Ji, Tan Shi, Mao Ye, Weishi Wan, Zhen Liu, Jiajia Wang, Tao Xu, and Shan Qiao. Multichannel exchange-scattering spin polarimetry. *Phys. Rev. Lett.*, 116:177601, Apr 2016.

[40] M. Jourdan, J. Minár, J. Braun, A. Kronenberg, S. Chadov, B. Balke, A. Gloskovskii, M. Kolbe, H.J. Elmers, G. Schönhense, H. Ebert, C. Felser, and M. Kläui. Direct observation of half-metallicity in the Heusler compound Co 2 MnSi. *nature communications*, 5(3974), 2014.

[41] C. Jozwiak, J. Graf, G. Lebedev, N. Andresen, A. K. Schmid, A. V. Fedorov, F. El Gabaly, W. Wan, A. Lanzara, and Z. Hussain. A high-efficiency spin-resolved photoemission spectrometer combining time-of-flight spectroscopy with exchange-scattering polarimetry. *Review of Scientific Instruments*, 81:053904, 2010.

[42] Antoine Kahn, Norbert Koch, and Weiying Gao. Electronic structure and electrical properties of interfaces between metals and π-conjugated molecular films. *Journal of Polymer Science Part B: Polymer Physics*, 41(21):2529–2548, 2003.

[43] Joachim Kessler. *Polarized Electrons*. Springer-Verlag, second edition, 1976.

[44] H.-J. Kim and E. Vescovo. Spin-resolved photoemission investigation of the $c(2\times2)$ and $c(3\times1)$ oxygen overlayers on the Fe(110) surface. *Phys. Rev. B*, 58:14047–14050, Nov 1998.

[45] J. Kirschner. *Polarized Electrons at Surfaces*. Springer-Verlag, 1985.

[46] J. Kirschner and R. Feder. Spin polarization in double diffraction of low-energy electrons from W(001): Experiment and theory. *Physical Review Letters*, 42(15):1008–1011, 1979.

[47] J. Kirschner, R. Feder, and J. F. Wendelken. Electron spin polarization in energy- and angle-resolved photoemission from W(001): Experiment and theory. *Physical Review Letters*, 47(8):614–617, 1981.

[48] J. Kirschner, F. Giebels, H. Gollisch, and R. Feder. Spin-polarized electron scattering from pseudomorphic Au on Ir(001). *Physical Review B*, 88:125419, 2013.

[49] J. Kirschner and K. Koike. Spin polarization of secondary electrons from Fe(110) excited by unpolarized primary electrons. *Surface Science*, 273:147–159, 1992.

[50] E. Kisker, R. Clauberg, and W. Gudat. Electron spectrometer for spin-polarized angle- and energy-resolved photoemission from ferromagnets. *Review of Scientific Instruments*, 53:1137–1144, 1982.

[51] M. Kolbe, P. Lushchyk, B. Petereit, H. J. Elmers, G. Schönhense, A. Oelsner, C. Tusche, and J. Kirschner. Highly efficient multichannel spin-polarization detection. *Physical Review Letters*, 107(207601):1–5, 2011.

[52] Markus König, Steffen Wiedmann, Christoph Brüne, Andreas Roth, Hartmut Buhmann, Laurens W. Molenkamp, Xiao-Liang Qi, and Shou-Cheng Zhang. Quantum spin hall insulator state in HgTe quantum wells. *Science*, 318(5851):766–770, 2007.

[53] R. Kurzawa, K.-P. Kämper, W. Schmitt, and G. G̈untherodt. Spin-resolved photoemission study of in situ grown epitaxial fe layers on W(110). *Solid State Communications*, 60(10):777–780, 1986.

[54] D. Kutnyakhov, S. Chernov, K. Medjanik, R. Wallauer, C. Tusche, M. Ellguth, S. A. Nepijko, M. Krivenkov, J. Braun, S. Borek, J. Minár, H. Ebert, H. J. Elmers, and G. Schönhense. Spin texture of time-reversal symmetry invariant surface states on W(110). *Scientific Reports*, 6(29394), 2016.

[55] D. Kutnyakhov, H. J. Elmers, G. Schönhense, C. Tusche, S. Borek, J. Braun, J. Minár, and H. Ebert. Specular reflection of spin-polarized electrons from the W(001) spin-filter crystal in a large range of scattering energies and angles. *Physical Review B*, 91:014416, 2015.

[56] D. Kutnyakhov, P. Lushchyk, A. Fognini, D. Perriard, M. Kolbe, K. Medjanik, E. Fedchenko, S. A. Nepijko, H. J. Elmers, G. Salvatella, C. Stieger, R. Gort, T. Bähler, T. Michlmayer, Y. Acremann, A. Vaterlaus, F. Giebels, H. Gollisch, and J.Kirschner d G.Schönhense a n R. Feder C. Tusche d, A.Krasyuk d. Imaging spin filter for electrons based on specular reflection from iridium(001). *Ultramicroscopy*, 130:63–69, 2013.

[57] Dmytro Kutnyakhov. *Imaging Spin-Filter Efficiency of W(001) and Ir(001) Single Crystals*. PhD thesis, Institut f̈ur Physik, 2014.

[58] Mohamed Aymen Mahjoub, Guillaume Monier, Christine Robert-Goumet, Luc Bideux, and Bernard Gruzza. New method for the determination of the correction function of a hemisphericalerical electron analyzer based on elastic electron images. *Journal of Electron Spectroscopy and Related Phenomena*, 197:80–87, 2014.

[59] Allan J. Melmed. Epitaxial growth of iron on tungsten field emission points. *Surface Science*, 7:478–481, 1967.

[60] T. Methfessel, S. Steil, N. Baadji, N. Großmann, K. Koffler, S. Sanvito, M. Aeschlimann, M. Cinchetti, and H. J. Elmers. Spin scattering and spin-polarized hybrid interface states at a metal-organic interface. *Phys. Rev. B*, 84:224403, Dec 2011.

[61] S. Miesch, A. Fognini, Y. Acremann, A. Vaterlaus, and T. U. Michlmayr. Fe on W(110), a stable magnetic reference system. *Journal of Applied Physics*, 109:013905, 2011.

[62] K. Miyamoto, A. Kimura, T. Okuda, K. Shimada, H. Iwasawa, H. Hayashi, H. Namatame, M. Taniguchi, and M. Donath. Massless or heavy due to two-fold symmetry: Surface-state electrons at w(110). *Phys. Rev. B*, 86:161411, Oct 2012.

[63] Marco Nardi, Roberto Verucchi, Riccardo Tubino, and Salvatore Iannotta. Activation and control of organolanthanide synthesis by supersonic molecular beams: Erbium-porphyrin test case. *Phys. Rev. B*, 79:125404, Mar 2009.

[64] Akinori Nishide, Yasuo Takeichi, Taichi Okuda, Alexey A Taskin, Toru Hirahara, Kan Nakatsuji, Fumio Komori, Akito Kakizaki, Yoichi Ando, and Iwao Matsuda. Spin-polarized surface bands of a three-dimensional topological insulator studied by high-resolution spin- and angle-resolved photoemission spectroscopy. *New Journal of Physics*, 12(6):065011, 2010.

[65] Taichi Okuda, Koji Miyamaoto, Hirokazu Miyahara, Kenta Kuroda, Akio Kimura, Hirofumi Namatame, and Masaki Taniguchi. Efficient spin resolved spectroscopy observation machine at Hiroshima Synchrotron Radiation Center. *Review of Scientific Instruments*, 82(10), 2011.

[66] Taichi Okuda, Koji Miyamoto, Akio Kimura, Hirofumi Namatame, and Masaki Taniguchi. A double {VLEED} spin detector for high-resolution three dimensional spin vectorial analysis of anisotropic rashba spin splitting. *Journal of Electron Spectroscopy and Related Phenomena*, 201:23 – 29, 2015. Special issue on electron spectroscopy for Rashba spin-orbit interaction.

[67] Taichi Okuda, Yasuo Takeichi, Yuuki Maeda, Ayumi Harasawa, Iwao Matsuda, Toyohiko Kinoshita, and Akito Kakizaki. A new spin-polarized photoemission spectrometer with very high efficiency and energy resolution. *Review of Scientific Instruments*, 79:123117, 2008.

[68] J. B. Pendry. *Low-Energy Electron Diffraction*, pages 201–211. Springer US, Boston, MA, 1990.

[69] N. L. Peterson. Diffusion in refractory metals. Technical report, Advanced Metals Research Corporation, 1960.

[70] V. N. Petrov, V. V. Grebenshikov, A. N. Andronov, P. G. Gabdullin, and A. V. Maslevtcov. Ultrafast compact classical Mott polarimeter. *Review of Scientific Instruments*, 78:025102, 2007.

[71] S. Qiao, A. Kimura, A. Harasawa, M. Sawada, J.-G. Chung, and A. Kakizaki. A new compact electron spin polarimeter with a high efficiency. *Review of Scientific Instruments*, 68:4390–4395, 1997.

[72] Karthik V. Raman. Interface-assisted molecular spintronics. *Applied Physics Reviews*, 1:031101, 2014.

[73] Eli Rotenberg and S. D. Kevan. Evolution of fermi level crossings versus h coverage on $w(110)$. *Phys. Rev. Lett.*, 80:2905–2908, Mar 1998.

[74] Y. Sakisaka, Thor Rhodin, and D. Mueller. Angle-resolved photoemission from Fe(110): Determination of e(k). *Solid State Communications*, 53(9):793 – 799, 1985.

[75] J. Sawler and D. Venus. Electron polarimeter based on spin-polarized low-energy electron diffraction. *Review of Scientific Instruments*, 62(10):2409–2418, 1991.

[76] Erik D. Schaefer, Stephan Borek, Jűrgen Braun, Ján Minár, H. Ebert, Gerd Schönhense, and Hans-Joachim Elmers. Vectorial spin-polarization detection in multichannel spin-resolved photoemission spectroscopy using an Ir(100) imaging spin filter. *to be published*, 2017.

[77] J. Schäfer, M. Hoinkis, Eli Rotenberg, P. Blaha, and R. Claessen. Fermi surface and electron correlation effects of ferromagnetic iron. *Physical Review B*, 72, 2005.

[78] G. Schmidt, D. Ferrand, L. W. Molenkamp, A. T. Filip, and B. J. van Wees. Fundamental obstacle for electrical spin injection from a ferromagnetic metal into a diffusive semiconductor. *Phys. Rev. B*, 62:R4790–R4793, Aug 2000.

[79] G. Schönhense and H. C. Siegmann. Transmission of electrons through ferromagnetic material and applications to detection of electron spin polarization. *Annalen der Physik*, 505(5):465–474, 1993.

[80] Gerd Schönhense, Katerina Medjanik, and Hans-Joachim Elmers. Space-, time- and spin-resolved photoemission. *Journal of Electron Spectroscopy and Related Phenomena*, 200:94–118, 2015.

[81] A Schulz, R Courths, H Schulz, and S Hufner. UPS investigation of Fe single crystals. *Journal of Physics F: Metal Physics*, 9(2):L41, 1979.

[82] M. P. Seah and W. A. Dench. Quantitative electron spectroscopy of surfaces: A standard data base for electron inelastic mean free path in solids. *Surface and Interference Analysis*, 1(1):2–11, 1979.

[83] Helmut Sitter, Claudia Draxl, and Michael Ramsey, editors. *Small Organic Molecules on Surfaces*, volume 173. Springer Berlin Heidelberg, 2013.

[84] SPECS Surface Nano Analysis GmbH. *PHOIBOS 100/150 Hemispherical Energy Analyzer*, 2012.

[85] Sabine Steil, Nicolas Groszmann, Martin Laux, Andreas Ruffing, Daniel Steil, Martin Wiesenmayer, Stefan Mathias, Oliver L. A. Monti, Mirko Cinchetti, and Martin Aeschlimann. Spin-dependent trapping of electrons at spinterfaces. *Nat Phys*, 9(4):242–247, April 2013.

[86] V. N. Strocov, X. Wang, M. Shi, M. Kobayashi, J. Krempasky, C. Hess, T. Schmitt, and L. Patthey. Soft-X-ray ARPES facility at the ADRESS beamline of the SLS: concepts, technical realisation and scientific applications. *Journal of Synchrotron Radiation*, 21:32–44, 2014.

[87] Vladimir N. Strocov, Vladimir N. Petrov, and J. Hugo Dil. Concept of a multichannel spin-resolving electron analyzer based on Mott scattering. *Journal of Synchrotron Radiation*, 22(3):708–716, May 2015.

[88] S. Suga, A. Sekiyama, G. Funabashi, J. Yamaguchi, M. Kimura, M. Tsujibayashi, T. Uyama, H. Sugiyama, Y. Tomida, G. Kuwahara, S. Kitayama, K. Fukushima, K. Kimura, T. Yokoi, K. Murakami, H. Fujiwara, Y. Saitoh, L. Plucinski, and C. M. Schneider. High resolution, low hν photoelectron spectroscopy with the use of a microwave excited rare gas lamp and ionic crystal filters. *Review of Scientific Instruments*, 81:105111, 2010.

[89] Shigemasa Suga and Christian Tusche. Photoelectron spectroscopy in a wide hν region from 6 eV to 8 keV with full momentum and spin resolution. *Journal of Electron Spectroscopy and Related Phenomena*, 200:119–142, 2015.

[90] H. Tang, M. Plihal, and D. L. Mills. Theoretical studies of spin-polarized LEED rotation curves: Clean W(100) and Fe overlayers on W(100). *Phys. Rev. B*, 54:14172–14184, Nov 1996.

[91] Christian Thiede, Christian Langenkämper, Kaito Shirai, Anke B. Schmidt, Taichi Okuda, and Markus Donath. Reflectivity and sherman maps of passivated Fe(001): Working points for a display-type spin-polarization analyzer. *Physical Review Applied*, 1:054003, 2014.

[92] D. Tillmann, R. Thiel, and E. Kisker. Very-low-energy spin-polarized electron diffraction from Fe(001). *Z. Phys. B - Condensed Matter*, 77:1–2, 1989.

[93] A. M. Turner and J. L. Erskine. Exchange splitting and critical-point binding energies for iron (110). *Physical Review B*, 25(3), 1982.

[94] C. Tusche, M. Ellguth, A. A. Ünal, C.-T. Chiang, A. Winkelmann, A. Krasyuk, M. Hahn, G. Schönhense, and J. Kirschner. Spin resolved photoelectron microscopy using a two-dimensional spin-polarizing electron mirror. *Applied Physics Letters*, 99:032505, 2011.

[95] Christian Tusche, Alexander Krasyuk, and Jürgen Kirschner. Spin resolved bandstructure imaging with a high resolution momentum microscope. *Ultramicroscopy*, 159:520–529, 2015.

[96] G. E. Uhlenbeck and S. Goudsmit. Spinning electrons and the structure of spectra. *Nature*, 117:264–265, February 1926.

[97] J. van Klinken. Double scattering of electrons. *Nuclear Physics*, 75:161–188, 1966.

[98] D. Vasilyev, C. Tusche, F. Giebels, H. Gollisch, R. Feder, and J. Kirschner. Low-energy electron reflection from Au-passivated Ir(001) for application in imaging spin-filters. *Journal of Electron Spectroscopy and Related Phenomena*, 199:10–18, 2015.

[99] D. Venus. Use of spin-polarized LEED rotation curves to study disordered surfaces W(001)-(1x1) and W(001)-2H(1x1). *Surface Science*, 291:418–428, 1993.

[100] D. Venus, S. Cool, and M. Plihal. Quantitative structural determination using spin-polarized low-energy electron diffraction rotation curves W(110). *Surface Science*, 446:199–210, 2000.

[101] E. Vescovo, C. Carbone, W. Eberhardt, O. Rader, T. Kachel, and W. Gudat. Spin-resolved photoemission study of the clean and oxygen-covered Fe(110) surface. *Phys. Rev. B*, 48:285–288, Jul 1993.

[102] R. Vollmer, M. Etzkorn, P.S. Anil Kumar, H. Ibach, and J. Kirschner. Spin-polarized electron energy loss spectroscopy of high energy, large wave vector spin waves in ultrathin fcc Co films on Cu(001). *Physical Review Letters*, 91(14):147201, 2003.

[103] J. Weissenrieder, M. Göthelid, M. Mansson, H. von Schenck, O. Tjernberg, and U.O. Karlsson. Oxygen structures on Fe(110). *Surface Science*, 527:163–172, 2003.

[104] A. Winkelmann, D. Hartung, H. Engelhard, C.-T. Chiang, and J. Kirschner. High efficiency electron spin polarization analyzer based on exchange scattering at Fe/W(001). *Review of Scientific Instruments*, 79:083303, 2008.

[105] Su-Yang Xu, Ilya Belopolski, Nasser Alidoust, Madhab Neupane, Guang Bian, Chenglong Zhang, Raman Sankar, Guoqing Chang, Zhujun Yuan, Chi-Cheng Lee, Shin-Ming Huang, Hao Zheng, Jie Ma, Daniel S. Sanchez, BaoKai Wang, Arun Bansil, Fangcheng Chou, Pavel P. Shibayev, Hsin Lin, Shuang Jia, and M. Zahid Hasan. Discovery of a Weyl fermion semimetal and topological Fermi arcs. *Science*, 349(6248):613–617, 2015.

[106] Y. Yafet. g factors and spin-lattice relaxation of conduction electrons. *Solid State Physics*, 14:1–98, 1963.

[107] Kh. Zakeri, T. R. F. Peixoto, Y. Zhang, J. Prokop, and J. Kirschner. On the preparation of clean tungsten single crystal. *Surface Science*, 604:L1–L3, 2010.

[108] Yimei Zhu, editor. *Modern Techniques for Characterizing Magnetic Materials*. Springer, 2005.

List of Publications

[1] Erik D. Schaefer, Sergey V. Chernov, Alexey A. Sapozhnik, Dmytro M. Kostyuk, Anna V. Zaporozhchenko, Serhiy I. Protsenko, Matthias Bode, Sergej A. Nepijko, Hans-Joachim Elmers and Gerd Schönhense, *Vectorial spin-polarization detection in multichannel spin-resolved photoemission spectroscopy using an Ir(001) imaging spin filter*, to be published (2017).

[2] Erik D. Schaefer, Stephan Borek, Jürgen Braun, Ján Minár, Hubert Ebert, Gerd Schönhense and Hans-Joachim Elmers, *Morphological and magnetic analysis of Fe nanostructures on W(110) by using scanning tunneling microscopy and Lorentz microscopy*, Japanese Journal of Applied Physics **55** (2016), no. 2S, 02BC11.